MAX-PLANCK-INSTITUT
FÜR CHEMISCHE PHYSIK FESTER STOFFE

TECHNISCHE UNIVERSITÄT DRESDEN

Investigation of Structural Properties and their Relation to the Phase Transitions in Shape Memory Heusler Compounds

Dissertation
zur Erlangung des akademischen Grades
Doctor of Philosophy
(Ph. D.)

vorgelegt von

Parul Devi
geboren in Meerut, India

Max Planck Institute for Chemical Physics of Solids Dresden

Fakultät Physik
Fakultät Mathematik und Naturwissenschaften
der Technischen Universität Dresden
2019

Tag der Einreichung: _._.2019

1.Gutachter: **Prof. Dr. Claudia Felser**
Festkörperchemie
Max-Planck-Institut für Chemische Physik fester Stoffe
Nöthnitzer Str. 40, 01187 Dresden

2.Gutachter: **Prof. Dr. Sebastian T. B. Goennenwein**
Institut für Festkörper
Technische Universität Dresden
D-01062 Dresden

3.Reader: **Jun.-Prof. Dr. rer. nat. Dmytro S. Inosov**
Institut für Festkörper
Technische Universität Dresden
D-01062 Dresden

Tag der Einreichung: _._2019

Dedicated to my mother

Versicherung

Hiermit versichere ich, dass ich die vorliegende Arbeit mit dem Titel "Investigation of Structural Properties and their Relation to the Phase Transitions in Shape Memory Heusler Compounds" ohne unzulässige Hilfe Dritter und ohne Benutzung anderer als der angegebenen Hilfsmittel angefertigt habe. Die aus fremden Quellen direkt oder indirekt übernommenen Gedanken sind als solche kenntlich gemacht. Die Arbeit wurde bisher weder im Inland noch im Ausland in gleicher oder ähnlicher Form einer anderen Prüfungsbehörde vorgelegt.

Die vorliegende Dissertation wurde am Max-Planck-Institut für chemische Physik fester Stoffe unter der wissenschaftlichen Betreuung von Frau Prof. Dr. Claudia Felser.

Ich erkenne die Promotionsordnung der Fakultät Mathematik und Naturwissenschaften der Technischen Universität Dresden an.

Parul Devi
Dresden, January 2019

Abstract

The present thesis is devoted to the investigation of modulated structures as well as the direct measurement of magnetocaloric effect (MCE) in Ni-Mn based magnetic shape memory (MSM) Heusler compounds in pulsed magnetic fields after analyzing isothermal entropy data taken in static magnetic fields. The emphasis is on the modulated structure of MSM Heusler compounds because of lower twinning stress which facilitates the easy transformation from austenite to martensite structure. Synchrotron x-ray powder diffraction (SXRPD) was carried out to study the modulated structure and NPD for antisite disorder as Ni and Mn have easily the same atomic scattering factor. Direct measurement of the adiabatic temperature change ΔT_{ad} was done in pulsed magnetic fields, because of fast response of $\sim$10 to 100 ms to the sample temperature on magnetic field, providing adiabatic conditions. It also gives an opportunity of very high magnetic fields up to 70 T because of short pulse duration during the measurement.

The modulated structure has been studied for the off-stoichiometric $Ni_2Mn_{1.4}In_{0.6}$ and $Ni_{1.9}Pt_{0.1}MnGa$ MSM Heusler compounds from SXRPD and NPD. $Ni_2Mn_{1.4}In_{0.6}$ exhibits martensitic transition at $T_{\mathrm{M}} \approx 295$ K and Curie temperature $T_{\mathrm{C}} \approx 315$ K. Rietveld refinement reveals uniform atomic displacement in the modulated structure of martensite phase and the absence of premartensite phase and phason broadening of the satellite peaks which was further confirmed by HRTEM study. Therefore, the structural modulation in $Ni_2Mn_{1.4}In_{0.6}$ can be successfully explained in term of the adaptive phase model. Whereas, $Ni_{1.9}Pt_{0.1}MnGa$ shows the premartensite phase in addition to the martensite and austenite phases and follows the soft phonon model. The temperature dependent ac-susceptibility shows the change in slope at different temperatures 365, 265, 230 and 220 K corresponding to the Curie temperature T_{C}, first premartensite T_1, second premartensite T_2 and martensite temperature T_{M}, respectively. Temperature-dependent high resolution SXRPD data analysis shows first, a nearly $3M$ modulated premartensite phase with an average cubic-like feature i.e. negligible Bain distortion of the elementary $L2_1$ unit cell results from the austenite phase. This phase then undergoes an isostructural phase transition $3M$ like premartensite phase with robust Bain distortion in

the temperature range from 220 to 195 K. Below 195 K, the martensite phase appears which results from the larger Bain-distorted premartensite phase.

In this work, the magnetocaloric properties of $Ni_{2.2}Mn_{0.8}Ga$ and $Ni_{1.8}Mn_{1.8}In_{0.4}$ magnetic shape memory (MSM) Heusler compounds were studied. $Ni_{2.2}Mn_{0.8}Ga$ exhibits the reversible conventional MCE, measured from isothermal entropy change ΔS_M and adiabatic temperature change ΔT_{ad} because of the geometric compatibility condition (GCC) for cubic austenite phase to tetragonal martensite phase as a consequence of low thermal hysteresis of the martensite phase transition. The reversible MCE has been confirmed by applying more than one pulse in the hysteresis region at 317 K. $Ni_{1.8}Mn_{1.8}In_{0.4}$ possess improved reversible behavior of inverse MCE due to the closely satisfying of GCC from cubic austenite to modulated monclinic martensite structure. The maximum value of ΔS_M has been found to the same for both heating and cooling curves measured from isothermal magnetization $M(T)$ curves until a magnetic field of 5 T. The adiabatic temperature change ΔT_{ad} results in a value of $\approx$ 10 K by applying a magnetic field of 20 T in a pulsed magnetic field. Furthermore reversible magnetostriction of 0.3% was observed near the first-order martensite phase transition temperatures 265, 270 and 280 K.

A reduction of thermal hysteresis has been found in MSM Heusler compounds $Ni_2Mn_{1.4}In_{0.6}$ and $Ni_{1.8}Co_{0.2}Mn_{1.4}In_{0.6}$ with the application of hydrostatic pressure followed by GCC from pressure dependent x-ray diffraction in both austenite and martensite phase. By increasing pressure, the lattice parameters of both phases change in such a way that they increasingly satisfy the GCC. The approach of GCC for different kind of martensite structures (tetragonal, orthorhombic and monoclinic) will help to design new MSM Heusler compounds taking advantage of first-order martensite phase transition.

Contents

Nomenclature

$\Delta T_{\mathrm{ad}}^{\mathrm{str}}$	Structural contribution to the adiabatic temperature change
$\Delta T_{\mathrm{ad}}^{\mathrm{mag}}$	Magnetic contribution to the adiabatic temperature change
β_{mar}	Isothermal compressibility of martensite phase
β_{aus}	Isothermal compressibility of austenite phase
ΔS_{iso}	Isothermal entropy change
$\Delta T_{\mathrm{ad}}^{\mathrm{max}}$	Maximum adiabatic temperature change
ΔT_{t}	Shift of the transition temperature
ΔV	Volume change during the transition
C_{P}	Heat capacity at constant pressure
ΔT_{hys}	Width of the thermal hysteresis
ΔS_{el}	Electronic entropy change
ΔT_{ad}	Adiabatic temperature change
ΔS_{mag}	Magnetic entropy change
ΔM	Magnetization change
$\mathbf{q}$	Modulation vector
M	Magnetization
m	magnetic moment
M_{f}	Martensite finish
M_{s}	Martensite start
A_{s}	Austenite start
A_{f}	Austenite finish
ΔS_{lat}	Lattice entropy change
Δl	Relative length change
ΔS_{T}	Total entropy change
$\mathbf{U}$	Transformation matrix
t	Time
U_{iso}	Atomic displacement
T_{C}	Curie temperature
RT	Room temperature
μ_{B}	Bohr magneton
P	Pressure

Nomenclature

λ_2	Middle eigenvalue of the transformation matrix
a_{pm}, b_{pm}, c_{pm}	Lattice parameters of premartensite phase
a_m, b_m, c_m	Lattice parameters of martensite phase
T_{PM}	Premartensite transition temperature
T_{M}	Martensite transition temperature
T_{A}	Austenite transition temperature
GCC	Geometric compatibility condition
a_c	Lattice parameter of cubic phase
FWHM	Full width at half maximum
FCC	Field cooled cooling
FCW	Field cooled warming
ZFC	Zero field cooling
MSM	Magnetic shape memory
MCE	Magnetocaloric effect
TA	Transverse acoustic
K	Boltzmann constant
h	Planck constant

1 Introduction

The present thesis aims to provide a comprehensive study on the optimization of the MCE in MSM Heusler compounds for application in magnetic refrigeration. This thesis is organized as follows:

1.1 Motivation of Work

Conventional gas compression refrigeration technology uses chlorofluorocarbons (CFCs) and hydrochlorofluorocarbons (HCFCs) as working fluids, has raised serious environmental concerns because of global warming [1]. Therefore, scientist and engineers have expended a lot of research effort to replace this technology from the other cooling technology, named as magnetic refrigeration (MR). MR near room temperature (RT) is a relatively novel technique, which is based on the MCE [2, 3]. The MCE results from the coupling of a system of magnetic moments, which creates cooling or heating of a system with an external magnetic field [4, 5]. This magnetocaloric phenomenon was first discovered by Emil Warburg in pure iron in 1881 [6]. The MCE is characterized by two parameters: (a) Isothermal entropy change ΔS_{M} and adiabatic temperature change ΔT_{ad}. The Isothermal entropy change ΔS_{M} defines the amount of heat that can be transferred in one cooling cycle and adiabatic temperature change ΔT_{ad} is related to the temperature span of the working device. These two quantities should be as large as possible in small magnetic field changes [7, 8].

Since, the most expensive part of a magnetocaloric cooling device is the magnetic field source. So, the maximum volume should be utilized as efficiently as possible for applying the magnetic field [4, 9]. Also, thermal conductivity of the material should be maximized. The prerequisite for that is a good thermal contact between the magnetocaloric material and heat exchange fluid [7]. To

enhance the heat exchange, it is important to use of fine structures of magnetocaloric material for obtaining a large surface area [8]. The magnetocaloric material should contain no harmful element in order to keep low environment impact. Thus for practical magnetic cooling applications, research is focused on the development of new materials with appropriate properties [2]. The material must also be capable to operate for millions of cycles without any fatigue and the long-term corrosion resistance must be guaranteed too [10, 11].

Nowadays, there are several material families which belongs to the great potential for applications in magnetic refrigeration [11, 12]. Gd is the benchmark material with outstanding properties and used in most magnetocaloric demonstrators [13, 14]. In 1997, Pecharsky and Gschneidner discovered another material $Gd_5(Ge, Si)_4$, which has several times larger isothermal entropy change ΔS_M and comparable adiabatic temperature change ΔT_{ad} to Gd [15, 16, 17]. Both Gd and $Gd_5(Ge, Si)_4$ has the drawback that they contain heavy rare-earth element Gd, which is very expensive. As an alternative, $La(Fe, Si)_{13}$ material class was developed [18, 19]. It also contains rare-earth element La, but it is much more abundant than Gd. In La-based material family, the transition temperature and the magnetocaloric properties can be precisely tuned to the desired temperature range by compositional variation or the addition of Co, Mn and interstitial H [20, 21]. After that, Fe_2P-type compounds were discovered which contain no rare-earth element. The first intensively studied system in this material family was Mn-Fe-P-As. It involves toxic As. Later, the toxic As element was replaced by Si and Ge [22, 23, 24, 25].

Another rare-earth free material class are Ni-Mn based Heusler compounds, which undergo a martensitic phase transformation [12, 26, 27, 28]. The martensitic transition temperature can be easily tuned in a broad temperature window by changing stoichiometry, substitution of an interstitial element and annealing conditions [28]. In addition to that, these materials show large MCE near RT, which make them outstanding and very promising for magnetic refrigeration [28, 29]. However, the large thermal hysteresis around the martensitic transition creates irreversible MCE in cyclic operation, which made them less feasible [26]. Recently, it has been shown that Ni-Mn based Heusler compounds show modulated structure in martensite phase [27, 30]. The modulated structure has lower twinning stress which can make an easy movement of material from

martensite to austenite and so that it can facilitate the reversible MCE in cyclic operations. Therefore, it is necessary to understand the origin of modulation in these compounds for improving the reversibility of MR [27, 29]. The aim of this thesis is devoted to study the origin of modulated structure in Ni-Mn based MSM Heusler compounds. It also focus on the reduction of hysteresis by chemical and physical pressure with the measurement of MCE in pulsed magnetic field.

1.2 Organization of Thesis

The organization and motivation behind the PhD research work are outlined in Chapter 1. In Chapter 2, an initial introduction of HeusIer compounds promising for MCE has been given. MSM HeusIer compounds show the modulated structure in martensite phase which is studied from SXRPD and can be analysed by Le Bail refinement initially and then Rietveld refinement using FullProf software. The analysis steps for Le Bail and Rietveld refinement has been shown in flowchart. This is followed by sample preparation and detailed experimental descriptions of the modulated structure from XRD and magnetocaloric measurements in pulsed magnetic fields. A short overview of other experimental techniques used in this thesis, including NPD, SEM, magnetization, magnetostriction and magnetocaloric measurements in Chapter 3 has been given.

Chapter 4 explains the modulated structure by using both models: adaptive phase model and soft phonon model in two different $Ni_2Mn_{1.4}In_{0.6}$ and $Ni_{1.9}Pt_{0.1}MnGa$ MSM Heusler compounds. $Ni_2Mn_{1.4}In_{0.6}$ shows $3M$ modulated martensite structure only whereas, $Ni_{1.9}Pt_{0.1}MnGa$ shows both premartensite and martensite structure. The nature of modulated structure was studied using high resolution SXRPD and NPD as a function of temperature and analysed on the basis of $(3+1)-D$ crystallography. Chapter 5 presents the structure, magnetic and MCE analysis in pulsed magnetic field inspired by a recent theoretical study of GCC. Chapter 6 focuses on the hydrostatic pressure study for reducing the hysteresis in two different $Ni_2Mn_{1.4}In_{0.6}$ and $Ni_{1.8}Co_{0.2}Mn_{1.4}In_{0.6}$ MSM Heusler compounds. It deals with the pressure dependent XRD and magnetization. Last chapter 7 describes the conclusion drawn from this PhD work

as well as recommendation regarding future work.

2 Fundamental Background

This chapter gives a theoretical background of Heusler compounds, analysis of modulated structure using $(3+1)-D$ superspace group approach and MCE. The modulated structure in Ni-Mn based Heusler compounds can be explained by two models, adaptive phase model and soft phonon model [27, 30, 31, 32]. Ni-Mn based Heusler compounds exhibit giant MCE at the first-order phase transition which shows thermal as well as magnetic hysteresis. Hysteresis in these materials creates irreversibility for the succesive magnetic field cycles, which reduces the efficiency of solid-state energy efficient refrigerants. Recently, James and co-workers [33] have shown that this hysteresis can be reduces by approaching the GCC. In this thesis, GCC has been explained for different kind of austenite and martensite phases. After that, detailed thermodynamics of MCE with the measurement methods has been explained. Finally, a chapterwise overview of this thesis is given.

2.1 Heusler Compounds

In the 19th-century, a German mining engineer and chemist discovered the first ferromagnetic Heusler compound Cu_2MnAl [31, 32]. Nowadays more than 1500 Heusler compounds can be prepared and are shown for different fields. The structure of Heusler compounds [X_2YZ (full Heusler, $L2_1$ cubic crystal structure) and XYZ (half Heusler, $C1_b$ cubic structure)] are shown in Fig. 2.1(a) and (b) respectively [32]. The Wyckoff positions for full Heusler are $8c$ $(\frac{1}{4}, \frac{1}{4}, \frac{1}{4})$ X atom, $4a$ $(0, 0, 0)$ Y atom and $4b$ $(\frac{1}{2}, \frac{1}{2}, \frac{1}{2})$ Z atom, whereas the Wyckoff positions for half Heusler are $4a$ $(0, 0, 0)$ Xatom, $4b$ $(\frac{1}{2}, \frac{1}{2}, \frac{1}{2})$ Y atom and $4c$ $(\frac{1}{4}, \frac{1}{4}, \frac{1}{4})$ Z atom. The detailed study of crystal structure is essential in order to understand the properties and to correlate the theoretical prediction with experimental results. Interestingly, the properties of many Heusler compounds can be predicted only

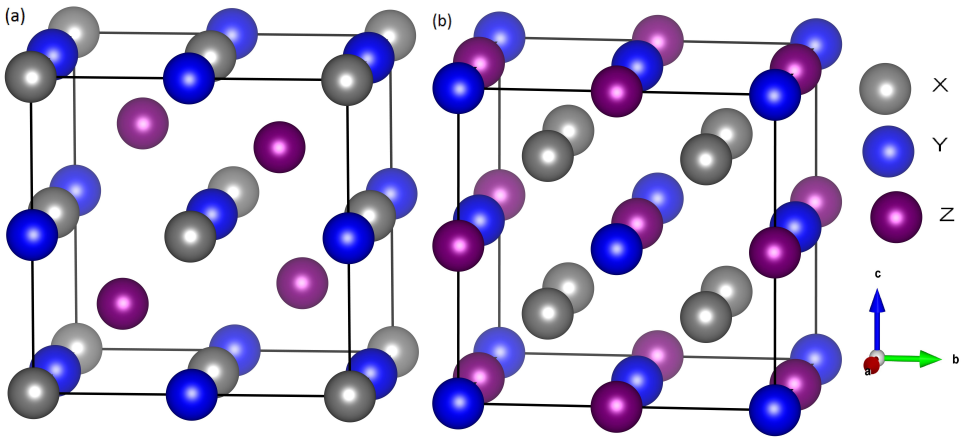

Figure 2.1: *Heusler crystal structures (a) half Heusler ($C1_b$) and (b) full Heusler ($L2_1$) drawn by vesta software.*

by counting the number of valence electrons. Nonmagnetic Heusler compounds with 27 valence electrons are superconducting. Intermetallic Heusler compounds are an exciting class of materials from both fundamental and application point of view. For full Heusler compounds X_2YZ, there are four formula units per unit cell. So, the magnetic moment in terms of Bohr magnetons, μ_{B}, is given by:

$$m_{xyz} = N_V - 24 \tag{2.1}$$

In half Heusler compounds, there are three formula units per unit cell results in magnetic moment in Bohr magnetons μ_B by:

$$m_{xyz} = N_V - 18 \tag{2.2}$$

where, N_V is the number of valence electrons [32].

Heusler compounds show fascinating scientific phenomena and fundamental properties such as superelasticity, giant-caloric (magneto-, baro- and elastocaloric) effects [12, 34], spin glass behavior [35], large magnetoresistance [36], large perpendicular magnetic anisotropy [37], large canting angle between magnetic moments [38] and exchange bias effect [39, 40, 41, 42]. These properties make them promising for novel application in the field of energy conversion, sensor and actuator devices [15]. Ni-Mn based Heusler compounds are one

group of materials showing all these properties. The functional properties in these Heusler compounds are associated with first-order diffusionless martensitic phase transition, during which the high temperature and high symmetry cubic austenite $L2_1$ phase transforms to low temperature and low symmetry martensite phase. The low temperature composition dependent martensite phase may be tetragonal, orthorhombic, or monoclinic [32, 43]. To choose a suitable compound for MCE from Heusler family, there are some properties to keep in mind. The suitable material for MCE should have first-order phase transition with negligible hysteresis and large magnetic moment. The first-order martensitic transition should also be sharp. The materials which show all these properties will result in large isothermal and adiabatic temperature change i.e. large MCE. Usually, the magnetic moment in Heusler compounds can be understood from the Slater-Pauling rule [28, 31, 32].

In 1996, the discovery of large magnetostrain in a single crystal of stoichiometric composition Ni_2MnGa had drawn attention to Ni-Mn based Heusler compounds [44, 45]. A magnetic field induced strain of $\approx 0.2\%$ was observed in Ni_2MnGa. Later, a large strain of $\approx 10\%$ was observed in a slightly different composition of Ni-Mn-Ga by applying the magnetic field of 1 T under ambient pressure [46]. The larger value of strain in Ni-Mn-Ga in comparison to other materials like lead-zirconate-titanate (PZT) and rare earth materials made them more feasible in the applications of actuators and sensors [47]. During the same time, the MCE was also observed in off-stoichiometric composition of Ni-Mn-Ga [48, 49]. Recently, both the direct and inverse MCE was observed in Ni_{2+x}-Mn_{1-x}-Z (Z=Sn, In, Sb) based Heusler compounds [29, 50, 51]. Direct MCE means that the sample heats up under the application of a magnetic field, whereas if it cools down by applying magnetic field, it is called inverse MCE. The advantage of Ni-Mn based Heusler compounds is that they do not include a rare earth element. Furthermore, the transition temperature in these materials can be tuned in broad temperature window by changing composition and annealing temperature [52]. The annealing temperature also plays an important role in determining the crystal structure. For instance, $Ni_2Mn_{1.4}In_{0.6}$ crystallizes in a cubic lattice i.e. no structural transformation including structural transformation from cubic to monoclinic modulated structure for different annealing temperatures occurs [12, 29, 53].

2.1.1 Magnetocaloric Materials

MCE is intrinsic to all magnetic materials. However, this value will be high at the first and second-order phase transition. For first-order phase transition both lattice entropy (due to the structural phase transition) and magnetic entropy contributes to MCE whereas only magnetic spin alignment participates in second-order phase transition. The large MCE around RT in Gd and $Gd_5Si_2Ge_3$ revived scientific and technological interest in magnetic refrigeration [16]. The drawback for Gd based materials was that they contain heavy rare earth elements, which are very expensive. As an alternative, La $(Fe, Si)_{13}$ was developed, including the rare earth element La which is more abundant and cheaper than Gd [20, 21]. The MCE and transition temperature in this material can be tuned by varying the composition or adding of Co, Mn and interstitial H [23, 24, 26]. The MCE was also observed in Mn-Fe-P-As based systems, but they include toxic As. However, the toxic As was replaced by Si and Ge [22, 25].
Among the promising materials studied for MCE, Ni-Mn based Heusler compounds are most attractive candidates with first-order magnetostructural phase transitions. The magnetostructural transition temperature T_M and Curie temperature T_C of these compounds can be widely adjusted by doping with Co, Fe or Cu [12]. The first-order martensitic transition in Heusler compounds is composition dependent. Fig. 2.2 shows the adiabatic temperature change at T_C and T_M for different kind of materials. The potential materials should have the following characteristics:
(a) large magnetic moment,
(b) little to no thermal and magnetic hysteresis,
(c) environment friendly material,
(d) affordable, abundant and easily synthesized material,
(e) large MCE near RT at reasonable magnetic field (H $<$ 2 T),
(f) little to no thermal expansion and contraction,
(g) appropriate thermal conductivity and electrical resistivity to minimize eddy currents,
(h) solubility (low brittleness, corrosion and solubility).
Figure 2.3 shows the value of adiabatic temperature for different kind of materials at a magnetic field of 2 T.

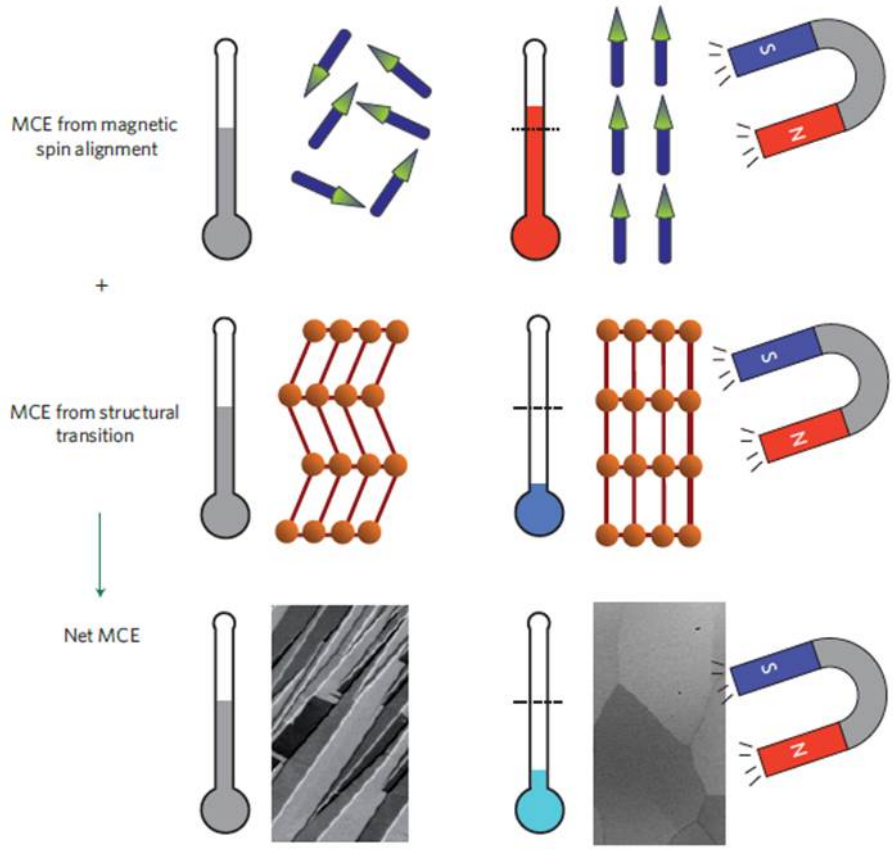

Figure 2.2: *Schematic shows the MCE contributions (lower part) from the magnetic (upper part) and structural part (middle part) of first-order phase transition. 'S' is the south pole and 'N' is the north pole of a magnet. Taken from Ref. [12].*

2.2 Modulated Structure

Interestingly, Ni-Mn based Heusler compounds show the modulated structure in the low temperature martensite phase [34, 54, 55]. Modulated structures are defined as such in which atoms or group of atoms are shifted or rotated with respect to their neighbors so that the three-dimensional translational symmetry is broken. However the shifts and rotations in modulated structure are

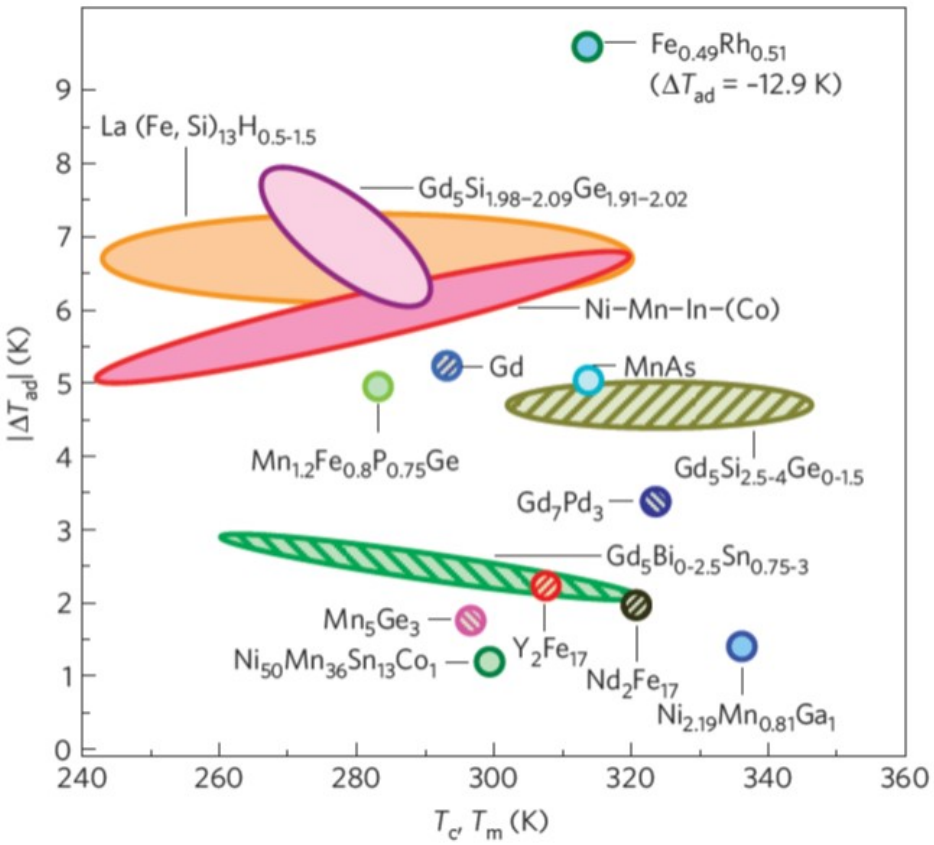

Figure 2.3: *Adiabatic temperature change at T_C (second-order phase transition, hatched pattern) and T_M (first-order phase transition, solid fill pattern) for different kind of magnetic materials at 2 T magnetic field. Taken from Ref. [12].*

not arbitrary; they follow an additional periodicity which can be described by atomic modulation functions (AMFs). AMFs are continuous, so that they can be expressed by combination of sine/cosine wave.

$$u_j(\bar{x}_4) = \sum_{n=1}^{\infty}[A_n^j \sin(2\pi n\bar{x}_4 + B_n^j \cos(2\pi n\bar{x}_4] \tag{2.3}$$

Here, A_n^j and B_n^j are the Fourier amplitudes of the displacement modulation of the jth atom and "n" is the order of the Fourier series, which is taken as equivalent to the order of the satellite reflections.

The additional periodicities of modulated structure results in additional sharp

peaks in the diffraction pattern, just as Bragg reflections due to the periodic term of three dimensional crystals. These additional peaks are known as satellite reflection and the intensity of these satellite reflections are weaker than main reflections. The positions of Bragg reflections for modulated structure are given as

$$Q = ha^* + kb^* + lc^* + mq = H + mq \tag{2.4}$$

Here, **q** is modulation vector, given as: $q = q_1a^* + q_2b^* + q_3c^*$ and m is the order of satellite reflection (m = 1, 2, 3.....).
If all **q**′s are rational then the structure is commensurate and if at least one of them is irrational then the structure is incommensurate [56].
The modulated structure has lower twinning stress, which results in small interfacial energy at magnetostructural transition. So, an easy movement of twin boundary from the low temperature martensite to high temperature austenite phase takes place. This energy barrier is manifested in term of latent heat and thermal/magnetic hysteresis of transition. Smaller energy barrier leads to improved reversible MCE [34]. Therefore, the current research in MCE focuses on minimizing the thermal hysteresis to improve reversibility and thus the efficiency of prospective applications.
In literature, two models are proposed to explain the modulated structure. One is the adaptive phase model and another is the soft phonon model. In adaptive phase model, the modulated structure is considered as a nanotwinned state of Bain distorted phase. All the atoms have uniform atomic displacement and modulation wave vector **q** is rational. So, the structure is commensurate. Whereas in soft phonon model, the modulated structure results from the phonon softening and all the atoms have non uniform atomic displacement with incommensurate nature of modulation. However, the modulated structure can be incommensurate because of nanotwinned state of Bain distorted phase [27, 55].

2.2.1 Analysis of Powder Diffraction Data

The powder diiffraction data analysis was done by Le Bail and Rietveld refinement using Jana2006 and FullProf software [57, 58, 59]. In 1967, H. Rietveld introduced a program which uses full information for least square refinement to match the observed and calculated intensities by adjusting the physical parame-

ters like unit cell parameters, temperature factor, atomic positions, composition, instrumental parameters as well as strain. The calculated peak intensities for the entire diffraction pattern are given by the following formula:

$$y_{ci} = S \sum L_k |F_k|^2 \phi(2\theta_i - 2\theta_k) P_k A + Y_{b(i)} \tag{2.5}$$

where, S is the scale factor, k represents the miller indices for h, k, l Bragg reflections. L_k contains the Lorentz, polarization and multiplicity factor. F_k denotes the structure factor for k^{th} Bragg reflection. The preferred orientation function is denoted by P_k and $Y_{b(i)}$ is the background intensity at the i^{th} step. The minimized function is:

$$\chi = \sum w_i (y_i - y_{ci})^2 \tag{2.6}$$

where, $w_i = 1/y_i$,
y_i = observed (gross) intensity at the i^{th} step.
y_{ci} = calculated intensity at the i^{th} step.
The powder diffraction reflection shape is influenced by both the sample and the instrument and varies as a function of 2θ. Among, the various peak shape functions, the most widely used shape is pseudo-Voigt. The pseudo-Voigt function is a linear combination of Lorentzian and Gaussian components in the following ratio.

$$pV = \eta L + (1 - \eta) G \tag{2.7}$$

where, η is the pseudo-Voigt mixing parameter. The full width at half maxima (FWHM) of Bragg peak is expressed as

$$(FWHM)^2 = U \tan^2 \theta + V \tan \theta + W \tag{2.8}$$

where, U, V and W are half width parameters, also knowns as profile shape parameters.
In Rietveld method, the quality of refinement between observed and calculated profile is measured by a set of some conventional factors, which are described as:

Profile factor:

$$R_p = \sum |(y_i - y_{ci})| / \sum |y_i| (2.9)$$

Weighted profile factor:

$$R_{wp} = [\sum w_i (y_i - y_{ci})^2 / \sum w_i (y_i)]^{1/2} \quad (2.10)$$

Expected weighted profile factor:

$$R_{exp} = [(N - P) / \sum w_i (y_i)^2]^{1/2} \quad (2.11)$$

where, N is the number of points that was used in the refinement, given as: $(N = N_{PTS} - N_{EXC})$
N_{PTS}: total number of points in the pattern,
N_{EXC}: total number of excluded points and P is the number of refined parameters.
Goodness of fit:

$$S = \frac{R_{wp}}{R_{exp}} \quad (2.12)$$

Reduced chi-Square:

$$\chi^2_\nu = [\frac{R_{wp}}{R_{exp}}]^2 \quad (2.13)$$

The best fit is observed when the value of χ^2_ν is close to 1. However, the reliability of fitting should be confirmed from the comparison of observed and refined pattern. Also, all physical parameters should be realistic. Before starting the refinement, it is important to have an approximate idea about the experimental condition (for example zero shift and resolution function of the instrument) and sample information (unit cell parameters and profile broadening function). To get realistic parameters, refinement should be done in sequence. In first step, lattice parameters and scale should be refined. After refining these parameters, other parameters should be refined by keeping the lattice parameters fixed to avoid possible large zero shift [57, 59, 60].
In 1988, A. Le Bail has introduced an idea that Rietveld method can be used to refine the reflection intensities without a structural model, which is known as Le Bail refinement. It requires only space group, approximate lattice parameters

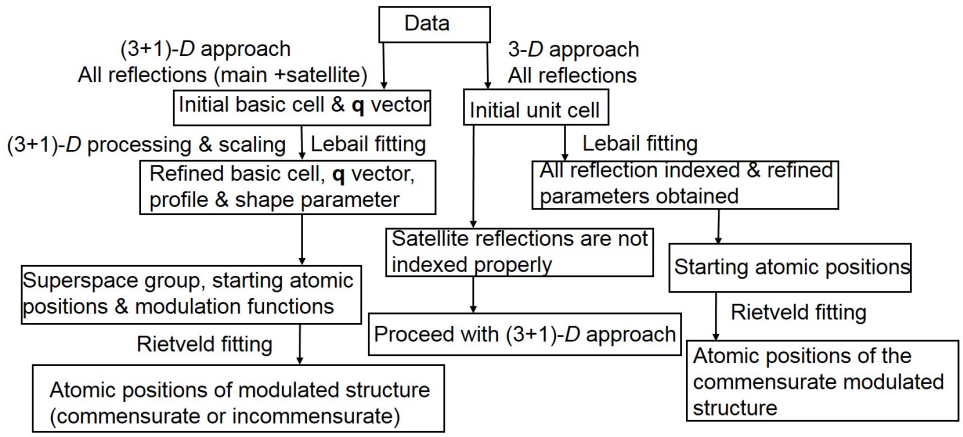

Figure 2.4: *Flowchart for the analysis of x-ray powder diffraction data for a modulated structure.*

and profile shape information. It is useful technique for samples with unknown crystal structure, where no information is reported in the literature. The data input for Le Bail fitting is much simpler and it enlarges the field of application for profile refinement. So, it is necessary to have information about the unit cell and profile shape parameters from Le Bail refinement before doing the Rietveld refinement [58].

Fig. 2.4 shows the procedure which was followed for the analysis of powder diffraction of modulated structure. In first step, the whole diffraction pattern was tried to fit with a $3-D$ structure. If Le Bail fitting index includes all Bragg peaks, then Rietveld fitting has been performed. For commensurate modulated structure, Rietveld fitting is satisfactory and the atomic positions are obtained [61]. If some of the Bragg peaks could not be indexed in the diffraction pattern then superspace $(3+1)-D$ approach is followed [62, 63]. In this approach, initially main reflections corresponding to the basic structure were indexed and then a $\mathbf{q}$ vector was provided to index the satellite reflections. Le Bail fitting is required to refine the basic unit cell and initial $\mathbf{q}$ value. After getting the best fit from Le Bail refinement, Rietveld refinement was used to refine the atomic position and amplitude modulation function. Once the best goodness of fit (GOF) is obtained, further analysis can be done to obtained other parameters such as nearest neighbour distance from t plot. Both commensurate and incom-

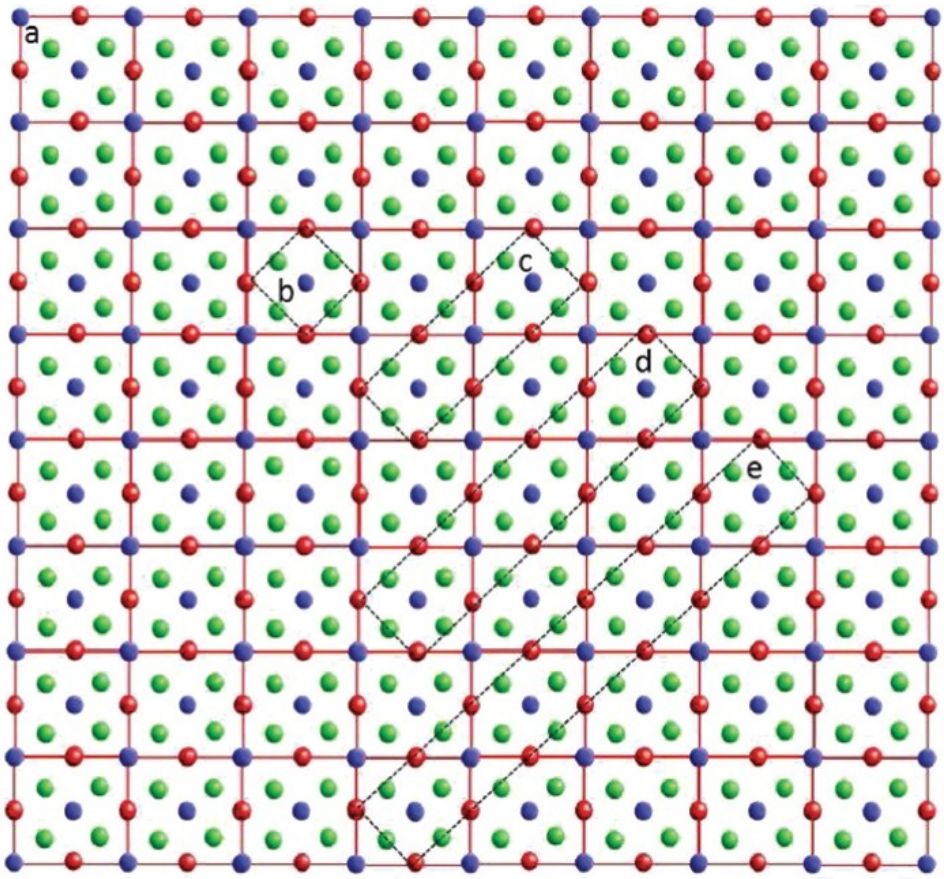

Figure 2.5: *Schematic of the unit cell for different kind of structures (a) austenite, (b) body centred tetragonal(bct) martensite, (c) 3M premartesite, (d) 5M marttensite and (e) 7M martensite superstructures. Taken from Ref. [34].*

mensurate modulated structure are analysed through $(3+1)-D$ approach [63]. Fig. 2.5 shows the unit cell for different kind of modulated structures. Ni-Mn based Heusler compounds show $3M$, $5M$ and $7M$ modulated structure. This representation is based on the number of satellite spots between the neighboring austenite peaks of $L2_1$ type austenite phase [27].

2.3 Geometric Compatibility Condition

Recently, James and co-workers [33, 64, 65, 66] have established a theoretical condition to reduce the hysteresis for improving reversibility of shape memory

alloys. The solid to solid first- order martensitic phase transformation is diffusionless. The lattice has different structure at higher and lower temperature. Since, the martensitic transformation is diffusionless. Therefore, there is no rearrangement of atoms and one structure can be obtained from the deformation of the other. As a consequence of thermal expansion, the lattice vectors depend upon temperature θ also. However, thermal expansion is negligibly small compared to the lattice distortion. Therefore, the lattice vector of austenite and martensite phase are related by a deformation. The relation between lattice vector is given as:

$$e_i^m = U e_i^a \tag{2.14}$$

Here, **U** describes the homogeneous deformation from austenite phase to martensite phase. This is called deformation matrix or Bain matrix. e_i^a is the lattice vector of austenite phase and e_i^m the lattice vector of martensite phase [67].

In general, the diffusionless martensitic transformation occurs by cooling the material that undergoes structural transition from a high symmetry austenite phase to low temperature martensite phase by shear deformation. The atoms move with respect to their neighbours. Therefore, it is also known as military transformation. To minimize the strain energy, an interface between the martensite and austenite phase become an undistorted and unrotated plane (invariant plane or habit plane). Mostly, shape memory alloys show cubic austenite to tetragonal, orthorhombic or monoclinic transformation. In this thesis, GCC has been discussed for cubic austenite to tetragonal, orthorhombic and monoclinic martensite phases [67].

2.3.1 Cubic Austenite to Tetragonal Martensite

If the transformation is from cubic austenite to tetragonal martensite, then there will be 3 martensite variants. This kind of transformation was observed in InTl disordered alloy [67]. It has face-centered cubic Bravais lattice in austenite phase and face-centered tetragonal lattice in martensite phase. The martensite variants for face-centered cubic to face-centered tetragonal described as follows:

$$\mathbf{U}_1 = \begin{pmatrix} \beta & 0 & 0 \\ 0 & \alpha & 0 \\ 0 & 0 & \alpha \end{pmatrix} \qquad \mathbf{U}_2 = \begin{pmatrix} \alpha & 0 & 0 \\ 0 & \beta & 0 \\ 0 & 0 & \alpha \end{pmatrix} \qquad \mathbf{U}_3 = \begin{pmatrix} \alpha & 0 & 0 \\ 0 & \alpha & 0 \\ 0 & 0 & \beta \end{pmatrix} \tag{2.15}$$

Here, the transformational stretches α and β are calculated from the lattice parameters of face-centered cubic austenite and face-centered tetragonal martensite phases. These transformational stretches are given as $\alpha = \frac{a_F}{a_0}$ and $\beta = \frac{c_F}{a_0}$, the superscript F stands for face-centered tetragonal structure [67].

All these matrices have the same determinant which represents the volume change between two phases. The compatibility between two phases is defined from the value of the determinant of transformation matrix [67, 68]. To be an exact compatible interface, the determinant of this transformation matrix should be one [67].

2.3.2 Cubic Austenite to Orthorhombic Martensite

In case of cubic to orthorhombic transformation, there are two types of transformation. One transformation may be described as follows: first cut a body centered tetragonal cell from two adjacent austenite cells and then stretch it unequally along the three edges of this tetragonal cell. By doing this, one will get the orthorhombic martensite unit cell. The second transformation from cubic to orthorhombic is described from the axes of orthorhombic symmetry, which is obtained from $\langle 110 \rangle$ cubic axes. The numbers of martensite variants in both cases are same i.e. 6. However, the deformation matrix will be different.
In first case, the deformation matrix is given as:

$$\mathbf{U}_1 = \begin{pmatrix} \delta & 0 & \epsilon \\ 0 & \beta & 0 \\ \epsilon & 0 & \delta \end{pmatrix} \qquad \mathbf{U}_2 = \begin{pmatrix} \delta & 0 & -\epsilon \\ 0 & \beta & 0 \\ -\epsilon & 0 & \delta \end{pmatrix} \qquad \mathbf{U}_3 = \begin{pmatrix} \delta & \epsilon & 0 \\ \epsilon & \delta & 0 \\ 0 & 0 & \beta \end{pmatrix}$$
$$\mathbf{U}_4 = \begin{pmatrix} \delta & -\epsilon & 0 \\ -\epsilon & \delta & 0 \\ 0 & 0 & \beta \end{pmatrix} \qquad \mathbf{U}_5 = \begin{pmatrix} \beta & 0 & 0 \\ 0 & \delta & \epsilon \\ 0 & \epsilon & \delta \end{pmatrix} \qquad \mathbf{U}_6 = \begin{pmatrix} \beta & 0 & 0 \\ 0 & \delta & -\epsilon \\ 0 & -\epsilon & \delta \end{pmatrix} \tag{2.16}$$

The above matrix elements are defined as: $\delta = \frac{\sqrt{2}(a+c)}{a_0}$, $\beta = \frac{b}{a_0}$, and

$\epsilon = \frac{\sqrt{2}(a-c)}{a_0}$ in an orthonormal basis parallel to the edges of the cubic unit cell [65].

There is another cubic to orthorhombic transformation in which the axes of orthorhombic symmetry are obtained from $\langle 110 \rangle$ cubic axes. However, this kind of transformation has not been observed so far in any material. The determinant and eigenvalues of these matrices are the same. To get an exact interface between cubic austenite and orthorhombic martensite, the determinant and middle eigenvalue of the transformation matrix should be one, which is known as GCC for cubic austenite to orthorhombic martensite phase [67].

2.3.3 Cubic Austenite to Monoclinic Martensite

There are two types of monoclinic martnsite transformation. One monoclinic martensitic transformation comes from $\langle 110 \rangle$ cubic transformation. Another one comes from the transformation in which the axis of monoclinic symmetry is along $\langle 100 \rangle$ cubic direction. The number of martensite variants from cubic austenite to monoclinic transformation are 12. The deformation matrix along $\langle 110 \rangle$ cubic direction is given as:

$$\mathbf{U}_1 = \begin{pmatrix} \gamma & \epsilon & \epsilon \\ \epsilon & \alpha & \delta \\ \epsilon & \delta & \alpha \end{pmatrix} \quad \mathbf{U}_2 = \begin{pmatrix} \gamma & -\epsilon & -\epsilon \\ -\epsilon & \alpha & \delta \\ -\epsilon & \delta & \alpha \end{pmatrix} \quad \mathbf{U}_3 = \begin{pmatrix} \gamma & -\epsilon & \epsilon \\ -\epsilon & \alpha & -\delta \\ \epsilon & -\delta & \alpha \end{pmatrix}$$

$$\mathbf{U}_4 = \begin{pmatrix} \gamma & \epsilon & -\epsilon \\ \epsilon & \alpha & -\delta \\ -\epsilon & -\delta & \alpha \end{pmatrix} \quad \mathbf{U}_5 = \begin{pmatrix} \alpha & \epsilon & \delta \\ \epsilon & \gamma & \epsilon \\ \delta & \epsilon & \alpha \end{pmatrix} \quad \mathbf{U}_6 = \begin{pmatrix} \alpha & -\epsilon & \delta \\ -\epsilon & \gamma & -\epsilon \\ \delta & -\epsilon & \alpha \end{pmatrix}$$

$$\mathbf{U}_7 = \begin{pmatrix} \alpha & -\epsilon & -\delta \\ -\epsilon & \gamma & \epsilon \\ -\delta & \epsilon & \alpha \end{pmatrix} \quad \mathbf{U}_8 = \begin{pmatrix} \alpha & \epsilon & -\delta \\ \epsilon & \gamma & -\epsilon \\ -\delta & -\epsilon & \alpha \end{pmatrix} \quad \mathbf{U}_9 = \begin{pmatrix} \alpha & \delta & \epsilon \\ \delta & \alpha & \epsilon \\ \epsilon & \epsilon & \gamma \end{pmatrix}$$

$$\mathbf{U}_{10} = \begin{pmatrix} \alpha & \delta & -\epsilon \\ \delta & \alpha & -\epsilon \\ -\epsilon & -\epsilon & \gamma \end{pmatrix} \quad \mathbf{U}_{11} = \begin{pmatrix} \alpha & -\delta & \epsilon \\ -\delta & \alpha & -\epsilon \\ \epsilon & -\epsilon & \gamma \end{pmatrix} \quad \mathbf{U}_{12} = \begin{pmatrix} \alpha & -\delta & -\epsilon \\ -\delta & \alpha & \epsilon \\ -\epsilon & \epsilon & \gamma \end{pmatrix} \tag{2.17}$$

These matrix elements are given as: $\gamma = \frac{a(\sqrt{2}a + c\sin\beta)}{a_0\sqrt{(2a^2+c^2+2\sqrt{2}ac\sin\beta)}}$,
$\epsilon = \frac{ac\cos\beta}{\sqrt{2}a_0\sqrt{2a^2+c^2+2\sqrt{2}ac\sin\beta}}$, $\alpha = \frac{1}{2\sqrt{2}a_0}(\frac{c(c+\sqrt{2}a\sin\beta)}{\sqrt{2a^2+c^2+2\sqrt{2}ac\sin\beta}} + b)$, and
$\delta = \frac{1}{2\sqrt{2}a_0}(\frac{c(c+\sqrt{2}a\sin\beta)}{\sqrt{2a^2+c^2+2\sqrt{2}ac\sin\beta}} - b)$.

whereas, the deformation matrix along ⟨100⟩ cubic direction is given as:

$$\mathbf{U}_1 = \begin{pmatrix} \tau & \sigma & 0 \\ \sigma & \rho & 0 \\ 0 & 0 & \beta \end{pmatrix} \quad \mathbf{U}_2 = \begin{pmatrix} \tau & -\sigma & 0 \\ -\sigma & \rho & 0 \\ 0 & 0 & \beta \end{pmatrix} \quad \mathbf{U}_3 = \begin{pmatrix} \rho & \sigma & 0 \\ \sigma & \tau & 0 \\ 0 & 0 & \beta \end{pmatrix}$$
$$\mathbf{U}_4 = \begin{pmatrix} \rho & -\sigma & 0 \\ -\sigma & \tau & 0 \\ 0 & 0 & \beta \end{pmatrix} \quad \mathbf{U}_5 = \begin{pmatrix} \rho & 0 & \sigma \\ 0 & \beta & 0 \\ \sigma & 0 & \tau \end{pmatrix} \quad \mathbf{U}_6 = \begin{pmatrix} \rho & 0 & -\sigma \\ 0 & \beta & 0 \\ -\sigma & 0 & \beta \end{pmatrix}$$
$$\mathbf{U}_7 = \begin{pmatrix} \tau & 0 & -\sigma \\ 0 & \beta & 0 \\ \sigma & 0 & \rho \end{pmatrix} \quad \mathbf{U}_8 = \begin{pmatrix} \tau & 0 & -\sigma \\ 0 & \beta & 0 \\ -\sigma & 0 & \rho \end{pmatrix} \quad \mathbf{U}_9 = \begin{pmatrix} \beta & 0 & 0 \\ 0 & \tau & \sigma \\ 0 & \sigma & \rho \end{pmatrix}$$
$$\mathbf{U}_{10} = \begin{pmatrix} \beta & 0 & 0 \\ 0 & \tau & -\sigma \\ 0 & -\sigma & \rho \end{pmatrix} \quad \mathbf{U}_{11} = \begin{pmatrix} \beta & 0 & 0 \\ 0 & \rho & \sigma \\ 0 & \sigma & \tau \end{pmatrix} \quad \mathbf{U}_{12} = \begin{pmatrix} \beta & 0 & 0 \\ 0 & \rho & -\sigma \\ 0 & -\sigma & \tau \end{pmatrix} \tag{2.18}$$

where, the matrix elements are defined as: $\tau = \frac{\alpha^2+\gamma^2+2\alpha\gamma(\sin\theta-\cos\theta)}{2\sqrt{\alpha^2+\gamma^2+2\alpha\gamma\sin\theta}}$, $\rho = \frac{\alpha^2+\gamma^2+2\alpha\gamma(\sin\theta+\cos\theta)}{2\sqrt{\alpha^2+\gamma^2+2\alpha\gamma\sin\theta}}$, $\sigma = \frac{\alpha^2-\gamma^2}{2\sqrt{\alpha^2+\gamma^2+2\alpha\gamma\sin\theta}}$, and $\beta = \frac{b}{a_0}$, $\alpha = \frac{\sqrt{2}a}{a_0}$, $\gamma = \frac{\sqrt{2}c}{Na_0}$.

The cubic lattice parameter is denoted as a_0, whereas a, b, c and β are lattice parameters of monoclinic unit cell. N is the degree of modulation. All these matrices give the same value of determinant as well as eigenvalues. The determinant represents the volume change and eigenvalue indicate the transformation stretch from one side relative to another. For an invariant habit plane between cubic austenite and monoclinic martensite, the middle eigenvalue of the transformation matrix should be one, which is known as GCC of monoclinic martensite phase [67].

2.4 History and Technology Advances of MCE

In 1905, Langevin predicted theoretically that a paramagnet should change its temperature under the application and removal of magnetic field [69]. After few years later, Weiss and Picard experimentally observed this effect in Ni, so called MCE [70]. To utilize this effect for cooling at low temperatures, further predictions have been made by Debye and Giaque [70]. Following this year, it was possible to reach temperatures below 1 K by using paramagnetic salts [71]. In 1976, Brown reached the next milestone for magnetic refrigeration [72]. He

built the first magnetocaloric demonstrator which was working at RT with a magnetic field of 7 T and can produce a temperature span of 47 K [72]. During that time, the magnetocaloric materials were not used as a regenerator which means that the temperature span was produced only in fluid and it was the same over its whole length. Following this, in 1982, Barclay and Steyert introduced the active magnetic regenerator (AMR) which uses magnetocaloric material to develop temperature gradient during operation, referred to as regenerator [73]. Large temperature spans can be achieved by using a simple layer or a stack of different magnetocaloric materials. Nowadays, every prototypical device works on the principle of AMR [5]. MCE is defined as heating or cooling of magnetic material in the presence of magnetic field and characterized by isothermal entropy ΔS_{iso} and adiabatic temperature change ΔT_{ad} [74]. Over the years the nature and behavior of MCE as a function of temperature and magnetic field is the subject of special interest for many experimental and theoretical studies [15, 69, 75, 76]. In recent past, the fundamentals of the MCE are developed quite well [15, 77]. Even today, research remains an important issue on the magnetothermal phenomenon from both theory and experiment point of view.

2.4.1 Thermodynamics of MCE

The MCE is the result of entropy variation arising from the coupling of the magnetic spin system of the solid in applied magnetic field. It is intrinsic to all magnetic materials. The total entropy, S_{tot}, of magnetic material is the sum of magnetic S_{Mag}, lattice S_{lat} and electronic S_{el} entropies at constant pressure [74].

$$S_{tot}(H,T) = S_M(H,T) + S_{lat}(H,T) + S_{el}(H,T). \tag{2.19}$$

In materials, where the magnetism is due to the localized magnetic moment, e.g. lanthanides, the total entropy is the sum of all three (S_{mag}, S_{lat}, and S_{ele}) entropies, respectively. However, in solids with itinerant magnetism and/or $3d$ magnetism the three contributions to the entropy is not straightforward. In Heusler materials, the magnetic entropy strongly depends on magnetic field, while lattice and electronic entropies are independent of magnetic field.

Suppose that, we have a piece of magnetic material and magnetic moments inside it are randomly oriented. There are two ways to apply the magnetic field (a) isothermal process and (b) adiabatic process. If we apply the magnetic field isothermally (T = const.), applied magnetic field would tend to align the magnetic moment and thus decreases the magnetic entropy $\Delta S_{\mathrm{mag}} < 0$. The decrease in magnetic entropy results in decrease for total entropy of the magnetic system $\Delta S_{\mathrm{tot}} < 0$. In an adiabatic process the total entropy of the system should remain constant (S_{tot} = const.). To fulfill this condition, $\Delta S_{\mathrm{tot}} = 0$, the lattice and electronic entropy must increase by $\Delta(S_{\mathrm{lat}} + S_{\mathrm{ele}}) = -\Delta S_{\mathrm{mag}}$. However, the contribution of electronic entropy is smaller in comparison to lattice entropy. The increase of lattice entropy results in temperature increment of the sample $\Delta T_{\mathrm{ad}} > 0$. Conversely when the magnetic field is removed, the magnetic moment tends to randomize. The randomization of magnetic moment results an increment in magnetic entropy and decrease in lattice entropy as well as sample temperature $\Delta T_{\mathrm{ad}} < 0$. Both isothermal and adiabatic processes are shown in Fig. 5.

Isothermal process is defined as $\Delta S_T = S(T, B) - S(T, 0) < 0$ whereas adiabatic process is given by the following equation $\Delta T_{\mathrm{ad}} = T(S, B) - T(S, 0) > 0$. In classical thermodynamics, a system can be characterized by various thermodynamic parameters such as pressure (P), temperature (T), and Gibbs free energy (G) associated with the system. If we apply a certain amount of heat dQ to the system, this heat will not only increase the temperature of the system but also increases its internal energy by dU, it will enable the system to perform some work, $dW = pdV$, on its environment and finally the magnetization may decrease due to the added heat, $-\mu_0 HdM$ [78]. From the first law of thermodynamics, the state of the system is given by:

$$dQ = dU + pdV - \mu_0 HdM. \tag{2.20}$$

According to the second law of thermodynamics for a reversible process,

$$dQ = TdS, \tag{2.21}$$

and by using Eq. (2.20) and Eq. (2.21), the internal energy change for a magnetic

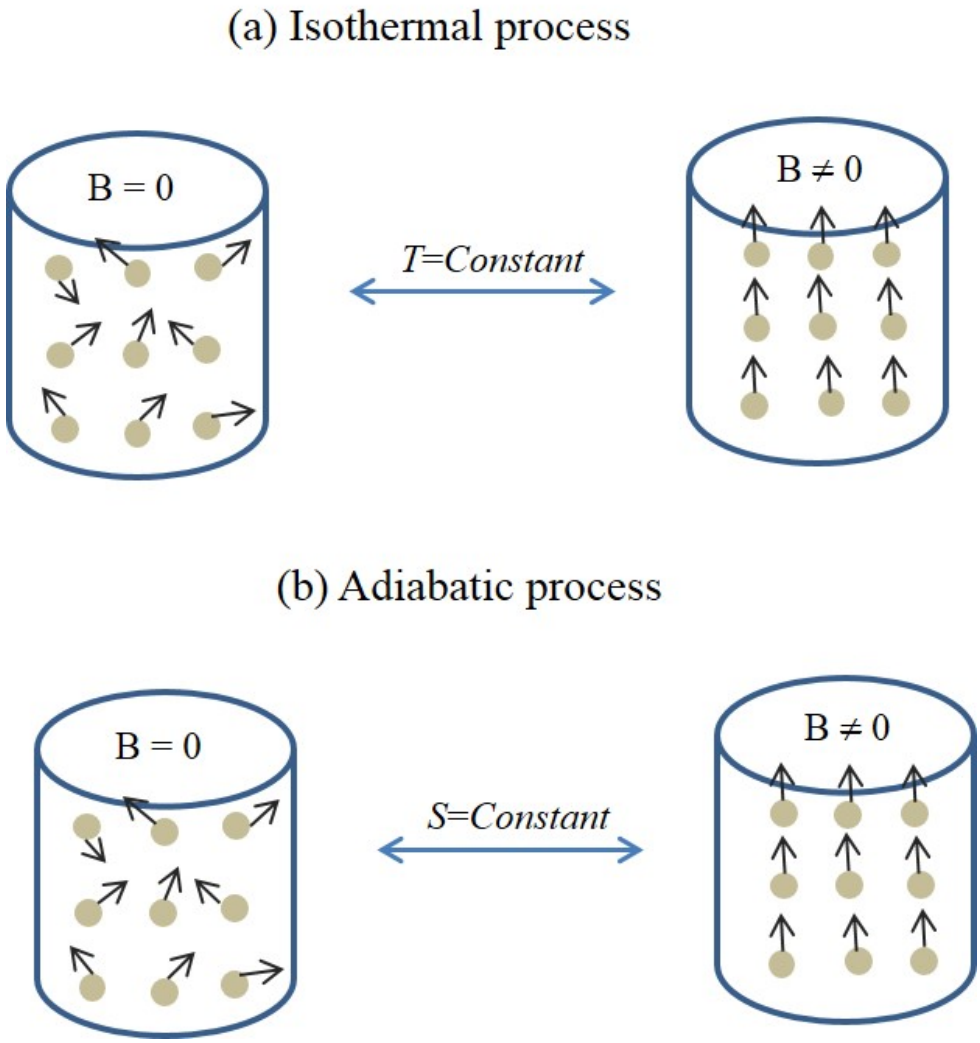

Figure 2.6: *Schematic of (a) isothermal and (b) adiabatic process of the magnetocaloric effect. Isothermal process (T = const.) leads to a negative entropy change ΔS_M, while adiabatic process (S = const.), gives a positive change in temperature ΔT_{ad} under the application/removal of magnetic field.*

material is expressed by:

$$dU = TdS - pdV + \mu_0 HdM. \tag{2.22}$$

The measurement of entropy is difficult because it contains the term TdS. So, it is more convenient to express the energy by using parameters such as T, p,

and H. Thus, the Gibbs free energy is defined as:

$$G \equiv U + pV - TS - \mu_0 HM. \tag{2.23}$$

By taking the differential of Eq. (2.23) and inserting the internal energy, dU, from Eq. (2.22), the Gibbs free energy can be expressed as

$$\begin{aligned} dG &= dU + pdV + Vdp - (TdS + SdT) - (\mu_0 HdM + \mu_0 MdH) \\ &= TdS - pdV + \mu_0 HdM + pdV + Vdp - TdS - SdT - \mu_0 HdM - \mu_0 MdH \\ &= -SdT + Vdp - \mu_0 MdH. \end{aligned} \tag{2.24}$$

Hence, we obtain

$$S = -\left(\frac{\partial G}{\partial T}\right)_{p,H} \tag{2.25}$$

and

$$M = -\frac{1}{\mu_0}\left(\frac{\partial G}{\partial H}\right)_{p,T}. \tag{2.26}$$

From an elementary theorem of calculus, two mixed second partial derivatives of G with respect to T and H are equal. According to Maxwell, the relation between the temperature derivative of the magnetization and the field derivative of the entropy is given by

$$\begin{aligned} \frac{1}{\mu_0}\left(\frac{\partial S}{\partial H}\right)_{p,T} &= -\frac{1}{\mu_0}\frac{\partial}{\partial H}\left(\frac{\partial G}{\partial T}\right)_{p,H} \\ &= -\frac{\partial}{\partial T}\left(\frac{1}{\mu_0}\frac{\partial G}{\partial H}\right)_{p} \\ &= \left(\frac{\partial M}{\partial T}\right)_{p,H}. \end{aligned} \tag{2.27}$$

By integrating both sides and rearranging the terms in Eq. (2.27), the isothermal magnetic entropy change under varying magnetic field, $\Delta H = H_F - H_I$, is given

by

$$\Delta S_M(T, \Delta H) = \mu_0 \int_{H_I}^{H_F} \left(\frac{\partial M}{\partial T}\right)_{p,H} dH. \tag{2.28}$$

This equation indicates that the magnetic entropy change is proportional to the derivative of the magnetization with respect to temperature at constant field and to the field variation. The differential of the total entropy, $S_{\mathrm{tot}}(H, T)$, can be written as

$$dS = \left(\frac{\partial S}{\partial T}\right)_{p,H} dT + \left(\frac{\partial S}{\partial H}\right)_{p,T} dH. \tag{2.29}$$

On the other hand, the heat capacity, C_{x}, is defined as

$$C_x = \left(\frac{\partial Q}{\partial T}\right)_x, \tag{2.30}$$

where x is the constant parameter. By using the second law of thermodynamics, $dQ = TdS$, the heat capacity can be represented as

$$C_x = T\left(\frac{\partial S}{\partial T}\right)_x. \tag{2.31}$$

Considering an adiabatic process ($dQ = TdS = 0$) and by using above Maxwell relation (Eq. (2.27)) and Eq. (2.31), due to a change in magnetic field, the temperature change is expressed as

$$dT = -\mu_0 \frac{T}{C_{p,H}} \left(\frac{\partial M}{\partial T}\right)_{p,H} dH. \tag{2.32}$$

Now, by integrating Eq. (2.32) from the initial field H_I to the final field H_F, the adiabatic temperature change is given by

$$\Delta T_{ad}(T, \Delta H) = -\mu_0 \int_{H_I}^{H_F} \frac{T}{C_{p,H}} \left(\frac{\partial M}{\partial T}\right)_{p,H} dH. \tag{2.33}$$

By analyzing Eqs. (2.28) and (2.33), some general information about the behavior of the MCE in solids with a second-order phase transition can be

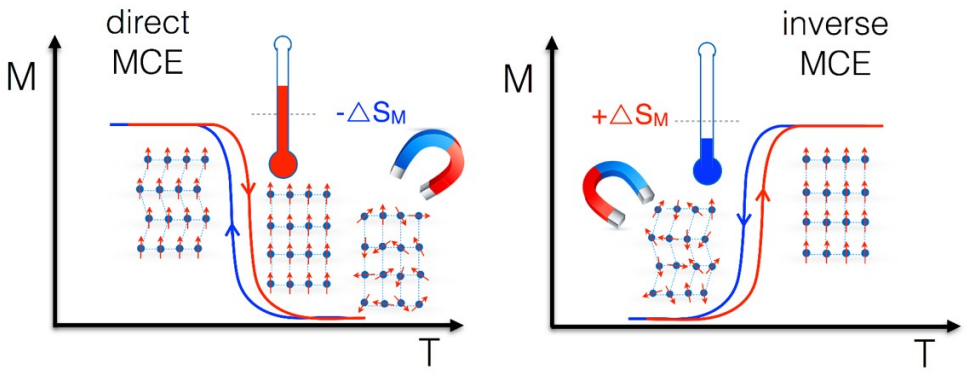

Figure 2.7: *Schematic diagram of the temperature dependence of direct and inverse MCE with thermal hysteresis in Heusler compounds.*

achieved [79, 81].

2.4.2 Direct (Conventional) and Inverse MCE

If the sample temperature increases by applying a magnetic field, it is called direct or conventional MCE whereas, if the sample temperature decreases upon the application of magnetic field, this is called inverse MCE. In Ni-Mn based MSM Heusler compounds, the occurrence of temperature change with magnetic field not only depends on the rapid change of magnetization with temperature but also on the shift of first-order magnetostructural transition temperature T_{tr} induced by applying an external magnetic field. If the magnetic field is applied adiabatically to a sample initially at temperature T_i, the magnetic field causes it to warm up to a final temperature T_f with increase in T_{tr} called conventional MCE. On the otherhand, the adiabatic application of magnetic field to a sample at T_i causes it to cool to T_f with decrease in T_{tr}, known as inverse MCE. Both effects rely on the shift in T_{tr} on applying magnetic field [79, 81].

2.4.3 Magnetic Refrigeration Process

Figure 2.8 shows the schematic for magnetic refrigeration cycles. The process completes in four steps.

In step (a) we have a piece of magnetic material. All the spins are randomly oriented in the absence of a magnetic field. As the process moves from (a) to

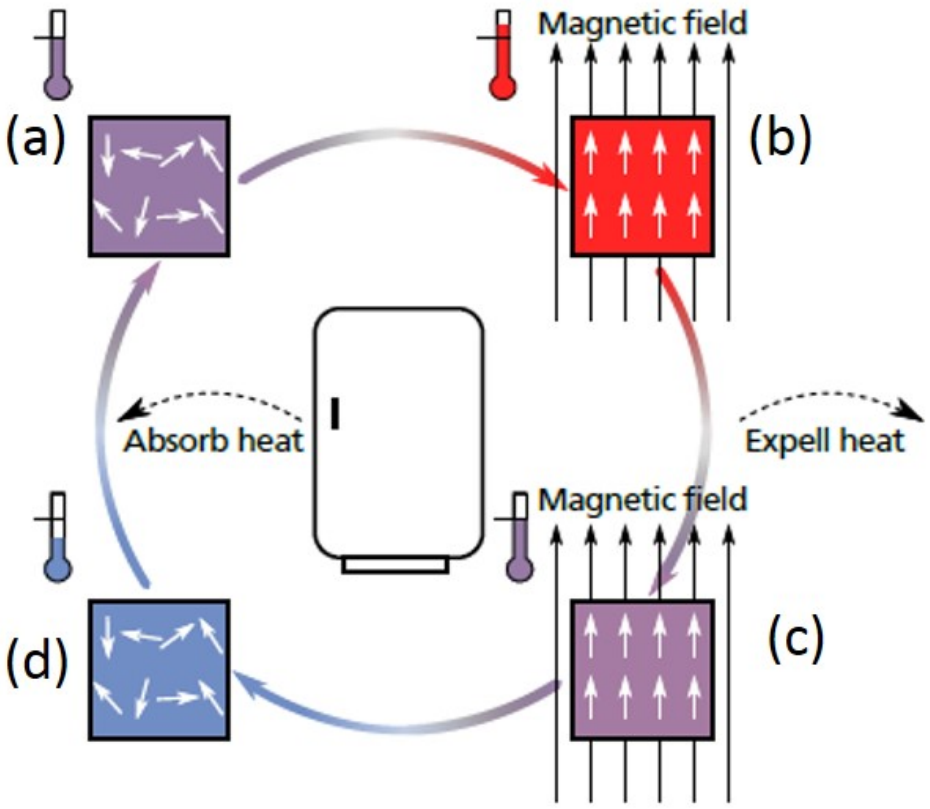

Figure 2.8: *Schematic of the magnetic refrigeration cycle. Taken from Ref. [28].*

(b) the spins get aligned by applying a magnetic field under adiabatic condition and as a result the temperature of the sample increases because of the MCE. When the process moves from (b) to (c), then the absorbed amount of heat is removed by water or fluid like helium and it comes again to temperature T. In the last steps from (c) to (d) the temperature of the sample decrease after removing the magnetic field because of MCE. At stage (d) the sample is cold enough to take heat from environment or external load. In this way one cycle completes and again a new cycle starts [5].

2.5 Measurements of the MCE

The MCE can be measured in two ways. (a) Direct measurement and (b) Indirect measurement. These two methods are described as follows:

2.5.1 Direct Measurements

Direct methods are defined as the temperature difference of the initial (T_{I}) and final (T_{F}) temperatures of a material while the external magnetic field is varied from an initial (H_{I}) to a final value (H_{F}) under adiabatic condition. For direct measurement, the sample temperature change can be monitored either contact technique, i.e., a direct thermal contact between sensor and the sample, suitable for strong magnetic field and large temperature changes,[82, 83, 84], or non-contact technique, which is based on the thermoacoustic principle. A sample with a periodically changing surface temperature induces exponentially decaying pressure waves which can be detected by a sensitive microphone. It is suitable for weak magnetic fields and small temperature difference [17, 85]. Direct measurement requires adiabatic condition which needs a sufficiently fast magnetic-field change. Two common ways to accomplish these measurement are: (1) measurements on fixed samples by changing the magnetic field (i.e., charging/discharging the magnet) [83] and (2) by moving the sample in and out of a constant magnetic field [84]. The electromagnet produces a magnetic field strength of 2 T. The permanent or superconducting magnets limits the magnetic field range to $0.1 - 10$ T [17]. In this thesis, ΔT_{ad} has been measured directly using a contact technique (sample surface is connected with the thermocouple) in pulsed magnetic fields up to 50 T with a magnetic field rate of 2000 T/s. This technique is described in chapter 3.

2.5.2 Indirect Measurements

Direct MCE measurements, give only the adiabatic temperature change while indirect techniques allow: (1) the calculation of both ΔT_{ad} and ΔS_{M} from an experimentally measured heat capacity and (2) the calculation of ΔS_{M} from magnetization measurements [17].

Most of the MCE studies are based on magnetization measurements by measuring $M(T)$ at different magnetic fields and $M(H)$ at different temperatures [113, 114, 116]. These magnetization curves are used to calculate ΔS_{M} by numerical integration of Eq. (2.28). An estimated error of ΔS_{M} calculated from $M(T)$ and $M(H)$ measurements depends on the accuracy of the magnetic moment measurements as well as the magnetic-field and temperature intervals. Thus, the numerical integration and replacing the exact differentials in Eq. (2.28) ($\mathrm{d}M$, $\mathrm{d}T$, and $\mathrm{d}H$) by the measured variations (ΔM, ΔT, and ΔH), the error using this technique is in the range of $3-10\%$ [86].

A complete characterization of the MCE is provided by measuring the heat capacity as a function of temperature in constant magnetic fields, $C(T)_H$. The entropy can be calculated by using Eq. (2.34) as:

$$\begin{aligned} S(T)_{H_I} &= \int_0^T \frac{C(T)_{H_I}}{T} dT + S_{0,H_I} \\ S(T)_{H_F} &= \int_0^T \frac{C(T)_{H_F}}{T}\, dT + S_{0,H_F}, \end{aligned} \tag{2.34}$$

where S_{0,H_I} and S_{0,H_F} are the zero-temperature entropies. In a condensed system $S_{0,H_I} = S_{0,H_F}$ [87]. Therefore, both $\Delta T_{\mathrm{ad}}(T)$ and $\Delta S_{\mathrm{M}}(T)$ can be obtained by $\Delta T_{\mathrm{ad}}(T) \approx [T(S)_{H_F} - T(S)_{H_I}]$ and $\Delta S_{\mathrm{M}}(T) \approx [S(T)_{H_F} - S(T)_{H_I}]$, respectively [17, 88, 89]. The accuracy of both $\Delta S_{\mathrm{M}}(T)$ and $\Delta T_{\mathrm{ad}}(T)$ measurements calculated from heat-capacity data depends on the accuracy of the $C(T)_H$ measurements.

3 Experimental Fabrication and Characterization Techniques

To study the condensed matter physics, the first step to take is the synthesis of materials. Bulk polycrystalline materials were prepared and characterized concerning the modulation and their MCE study from various techniques are presented in this thesis. Polycrystals have random crystalline orientation which facilitates the observation of all possible diffraction peaks in powder x-ray diffraction. The averaged temperature dependent magnetization behavior for polycrystalline materials is closer to an ideal Curie-Weiss behavior in comparison to single crystals [90]. Polycrystalline MSM Heusler compounds were prepared by arc melting and induction melting techniques and then characterized by the measurement techniques as described in this chapter.

3.1 Sample Preparation Methods

The studied polycrystalline Heusler samples were prepared by both arc melting and induction melting techniques under an Ar atmosphere from high purity elements (99.99%). In order to keep the final composition nominal, an excess amount of 2-3% Mn was added because of the high vapor pressure of Mn for arc melting. However, there is no need for excess amount of Mn in case of induction melting. To ensure the homogeneity, as-cast ingots were turned and remelted 5 times. After melting the ingot, the observed mass loss was negligibly small (less than 1%). The prepared ingots after melting were wrapped inside Mo foil to prevent oxidation and placed inside a quartz tube under an Ar atmosphere of 2 mbar and subsequently annealed at different temperature 700 - 900°C and 1-5 days for the required phase formation.

3.1.1 Arc Melting

The arc melting furnace consists of four main sections: the chamber, the vacuum pump (turbo pump), the water and the electrical power supply. The chamber contains four copper stages. In the first step the copper stages are disconnected from the chamber and cleaned by alcohol and sandblasting. One of the copper stages is loaded with Ti as getter to prevent oxidation. The other three copper stages are loaded with weighed materials, usually consisting of granules and foil to be melted and are reconnected with the chamber. Afterwards the system is evacuated and then filled by Ar three times. Then a small pressure of Ar is filled into the chamber before power supply and water supply was turned on. The water supply was used to cool the copper stages. The tungsten tip is lowered to touch the material on the copper stage and the tip is constantly moved uniformly over the whole area containing the material. The melted ingots are turned over and remelted three times to achieve a homogeneous ingot. After melting, the electric power supply was turned off and later on the water supply was also turned off when the ingots were cooled down. The melted ingots were taken out from the chamber. This technique allows to achieve the temperatures up to 3000°C.

3.1.2 Induction Melting

Induction melting is a simple technique that can be used to melt intermetallic materials with lower melting points. It is in combination with a radiofrequency generator, that produced the heat which melts the samples. Some of the studied samples in this thesis were prepared by induction melting. Central part of our induction melting is a horizontal cold boat furnace with radio frequency induction placed inside the glove box. The water cooling and a rough pump is connected from outside to prevent the cold boat from melting and to reduce the reactivity during the sample melting. To melt the sample, the quartz glass tube, the weighed sample and the alumina (Al_2O_3) crucibles were placed inside the glove box. The quartz tube in which the alumina crucible containing the melting material was positioned inside the cold boat and then melted for obtaining the ingot.
Various measurement techniques have been utilized to study the structure, ther-

mal, magnetic and electronic properties of the prepared materials. These techniques are described below.

3.2 Structural Characterization

The crystallographic structures of the prepared powder samples were determined using x-ray diffraction (XRD). Prior to XRD measurements, the material was crushed into a fine powder with an agate mortar, sieved down to < 50 µm and annealed at 500°C temperature to remove the stress generated during grinding [34]. This annealed powder was homogeneously dispersed on a Mylar foil with the help of petroleum jelly in hexane.
Fig. 3.1 illustrates the kinematic interpretation of XRD. A beam of monochromatic x-ray is incident upon a crystal with lattice planes separated by a distance d. The incident beam is reflected by each plane with the path difference $2d\sin\theta$ between two adjacent planes. When the reflected radiation constructively interferes, the Bragg condition is satisfied.

$$n\lambda = 2d\sin\theta. \tag{3.1}$$

where, n is an integer and represents the order of the corresponding reflection. λ is the wavelength of the incident x-ray beam. d is the distance between two adjacent lattice planes. The Bragg reflection is only possible when $\lambda \leqslant 2\,d$. XRD data for powder samples was measured at RT using an image-plate Huber G670 Guinier camera equipped with a Ge (111) monochromator and Cu K_α radiation of wavelength $\lambda = 1.54$ Å in the range of $3° \leq 2\theta \leq 100°$. Initial indexing of XRD pattern for lattice parameters was done by PowderCell package [91]. LaB_6 (NIST SRM 160a, $a = 4.15691$ (8)Å) was used as an internal standard [92]. The temperature dependent XRD for powder sample was done using StadiP (Stoe & Cie. GmbH) diffractometer. The wavelength of radiation for XRD was Mo K_{α_1} $\lambda = 0.70930$ Å. Before doing XRD, the powder samples were annealed at 700°C.

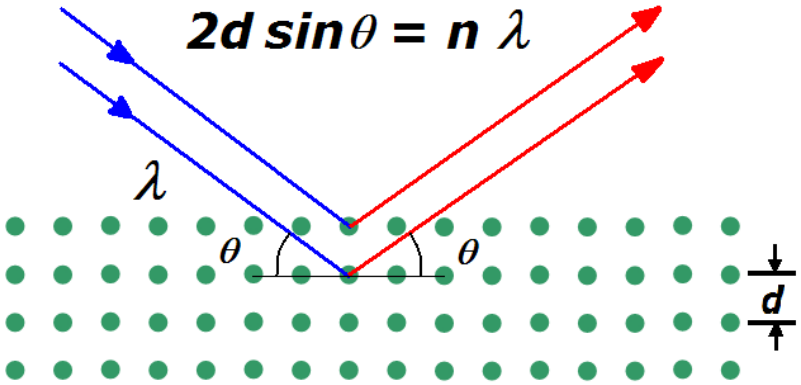

Figure 3.1: *Schematic of Bragg's diffraction law. Two beams with identical wavelength and phase approach a crystalline solid and scattered from different atoms of different plane within it. Taken from Ref. [27].*

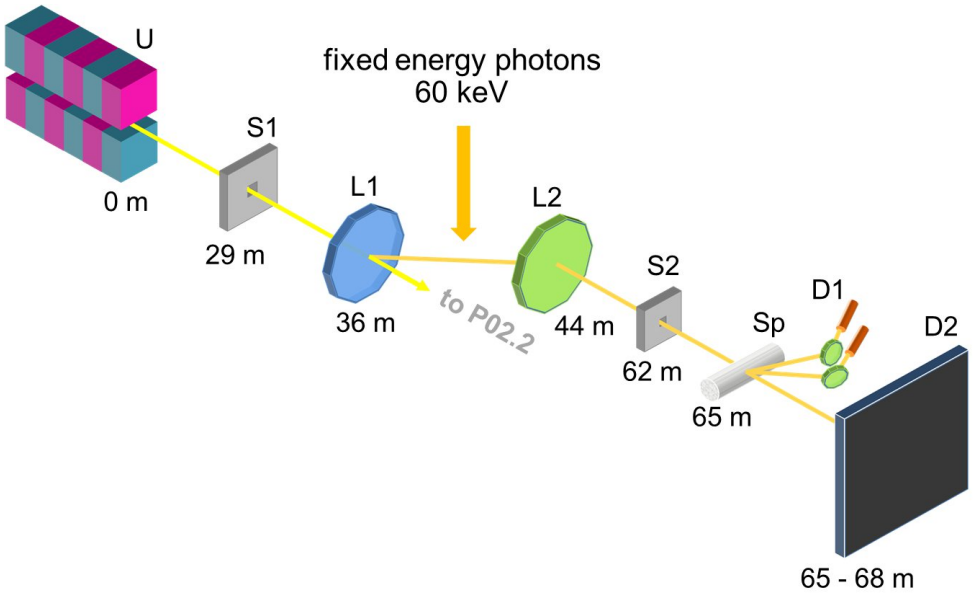

Figure 3.2: *Schematic diagram of the optics of high resolution powder diffractometer (HRPD) set up. Taken from Ref. [27].*

3.2.1 (a) Synchrotron X-ray Powder Diffraction (SXRPD)

Fig. 3.2 shows the schematic of the optics of high resolution powder diffractometer (HRPD) beamline which has undulator U, Laue monochromator crystals (L1,

L2), slit systems (S1, S2), Sp (sample e.g. powder in capillary) and detectros (D1, D2).
The results of SXRPD in this thesis were obtained at DESY Hamburg. The advantages of SXRPD are the high spatial resolution, high sample penetration and high data collection speed compare to laboratory XRD. The high resolution of synchrotron XRD is able to split the modulated peaks. The working process of SXRPD given as: A heated tungsten cathode produced the electrons from electron gun by thermionic emission. These emitted electrons are accelerated by potential difference of 60 kV to the energy of 60 keV (corresponding to wavelength of (0.207 Å)) applied across the gun and move into the linear accelerator. The linear accelerator accelerates the electron beam to a higher energy value of 100 MeV over a distance of about 10 meters. The booster of circumference 130 m is an electron synchrotron that takes the beam from the linear accelerator and increases its energy to 3 GeV. This beam of higher energy is then further accelerated by simultaneous ramping of magnet strength and cavity fields. The final destination for accelerated electrons is the storage ring which can hold 200 mA of stored ring with a beam lifetime of over 20 hours. The focus and selection of appropriate wavelength was done from the photon delivery system which incorporates filters, mirrors, monochromators, attenuators and other devices [93].

3.2.2 (b) Pressure Dependent X-ray Powder Diffraction

Pressure dependent XRD measurements performed in austenite and martensite phase reported in this thesis were performed at the XDS beamline of the Brazilian synchrotron light laboratory. The annealed powder was sieved for the particle size under 10 μm and loaded in diamond anvil cell. The pressure inside the sample space was determined from the fluorescence lines of small ruby grains, which were loaded along with the sample. A mixture of four-part methanol to one-part ethanol was used as a pressure transmitting medium. The wavelength used for radiation was 0.619921 Å. The data was acquired by $2-D$ detection plate and then integrated as a calibration standard in the software [FIT2D] using LaB_6 [94]. The obtained XRD patterns were fitted using the Le Bail algorithm as implemented in the Jana2006 software package for unit cell

parameters [95, 96].

3.3 Neutron Powder Diffraction (NPD)

According to wave-particle dualism, neutrons have both wave and particle like characteristic. Due to the wave characteristic, the wavelengths for neutrons are given as:

$$\lambda = \frac{h}{mv} \tag{3.2}$$

where h is Planck constant. m and v are the mass and velocity of neutron.
At temperature T, the wavelength of neutron is given as:

$$\lambda = \frac{h}{\sqrt{3mKT}} \tag{3.3}$$

where K is the Boltzmann constant and T is the temperature of the sample.
Similar to x-rays neutrons have a wavelength of atomic scale order Å. Unlike x-rays, neutrons do not have a charge. So that, they can easily penetrate into the electron cloud of atoms or ions and easily be scattered by the nucleus. Neutrons can generate interference and thus leads to the Bragg diffraction patterns. Because of the smaller magnetic moment ($\approx 10^{-3}\mu_B$) of neutrons, the scattering atom or ion will interact with the neutron beam. So that neutron can probe both crystal and magnetic structure of materials. Fig. 3.3 shows the schematic diagram of the neutron diffraction experiment at a reactor source. A steady flux of incident neutrons of several wavelengths is produced by the moderator. Then, a monochromator is used to produce a single wavelength neutron beam. The scattering vector Q for neutron scattered by a sample is given as $Q = K_0 - K_1$ which is directly proportional to the angle θ between sample and detector and inversely proportional to the wavelength. To investigate both crystal and magnetic structure as well as antisite disorder, NPD was done on $\approx$ 6 gm powder sample at D2B beamline (ILL, Grenoble). D2B is designed to achieve high resolution but limited by powder particle size. It has a white monochromatic neutron beam in a wide wavelength range by using a Ge monochromator and gives a diffraction pattern in steps of 0.05° in 2θ range of 10-160°. For the

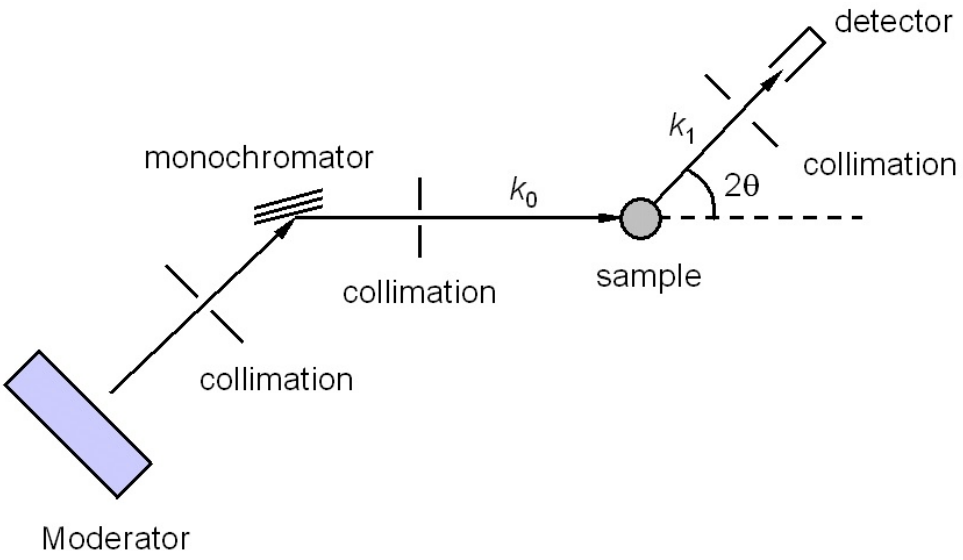

Figure 3.3: *Schematic diagram of neutron diffraction experiment with neutrons of incident wave vector K_0 and scattered wave vector K_1. Taken from Ref. [27].*

present work, NPD measurements were performed using Ge[335], by using a wavelength of 1.59 Å in the high intensity mode. A cryostat, cryofurnace and high temperature furnace attached with the beamline were used for temperature dependent measurement. The analysis of neutron diffraction was done by using FullProf software [57].

3.4 Scanning Electron Microscopy

The compositional analysis was done by energy dispersive analysis of X- rays (EDAX) from scanning electron microscope (SEM) of Philips XL30 equipped with a LaB_6 cathode and a XFLASH detector at 15 kV. This technique can do precise measurement of the sample size down to nm range. Prior to the measurement, samples were polished on resin. When a focused beam of high energy electrons interacts with the sample surface. A variety of signals is generated which reveal information about the morphology and chemical composition [38].

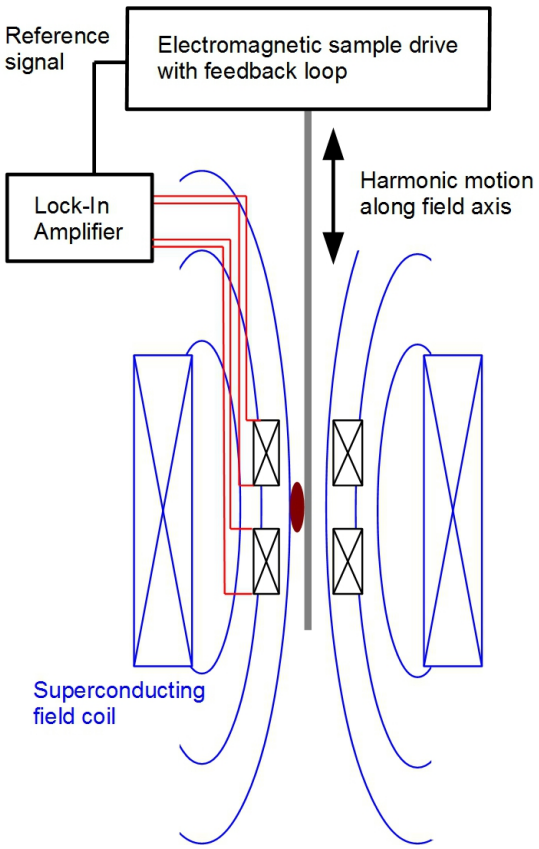

Figure 3.4: *Sketch of a vibrating sample magnetometer (VSM).*

3.5 Magnetic Measurements

A vibrating sample magnetometer (VSM) was used for magnetization measurement. The magnetization measurements of bulk samples were done on a needle like sample, mounted into the sample holder having a mass between 10 to 20 mg. The needle like sample was produced from mechanical crushing. Ac susceptibility, temperature dependent and field dependent magnetization measurements were done for the magnetic characterization. This technique is based on Faraday's law of induction. The sample is mechanically oscillating inside an inductive pick-up-coil system. Typically, a motor or piezoelectric actuator produces the vibration. The flux change caused by vibrating the sample induces a voltage in the pickup coils, which is proportional to the magnetic moment of the sample. A schematic drawing of a typical VSM is shown in Fig. 3.4. In this

technique,the sample is mounted on a quartz holder Fig. 3.4. The VSM used here is capable of measuring magnetization value in the range of 2.5×10^{-5} to 5 emu in the temperature range from 2 to 400 K with a magnetic field change of $-$ 7 T to 7 T [97].

3.5.1 Pressure Dependent Magnetization

Hydrostatic pressure dependent magnetization measurement was done in a home-made Cu-Be piston cylinder type pressure cell, which was built to fit the sample space inside the MPMS XL magnetometer. The shape, size and design of the pressure cell was similar to the that used in the reported reference [98]. For the pressure transmitting medium silicon oil was used. A small piece of Sn as a reference sample was loaded along the measuring sample. The superconducting transition of Sn, which occurs around 3.7 K at 1 bar, was used to determine the pressure inside the cell. In this thesis the pressure reported for the magnetic measurement was corrected for the pressure drop that occurs on cooling from RT to 3.7 K. The estimation of pressure drop from a separate calibration measurement to be $\approx$ 2 kbar was obtained by measuring T_{C} of high purity MnAs for which the pressure dependence is already reported [96].

3.6 Magnetocaloric Measurements

The MCE can be quantified in two terms: isothermal entropy change ΔS_{M} and adiabatic temperature change ΔT_{ad}. The isothermal entropy change ΔS_{M} can be determined from the magnetization (isothermal and isofield) measurements by using Maxwell relation. The specific heat capacity C_{P} and the magnetization measurements give adiabatic temperature change ΔT_{ad}. In addition to that, one can calculate ΔT_{ad} directly in pulsed magnetic field [28]. A detailed description about ΔS_{M} and ΔT_{ad} has been discussed in this section.

3.6.1 Isothermal Entropy Change

The MCE can be determined from magnetization curves using Maxwell equation from $M(H)$ or $M(T)$ curves.

$$\Delta S_M = S(T,H) - S(T,0) = \int_0^H \left(\frac{\partial M}{\partial T}\right)_H dH. \tag{3.4}$$

The calculated value of ΔS_{M} strongly depends upon the measurement protocol. The estimated value of ΔS_{M} from $M(H)$ is not recommendable for large hysteresis MSM Heusler compounds because of the coexistence of the high and low temperature phase which can lead to critical overestimation of the MCE even though the measurement was done by using discontinuous protocol (before each measurement, sample was heated to high temperature and then cooling down to low temperature). On the otherhand, from $M(T)$ measurements in a broad temperature interval ΔS_{M} value is much reasonable because the phase coexistence problem has been avoided. A more accurate way to calculate ΔS_{M} from the heat capacity data in different magnetic fields using equation 2.34. Obviously, a small error will always be inevitable, as it is impossible to measure the heat capacity down to 0 K due to the third law of thermodynamics.

3.6.2 Adiabatic Temperature Change

The adiabatic temperature change ΔT_{ad} reported in this thesis was measured in pulsed magnetic field in the Helmholtz-Zentrum Dresden Rossendorf (HZDR) at the Dresden High Magnetic Field Laboratory (Hochfeld-Magnetlabor Dresden, HLD). The pulsed magnets at HLD were energized from maximum electric power of 5 GW. All the magnets in HLD were separated from each other through installed individual pulsed cell. The magnet was cooled down to 77 K by immersing them in pulsed magnets to reduce the ohmic resistance. For the direct measurement of MCE, there are three essential components: the magnet for supplying the magnetic field, a cryostat to cool down or heat up the sample and a thermometer to measure the temperature of sample. The thermocouple used here was copper-constantan. The MCE was done on two flat pieces of the sample which were cutted from diamond saw. Fig. 3.5 shows the schematic diagram

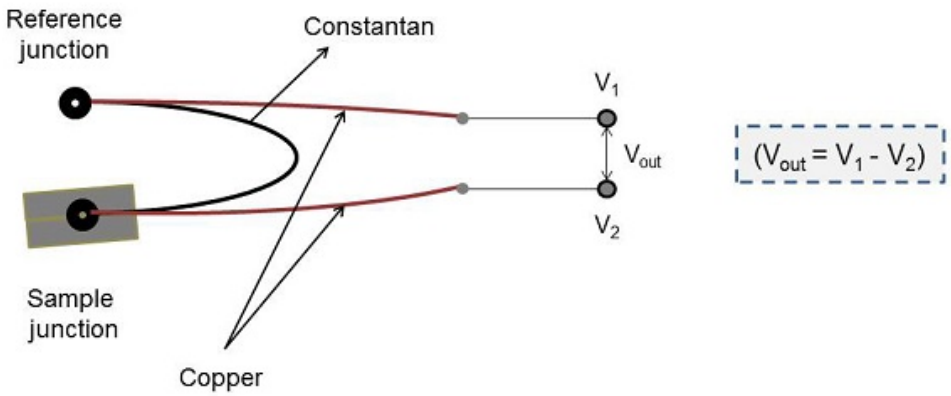

Figure 3.5: *Schematic diagram of the copper-constantan thermocouple glued with the sample. Taken from Ref. [99].*

of sample attached with thermocouple. One end of thermocouple was sandwiched by gluing with a small amount of silver epoxy between the two equally flat pieces of the sample. The other end was used to measure the temperature inside the sample holder and to detect a possible influence of the magnetic field on thermocouple voltage. Fig. 3.6(a) shows the experimental set-up for MCE measurement in a pulsed magnetic field, which contains cryostat, magnet, and electronic connections and Fig. 3.6(b) shows both sides of the sample holder together with brass cylinder [99, 100].

The advantage of MCE measurement in pulsed magnetic field is the availability of high magnetic fields, which induce the transition also far below the martensitic transition and saturation of magnetization $M(H)$. The short pulse length ≈ 50 ms allows the adiabatic measurement conditions. Additionally, it provides realistic condition for magnetic refrigeration applications. The disadvantages are also like noisy environment and finite response time of the thermocouple. The challenge in this measurement is to make good thermocouple. Because when the thermocouple wires were twisted through each other, the small loops in the thermocouple wiring produced a very large spurious voltage (dB/dt) which affects the component of the MCE [99].

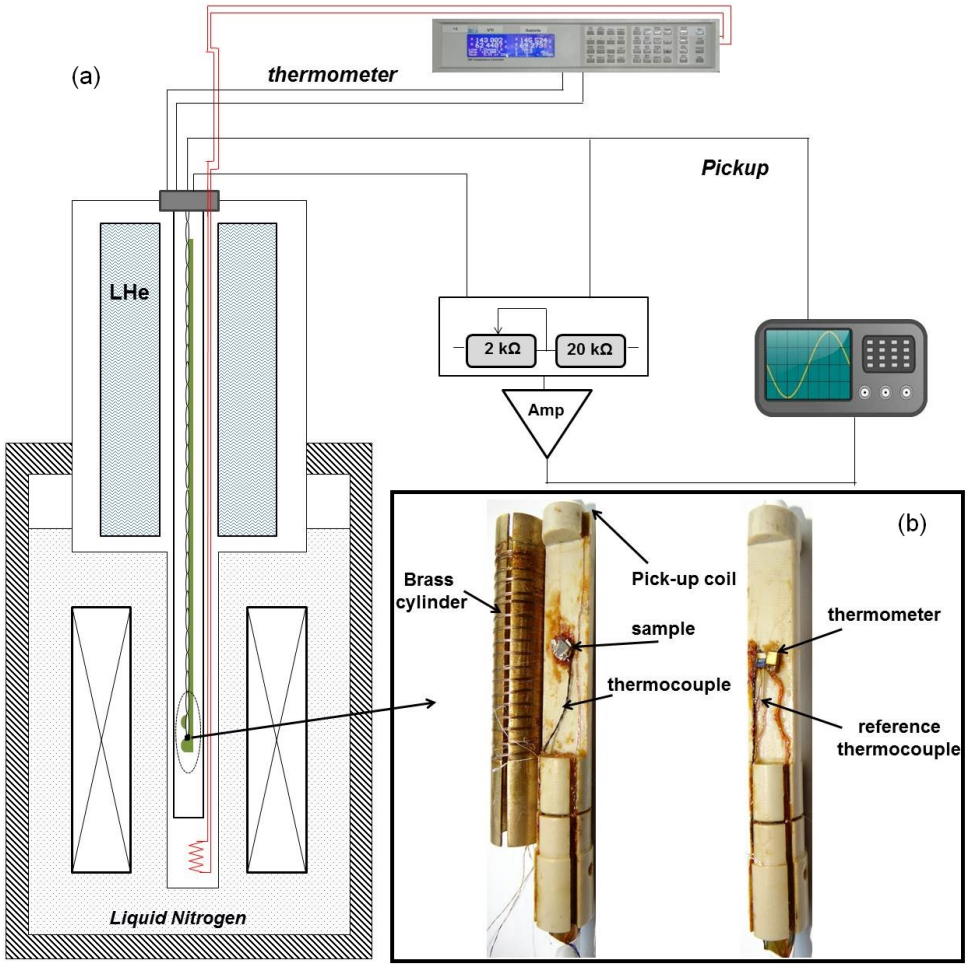

Figure 3.6: *(a) Schematic diagram of the experimental set-up for MCE measurement in pulsed magnetic field. (b) Both sides of sample holder together with brass cylinder, which is represented in black rectangle box. Taken from Ref. [99].*

3.7 Magnetostriction Measurement

The magnetostriction measurements were performed by using an optical-fiber strain gauge in pulsed magnetic field up to 20 T with a rise time of about 7 ms and a total pulse duration of 25 ms. The strain gauge is bonded to the sample surface with cyanoacrylate epoxy. The strain gauge fiber Bragg grating (FBG) length is 1 or 2 mm with a peak reflectivity at 1550 nm. The transmission from the sample strain to the fiber is in the range of $70 - 90\%$. The sample elongation

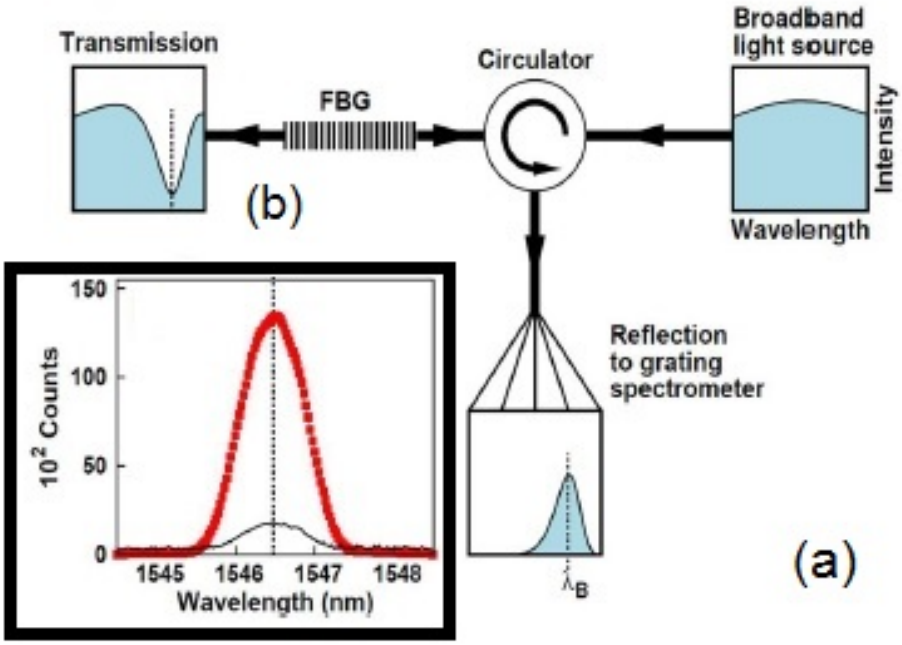

Figure 3.7: *Schematic drawing of the magnetostriction set-up. (a) Optical circuit for fiber Bragg grating (FBG) measurements. Each box represents the light spectra. (b) Reflection spectrum of the FBG at 5.4 K in zero field (red curve). The black curve is the root mean square noise (gain by 100). It is represented in black rectangle box. Adapted from [101].*

was registered by a high-resolution grating spectrometer and converted to a reflectivity-peak shift. The spectrometer operates at a frequency of 47 kHz and provides a resolution of better than 10^{-6} in elongation. The optical circuit and corresponding reflection spectrum for 2 mm FBG is illustrated in Fig. 3.7(a) and (b). A detailed description of this technique is given in [101].

4 Modulation in $Ni_{2+x}Mn_{1-x}Z$ (Z= In, Ga) Heusler compounds

In this chapter, an overview of modulated structures, explained by soft phonon and adaptive phase model has been given [103, 104, 105]. The modulated structure was studied in two different MSM Heusler compounds (a) $Ni_2Mn_{1.4}In_{0.6}$ and (b) $Ni_{1.9}Pt_{0.1}MnGa$ from SXRPD and NPD experiments. The structure modulation in $Ni_2Mn_{1.4}In_{0.6}$ and $Ni_{1.9}Pt_{0.1}MnGa$ could be successfully explained using adaptive phase and soft phonon models, respectively. These successfull studies give an opportunity to critically examine the two proposed mechanism for the origin of modulation in MSM Heusler compounds. In the adaptive phase model, the modulated structure is considered as a nanotwinned state of Bain distorted phase. Uniform atomic displacement and commensurate modulation are the key characteristic of adaptive phase model. Whereas, in soft phonon model, the modulated structure occurs from phonon softening which results in non-uniform atomic displacement and incommensurate structure.

4.1 Overview of the Modulated Structure

Lattice periodicity is a fundamental concept to define the crystallography. The periodic deformation of basic structure having space group symmetry is considered as modulation. If the periodicity of modulation is the same as that of basic structure, the modulated crystal structure is called commensurate and if it does not belong to the basic structure, then the modulated crystal structure is called incommensurate [110].

The modulated structures occur in various kinds of materials like magnetic shape memory compounds and ferroelectrics. The magnetic and electric field can distort unit cell lattices, which results in associated strain below 0.3%. These applied fields control the orientation of low symmetry unit cells. The modulated structure occurs because of the diffusionless martensitic transformation from high temperature, high symmetry austenite phase to low temperature, low symmetry martensite phase. The martensite phase is accommodated from a habit plane as a lattice invariant interface. This lattice invariant interface fixes the geometrical relationship between the high temperature austenite and low temperature martensite phases. The lattice mismatch between two phases is compensated by the twinning of martensite. Different aligned martensite variants are connected by a large number of twin boundaries. Initially, these modulated structures were considered as thermodynamically stable phases. In 1991, Khachaturyan *et al.* [93] argued that the modulated structures occuring in materials should be understood as ultrafinely twinned metastable structures.

It is important to mention that in the literature the modulated structure is mainly reported by $3M$, $5M$ and $7M$ type notations. However, in Heusler compounds, the periodicity is completed after even number of layers. So, the correct notations for Heusler compounds are $6M$, $10M$ and $14M$. The periodicity will be complete after odd number of layers, if the ordering of the austenite phase is B2 type. The concept to use $3M$, $5M$ and $7M$ notations for Heusler compounds having $L2_1$ type ordered structure in austenite phase is on the basis of the number of satellite spots between the neighboring austenite peaks [34].

4.2 Origin and Nature of Modulation in $Ni_2Mn_{1.4}In_{0.6}$

Recently, the origin of modulation in Ni_2MnGa MSM Heusler compound was studied in the framework of the soft phonon model because of the non uniform atomic displacements. The incommensurate martensite phase in Ni_2MnGa results from an incommensurate premartensite phase and not directly from the austenite phase. The diffraction pattern of Ni_2MnGa shows the presence of phasons and broadening of superlattice peaks due to the phason strains which

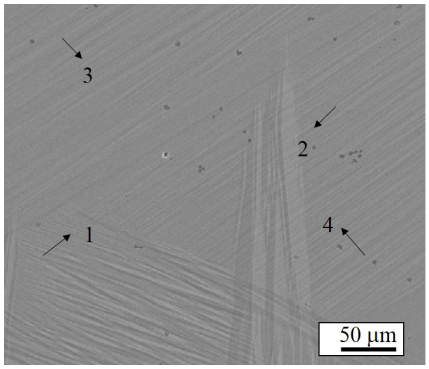

Figure 4.1: *RT SEM image of $Ni_2Mn_{1.4}In_{0.6}$. The black arrows indicate the areas where the composition was analyzed in detail.*

make it against the concept of adaptivity. On the otherhand, Ni-Mn-In MSM Heusler compounds do not show the premartensite phase as the martensite phase directly transforms from the austenite phase. This suggests that it will be interesting to investigate the structural modulation in $Ni_2Mn_{1.4}In_{0.6}$ MSM Heusler compound and it may follow the adaptive phase model.
A polycrystalline ingot with nominal composition of $Ni_2Mn_{1.4}In_{0.6}$ from its constituent elements of 99.99% under Ar atmosphere was prepared by arc melting technique. The ingot was annealed at 973 K in sealed quartz ampules for three days for homogenization and then quenched in ice water mixture.

4.2.1 Scanning Electron Microscopy

First step of phase analysis was done by SEM under backscattered electron detection (BSD) configuration which revealed that the sample is single phase with a homogeneous composition distribution. SEM image has some black dots which represents the unreacted Mn. The composition analysis was done by EDAX. Prior to phase analysis sample was embedded in epoxy resin blocks and a smooth surface was prepared.

4.2.2 Magnetization Measurement

To see the characterization temperatures T_M and T_C, the magnetization was done at low magnetic field (500 Oe) during zero field cooling (ZFC), field cooled

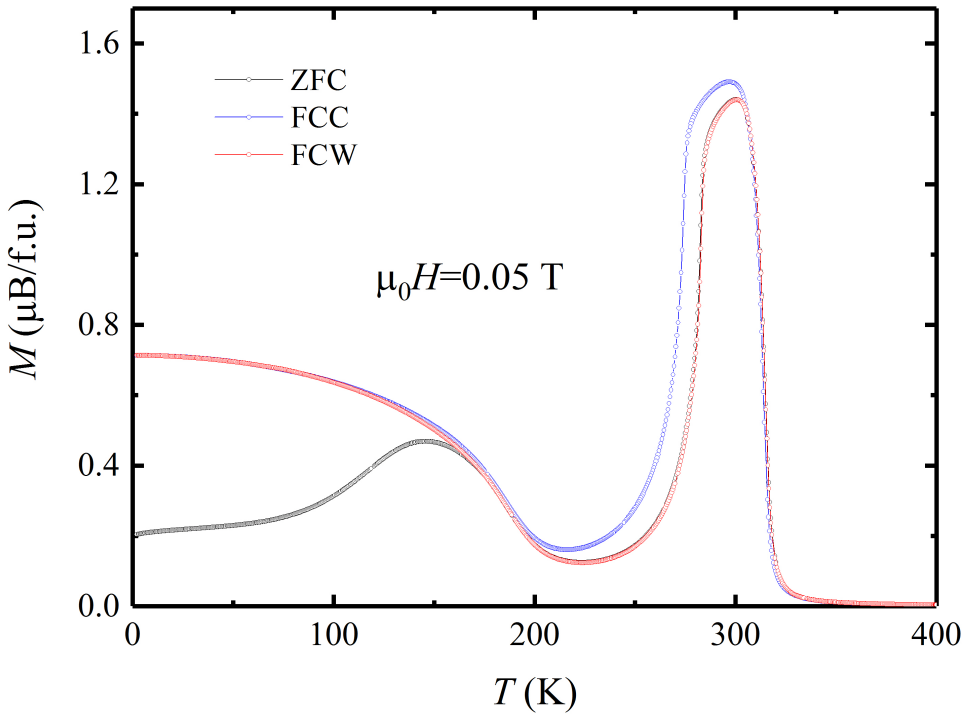

Figure 4.2: *Magnetization (ZFC, FCC and FCW) $M(T)$ of $Ni_2Mn_{1.4}In_{0.6}$ as a function of temperature at low magnetic field of 500 Oe.*

cooling (FCC) and field cooled warming (FCW) in the temperature range from 2 to 400 K. On cooling, a transition from paramagnetic to ferromagnetic has been observed around 315 K, which is followed by the decrease in magnetization around 295 K. The existence of thermal hysteresis confirms the first-order nature of the martensitic transition which is in well agreement with the literature [12, 55]. In the martensite phase around $T \approx 145$ K, the bifurcation of the ZFC and FCC curve arises because of the coexistence of antiferromagnetic (AFM) and ferromagnetic (FM) exchange interactions.

The isothermal magnetization $M(H)$ plot at 2 K indicates a typical AFM ground state as shown in Fig. 4.3. Inset in Fig. 4.3 shows the AFM ground state with spin-flop transition which occurs at low magnetic field of ± 0.05 T leading to the opening up of a double hysteresis loop above this field. The occurrence of such spin flop transition at low magnetic field suggests that both the FM and AFM states are nearly degenerate in the martensite phase. Although, the ground state is dominated by AFM interactions.

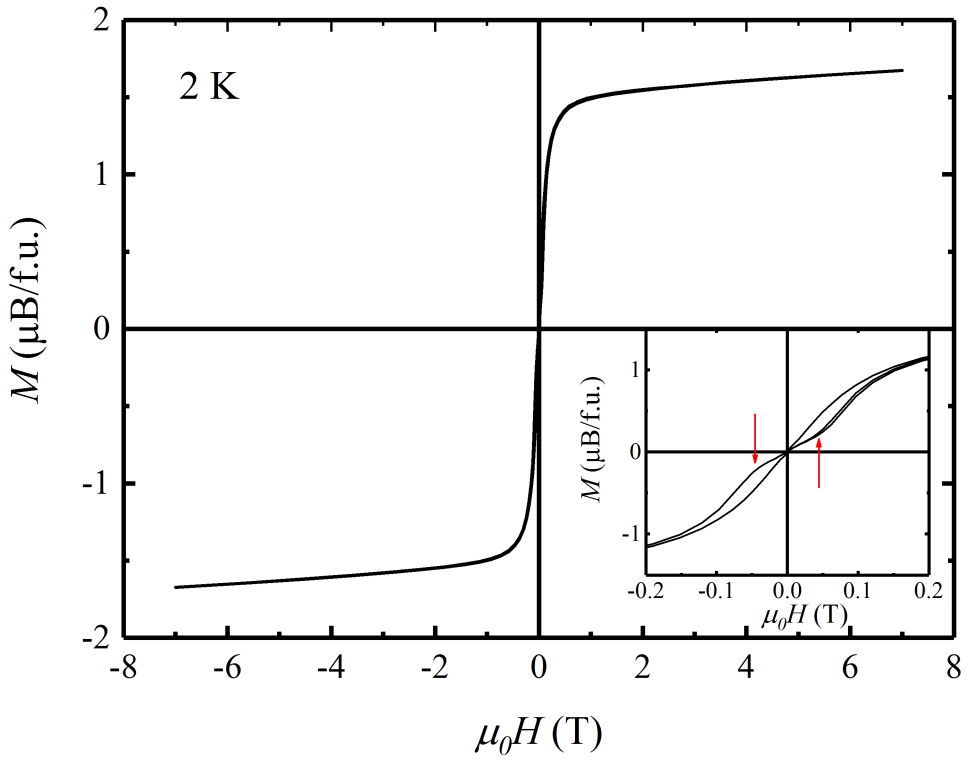

Figure 4.3: *$M(H)$ measurement of $Ni_2Mn_{1.4}In_{0.6}$ at 2 K Inset shows the $M(H)$ curve on an expanded scale, where the spin-flop transitions are marked by red arrows.*

4.2.3 High Resolution Synchrotron XRD

To resolve the structure of $Ni_2Mn_{1.4}In_{0.6}$, the SXRPD patterns were recorded in both austenite (350 K) and martensite (235 K) phases, respectively. The first step of structural analysis was done by indexing the powder diffraction pattern using Le Bail technique, which refines the unit cell parameters and profile broadening functions to obtain the best fit between the observed and calculated profiles in the least-squares sense for a given space group. In the austenite phase, all the observed Bragg peaks could be refined with the cubic structure (space group Fm-$3m$) shown in Fig. 4.4(a). The refined cell parameter is found to be 6.0048(4) Å. Inset in Fig. 4.4(a) shows the presence of superstructure

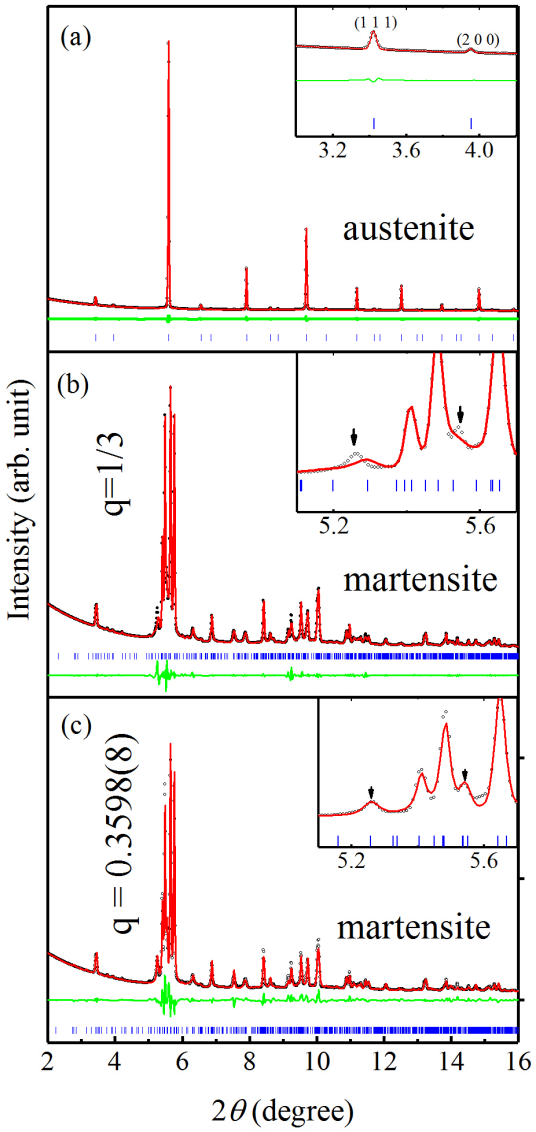

Figure 4.4: *Le Bail fits of SXRPD patterns for $Ni_2Mn_{1.4}In_{0.6}$ at (a) cubic austenite phase (350 K). Inset shows the fitting for main peaks (111) and (200) on expanded scale, related to $L2_1$ ordering. (b) Martensite phase at 235 K with commensurate structure model, and (c) Martensite phase at 235 K using incommensurate structure model. The inset in (b) and (c) shows the fitting for the main peak region (2θ = 5-6°) on an expanded scale. Arrows in (b) and (c) represent the satellite reflections. The experimental data, fitted curve, and the residues are shown by black circles, red continuous lines and green continuous line(bottom most). The blue tick marks represent the Bragg peak positions.*

peaks like (111) and (200) in the SXRPD pattern which confirms the structure corresponding to the ordered $L2_1$ type. At 235 K, more number of Bragg reflections appear indicating that the structure is no longer cubic. A careful analysis of all the observed high and low intensity peaks revealed that the structure can not be refined in terms of a simple Bain distorted unit cell and it requires the consideration of Bain distorted modulated unit cell as reported in other MSM Heusler compounds. To investigate the modulated structure, superspace $(3+1)-D$ formalism is used in the martensite phase of $Ni_2Mn_{1.4}In_{0.6}$ MSM Heusler compound. Following this formalism, the SXRPD pattern was divided into two sets of reflections: (1) main reflections due to the Bain distorted basic structure and (2) satellite reflections corresponding to the modulated structure whose intensity is in general much less than the intensity of main reflections. All the main reflections corresponding to the basic structure were indexed by using monoclinic cell (space group $I2/m$) and the lattice parameters are $a = 4.3983(1)$ Å, $b = 5.6453(2)$ Å, $c = 4.3379(1)$ Å and $\beta = 92.572(2)^\circ$. After obtaining the cell parameters for the basic structure, the superspace group formalism was used to refined the full SXRPD pattern including both the main and satellite reflections. The satellite reflections were indexed using a modulation wave vector $\mathbf{q} = (0, 0, \frac{1}{3})$ and superspace group $I2/m(\alpha 0 \gamma)00$. The inset of Fig. 4.4(b) shows the commensurate wave vector which could index many of the satellite reflections, but some of the calculated satellite reflections were found to be shifted away from the observed reflection positions. So, the wave vector $\mathbf{q}$ was refined and an excellent match has been found between the observed and calculated profiles for an incommensurate modulation wave vector $\mathbf{q} = 0.3599(8)c^* = (\frac{1}{3} + \delta)c^*$ (where $\delta = 0.02653$ is the degree of incommensuration). It include all Bragg and satellite reflections which could not be accounted for using the commensurate wave vector $\mathbf{q} = \frac{1}{3}$ as shown in Fig. 4.4(c).

This indicates that $Ni_2Mn_{1.4}In_{0.6}$ has an incommensurate $3M$-like modulation. The second- order satellite peaks are indicated by black arrows in SXRPD pattern. A slightly different composition of Ni-Mn-In shape memory compound with higher martensite transition temperature also show the similar $3M$ modulated martensite structure [105]. Le Bail refinement sucecessfully refines the

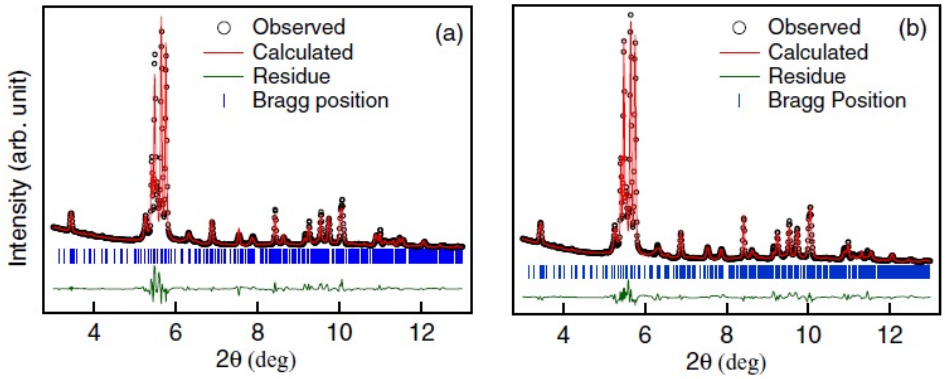

Figure 4.5: *Rietveld fits of SXRPD patterns for $Ni_2Mn_{1.4}In_{0.6}$ in martensite phase (235 K) by considering the (a) soft phonon (non-uniform atomic displacement) structural model (b) Adaptive phase (uniform atomic displacement) structural model. The experimental data, fitted curve, and the residue are shown by black circles, red continuous line and green continuous line (bottom most) respectively. Blue tick marks represent the Bragg peak positions.*

peak broadening of both the main and satellite reflections which was modeled using anisotropic strains as per Stephen's model without invoking 4^{th}- rank strain tensor for phason broadening. It is opposite to the situation in Ni_2MnGa in which phason strains had to be invoked to model the broadening of the satellite peaks.

In the next step, Rietveld refinement was done to study the atomic positions and atomic modulation functions. The Wyckoff positions for Ni, Mn and In were considered to be $4h$ (0.5, 0.25, 0), $2a$ (0, 0, 0), and $2d$ (0, 0.5, 0) sites, respectively, of the basic structure in Rietveld refinement. The excess Mn atoms occupy the $2d$ wyckoff positions instead of In atoms. The amplitudes of the atomic modulation function were refined without applying any constraints for different atomic sites in accordance with the non-uniform displacement model used in the refinement of Ni_2MnGa system [132, 133]. This refinement gives a reasonable fit between the observed and calculated peak profiles as shown in Fig. 4.5(a). But, the interatomic distances are found to be physically unrealistic for Ni-Mn-In family of intermetallic compounds.

Fig. 4.6(a) shows the interatomic distance obtained after Rietveld refinement.

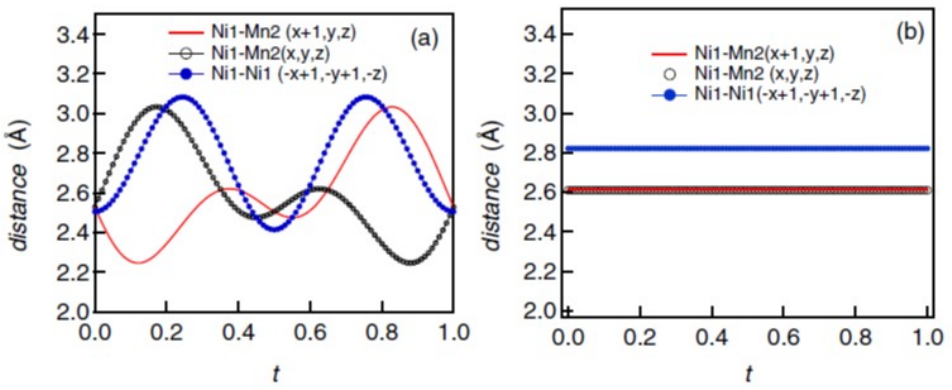

Figure 4.6: *Selected distance d as a function of t parameters for $Ni_2Mn_{1.4}In_{0.6}$ derived from (a) Soft phonon (non uniform atomic displacement) structural model showing unphysical values (less than 2.5 Å) and (b) Adaptive phase (uniform atomic displacement) model showing values which are expected for these kind of intermetallic compounds.*

These values are less than 2.3 Å for some t values, whereas the sum of atomic radii (1.25 Å for Ni, 1.37 Å for Mn, and 1.67 Å for In) of various pairs of atoms is always $\geq$ 2.5 Å. Rietveld refinement was also carried out for the nonuniform displacement model by using constraints on the interatomic distances in order to get the physically plausible values. But it converged to the values obtained for the uniform displacement model. The reason for physically unrealistic interatomic distance could be either the presence of antisite disorder observed in Ni-Mn based Heusler compounds or the nonexistence of the nonuniform model [134, 135, 136]. The refined parameters corresponding to the non-uniform displacement models are shown in table 4.1.

In the next step, uniform displacement model was considered for Rietveld refinement in which the modulation amplitude of all atomic sites were constrained to be identical. Rietveld refinement result of uniform displacement model is shown in Fig. 4.5(b). The corresponding atomic positions are listed in table 4.2.

4.2.4 Neutron Powder Diffraction

After getting the analysis from SXRPD of correct atomic modulation model, NPD was collected to discuss the magnetic structure in the austenite and

Table 4.1: *Atomic positions (x, y, z), amplitudes (A_1, A_2, B_1, B_2) of the modulation function, and atomic displacement parameter (U_{iso}) of the modulated martensite phase (235 K) of $Ni_2Mn_{1.4}In_{0.6}$ obtained from the Rietveld refinements of SXRPD data considering non-uniform displacement model.*

Atom	Wyckoff position	Modulation amplitude	x	y	z	U_{iso} (Å^2)
Ni1	4*h*		0.5	0.25	0	-0.004(1)
		A_1	0.117(2)	0	0	
		B_1	0	0	0	
		A_2	0.034(4)	0	0	
		B_2	0	0.028(2)	0	
Mn1	2*a*		0	0	0	-0.009(2)
		A_1	0.114(3)	0	0	
		B_1	0	0	0	
		A_2	0.034(8)	0	0	
		B_2	0	0	0	
In1	2*d*		0	0.5	0	0.045(3)
Mn2	2*d*		0	0.5	0	0.045(3)
		A_1	0.051(4)	0	-0.015(6)	
		B_1	0	0	0	
		A_2	-0.021(5)	0	0	
		B_2	0	0	0	

martensite phase. Since, both Ni and Mn atoms have similar x-ray atomic scattering factors, XRD can not distinguish antisite disorder. In contrast to that, the scattering length of neutrons for Ni and Mn have opposite signs and hence neutron scattering is ideally suited to capture Ni and Mn antisite disorder. The nuclear superspace group $I2/m(\alpha 0\gamma)00$ has four magnetic superspace groups due to time reversal symmetry breaking: (i) $I2/m(\alpha 0\gamma)00$, (ii) $I2'/m(\alpha 0\gamma)00$, (iii) $I2/m'(\alpha 0\gamma)00$, and (iv) $I2'/m'(\alpha 0\gamma)00$. Among the four superspace groups, only (i) and (iv) magnetic superspace group allow nonzero magnetic moments and restrict magnetic moments along the b axis of the monoclinic unit cell.
Rietveld refinement was done to resolve the NPD pattern of $Ni_2Mn_{1.4}In_{0.6}$ in both austenite and martensite phase. In the austenite phase at 300 K, the refinement was done by considering the atomic positions within the space group Fm-3m. Here, Ni and Mn atoms occupy 8*c* (0.25, 0.25, 0.25) and 4*a* (0, 0,

Table 4.2: *Atomic positions (x, y, z), amplitudes (A_1, A_2, B_1, B_2) of the modulation function, and atomic displacement parameter (U_{iso}) of the modulated martensite phase (235 K) of $Ni_2Mn_{1.4}In_{0.6}$ obtained from the Rietveld refinements of SXRPD data considering adaptive phase model.*

Atom position	Wyckoff amplitude	Modulation	x	y	z	U_{iso} (Å^2)
Ni1	4h		0.5	0.25	0	0.0084(5)
Mn1	2a		0	0	0	0.0084(5)
In1	2d		0	0.5	0	0.0084(5)
Mn2	2d		0	0.5	0	0.0084(5)
		A_1	0.1015(7)	0	0.0018(8)	
		B_1	0	0	0	
		A_2	0.0259(14)	0	0.0034(19)	
		B_2	0	0	0	

0) Wyckoff positions respectively, while extra Mn and In occupy 4b (0.5, 0.5, 0.5) Wyckoff positions according to their relative occupancies. The possibilities of anti-site disorder was also considered between different atomic sites (for e.g. Ni(8(c)-Mn(4a), Mn(4a)-In(4b) and Ni(8c)-In(4b)) but could not observe any improvement in the fits of R factors. Therefore, Rietveld analysis of NPD data at 300 K confirms the absence of any substantial anti-site disorder in $Ni_2Mn_{1.4}In_{0.6}$ MSM Heusler compound as shown in Fig. 4.7.

After confirming the absence of any descernible anti-site disorder from the analysis of NPD at 300 K, the refinement was done in martensite phase at 3 K. The magnetic structure can be described by $I2/m(\alpha 0\gamma)00$ magnetic superspace group for Rietveld refinement in which the magnitude of the Mn magnetic moments are equal (1.18 μ_{B}) of fully occupied site (2a) and partially occupied site (2d) are equal but antiferromagnetically correlated. The NPD of modulated structure in martensite phase was refined with $(3+1)-D$ superspace formalism, similar to the analysis of the SXRPD pattern. Rietveld refinement of NPD was done by considering both non-uniform and uniform displacement model. In the first step, Rietveld refinement was carried without applying any constraints on the amplitude or direction of atomic displacements for the atomic modula-

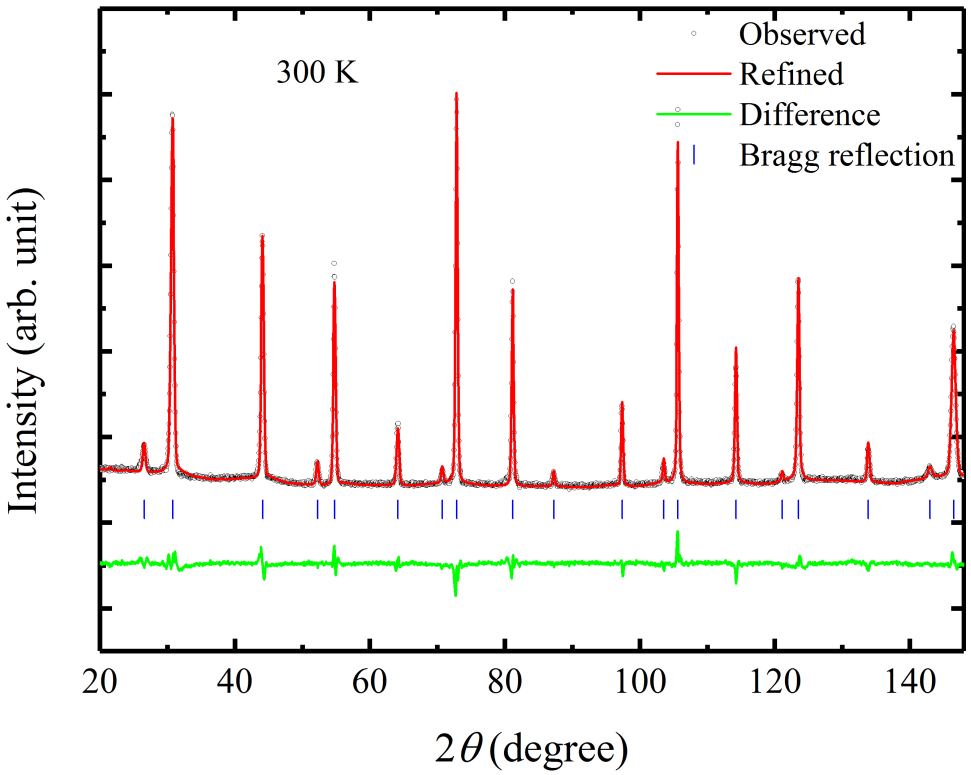

Figure 4.7: *Rietveld refinement of NPD pattern of $Ni_2Mn_{1.4}In_{0.6}$ in the austenite phase at 300 K.*

tion functions of the different atoms. The refinement pattern is shown in Fig. 4.8 and 4.9. The refined parameters corresponding to non-uniform and uniform displacement models are given in table 4.3 and 4.4, respectively.

Interestingly, Rietveld refinement converges for a non-uniform atomic displacement model but interatomic distances are unreasonable, as shown in Fig. 4.10(a) for some selected atomic pairs obtained using NPD. The interatomic distances obtained from NPD can not resolve the issue of implausible interatomic distance using non-uniform displacement model, similar to SXRPD analysis. It indicates that the problem lies within the modulation model itself. In the next step, uniform displacement model was considered for Rietveld refinement in which the amplitude of modulation for all the atomic sites was constrained to be identical as shown in table 4.4. The interatomic distances derive from the uniform atomic displacement model clearly reveal that this model gives physically realistic interatomic distances as shown in Fig 4.10(b) which is acceptable for MSM Heusler

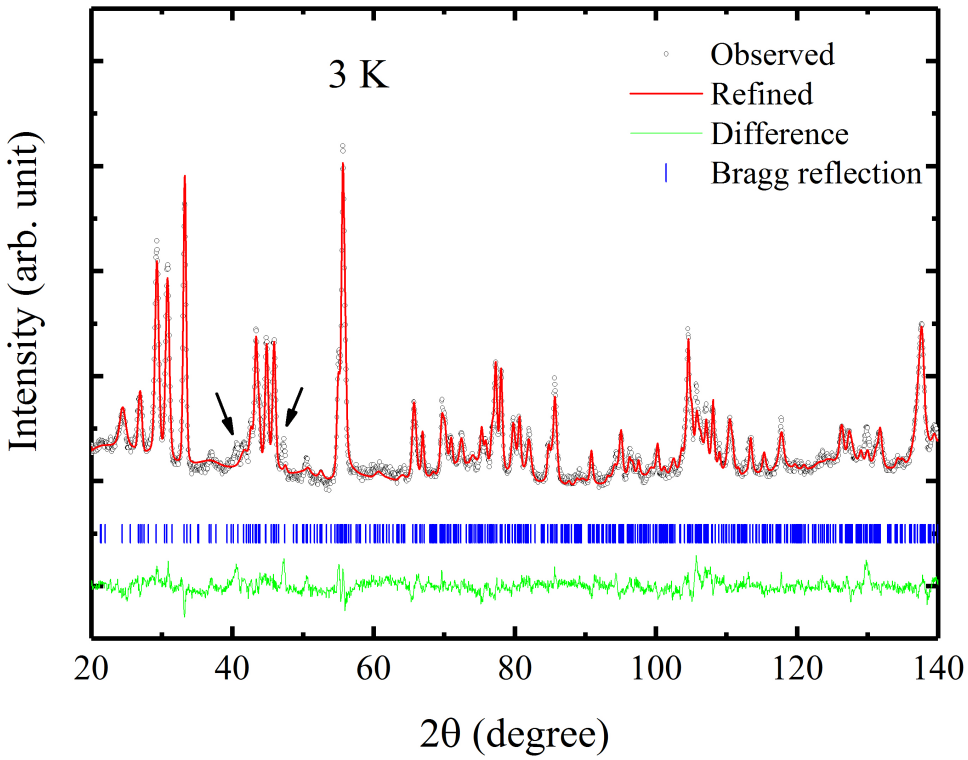

Figure 4.8: *Rietveld refinement of NPD pattern of $Ni_2Mn_{1.4}In_{0.6}$ in the martensite phase at 3 K using non-uniform displacement model. Black arrows indicate peaks due to the cryo-furnace wall material (Al).*

compounds. Thus, Rietveld refinement of SXRPD and NPD patterns confirms that $Ni_2Mn_{1.4}In_{0.6}$ involves uniform displacement of atoms in the martensite phase and follow the adaptive phase model. The analysis of diffraction data from $(3+1)-D$ superspace group is used to obtain the $3-D$ superstructure. Table 4.5 shows the refined structural parameters for $3-D$ rational approximant superstructures, which are obtained from the $(3+1)-D$ superspace group analysis of NPD pattern at 3 K by using non-uniform displacement (electronic instability) model, while table 4.6 shows the refined structural parameters for uniform displacement (adaptive phase) model.

4.2.5 High Resolution Transmission Electron Microscopy

To further support the uniform displacement model, the origin of modulation in $Ni_2Mn_{1.4}In_{0.6}$ was studied from HRTEM measurements. Fig. 4.11 shows the

Table 4.3: *Atomic positions (x, y, z), amplitudes (A_1, A_2, B_1, B_2) of the modulation function, and atomic displacement parameter (U_{iso}) of the modulated martensite phase (235 K) of $Ni_2Mn_{1.4}In_{0.6}$ obtained from the Rietveld refinements of NPD data using non-uniform displacement model.*

Atom	Wyckoff position	Modulation amplitude	x	y	z	U_{iso} (Å2)
Ni1	4*h*		0.5	0.25	0	-0.007(6)
		A_1	0.128(7)	0	0	
		B_1	0	0.011(2)	0	
		A_2	0.022(13)	0	-0.011(1)	
		B_2	0	-0.022(1)	0	
Mn1	2*a*		0	0	0	-0.007(6)
		A_1	0.103(6)	0	-0.030(5)	
		B_1	0	0	0	
		A_2	0.095(5)	0	0	
		B_2	0	0	0	
In1	2*d*		0	0.5	0	-0.007(6)
Mn2	2*d*		0	0.5	0	-0.007(6)
		A_1	0.14(2)	0	-0.07(3)	
		B_1	0	0	0	
		A_2	0.15(2)	0	-0.07(2)	
		B_2	0	0	0	

electron diffraction pattern at 300 K which confirms the austenite structure of $Ni_2Mn_{1.4}In_{0.6}$ as supported from the magnetization data.

Fig. 4.12(a) shows the noise filtered HRTEM image along the [210] zone axis, which was observed by *insitu cooling* of the sample down to 100 K. For this crystal lattice projection, atoms appear as bright spots. The interplanar spacing of 2.1 Å is observed along the (001) atomic planes. An occurrence of bright and dark horizontal bands is related to the different stacking of the (001) planes, generating the unit cell of $3M$ structure. A stacking of six atomic planes (c = 6 × 2.15 Å = 12.98 Å) in the martensite phase is shown in Fig. 4.12(b). The corresponding atomic positions for the rational approximant structure of the martensite phase and correlate to the uniform displacement model is shown in table 4.6. For this projection, the twinning of the (001) planes is represented by a dark zig-zag line within the $3M$ unit cell. This stacking sequence is represented

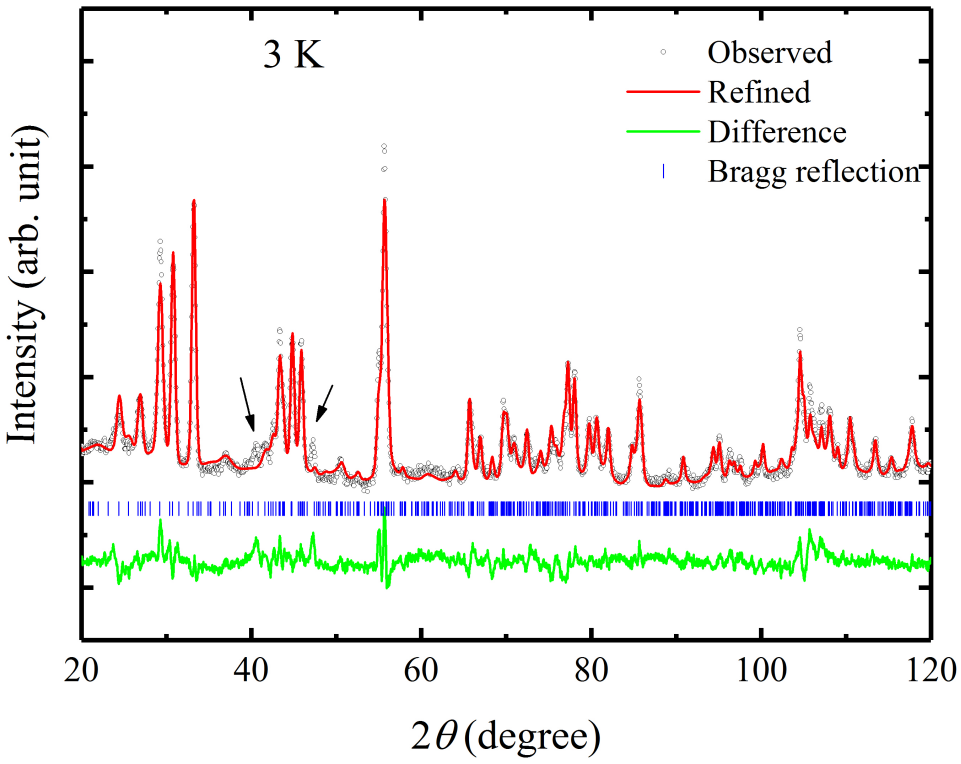

Figure 4.9: *Rietveld fitting of NPD pattern in the martensite phase at 3 K considering the uniform displacement model. Peaks due to the cryo-furnace wall material (Al) are marked by black arrows.*

by white rectangle, shown in the experimental HRTEM image. These atomic positions from HRTEM experiments are consistent with the simulated positions obtained by using Rietveld refined coordinates for the uniform displacement model. The thin TEM samples after *insitu cooling* does not always generate a perfect (4−2) twinned structure of six atomic planes obtained for the average structure using the bulk sample. The HRTEM images often show stacking faults, which locally could lead to different periodicities, say, of seven atomic planes.

The fast fourier transform (FFT) of the martensite structure along [210] zone axis is shown in Fig. 4.13(a). The corresponding simulated diffraction pattern using the positional coordinates of adaptive phase modulation along the [210] zone axis for $3-D$ rational approximant superstructure is shown in Fig. 4.13(b). These two data show an excellent match and confirms the uniform displacement model.

Table 4.4: *Atomic positions (x, y, z), amplitudes (A_1, A_2, B_1, B_2) of the modulation function, and atomic displacement parameter (U_{iso}) of the modulated martensite phase (235 K) of $Ni_2Mn_{1.4}In_{0.6}$ obtained from the Rietveld refinements of SXRPD data considering non-uniform displacement model.*

Atom	Wyckoff position	Modulation amplitude	x	y	z	U_{iso} (Å^2)
Ni1	$4h$		0.5	0.25	0	0.0002(5)
Mn1	$2a$		0	0	0	0.0002(5)
In1	$2d$		0	0.5	0	0.0002(5)
Mn2	$2d$		0	0.5	0	0.0002(5)
		A_1	0.1275(9)	0	0.005(1)	
		B_1	0	0	0	
		A_2	0.114(3)	0	0.004(2)	
		B_2	0	0	0	

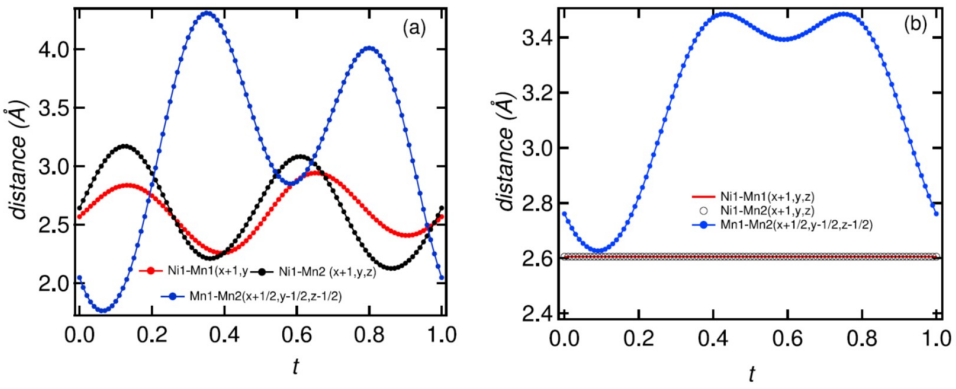

Figure 4.10: *Selected distance d as a function of t parameters derived from (a) Unphysical values (< 2 Å) from non-uniform atomic displacement model and (b) Expected values from uniform atomic displacement model for these kind of intermetallic compounds.*

4.2.6 Summary

The experimental results of magnetization, high resolution SXRPD and NPD were presented for $Ni_2Mn_{1.4}In_{0.6}$ MSM Heusler compound. The magnetization data of $Ni_2Mn_{1.4}In_{0.6}$ show the absence of premartensite phase which was further confirmed by a combined study of high resolution SXRPD and NPD using

Table 4.5: *Lattice parameters, space group and atomic positions of* $3-D$ *rational approximate structure of* $Ni_2Mn_{1.4}In_{0.6}$ *at 235 K derived from* $(3+1)-D$ *incommensurate structure for non-uniform displacement model.*

Atoms	Wyckoff position	x	y	z	Occupancy
Mn1	$1a$	0	0	0	1
Mn2	$1h$	1/2	1/2	1/2	1
Mn3	$2m$	0.00704	0	0.32342	1
Mn4	$2n$	0.67195	1/2	0.15906	1
In1	$1b$	0	1/2	0	0.6
In2	$1g$	1/2	0	1/2	0.6
In3	$2m$	0.75251	0	0.1256	0.6
In4	$2n$	0.99431	1/2	0.33461	0.6
Mn5	$1b$	0	1/2	0	0.4
Mn6	$1g$	1/2	0	1/2	0.4
Mn7	$2m$	0.75251	0	0.1256	0.4
Mn8	$2n$	0.99431	1/2	0.33461	0.4
Ni1	$2j$	1/2	1/4	0	1
Ni2	$2k$	0	3/4	1/2	1
Ni3	$4o$	0.59144	1/4	0.33676	1
Ni4	$4o$	0.13	3/4	0.16365	1

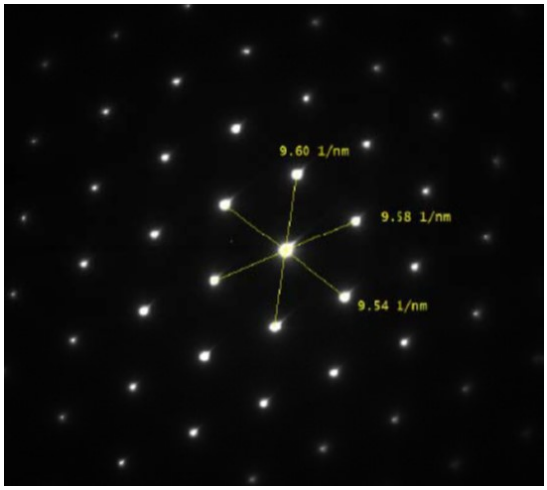

Figure 4.11: *(a) HRTEM pattern of* $Ni_2Mn_{1.4}In_{0.6}$ *for* $\langle 111 \rangle$ *zone in the austenite phase.*

Table 4.6: *Lattice parameters, space group and atomic positions of* $3-D$ *rational approximate structure of* $Ni_2Mn_{1.4}In_{0.6}$ *at 235 K derived from* $(3+1)-D$ *incommensurate structure for adaptive phase model.*

Crystal system: Monoclinic

Space group: $P2/m$

Cell (Å): $a = 4.3983(3)$, $b = 5.5858(2)$, $c = 12.9823(2)$ & $\beta = 92.796(9)^{o}$

Atoms	Wyckoff position	x	y	z	Occupancy
Mn1	$1a$	0	0	0	1
Mn2	$1h$	1/2	1/2	1/2	1
Mn3	$2m$	0.07781	0	1/3	1
Mn4	$2n$	0.64303	1/2	0.16954	1
In1	$1b$	0	1/2	0	0.6
In2	$1g$	1/2	0	1/2	0.6
In3	$2m$	0.64303	0	0.16954	0.6
In4	$2n$	0.07781	1/2	1/3	0.6
Mn5	$1b$	0	1/2	0	0.4
Mn6	$1g$	1/2	0	1/2	0.4
Mn7	$2m$	0.64303	0	0.16954	0.4
Mn8	$2n$	0.07781	1/2	1/3	0.4
Ni1	$2j$	1/2	1/4	0	1
Ni2	$2k$	0	3/4	1/2	1
Ni3	$4o$	0.57781	0.25	0.33376	1
Ni4	$4o$	0.14303	0.75	0.16954	1

$(3+1)-D$ superspace group approach. Rietveld analysis of high resolution SXRPD and NPD study shows uniform atomic displacement in the modulated structure with the absence of premartensite phase and phason broadening of the satellite peaks. HRTEM study also support uniform atomic displacement, observed by powder diffraction patterns. The modulated structure is commensurate with non integer modulation vector beacuse of nanotwinned state of Bain distorted phase. NPD data shows that the magnetic structure of martensite phase at 3 K is site disordered antiferrimagnetic in which two Mn atoms at two different crystallograhic positions are coupled antiferromagnetically. All these observations confirm that the structural modulation in $Ni_2Mn_{1.4}In_{0.6}$ magnetic shape memory compound can be explained in the term of adaptive phase model.

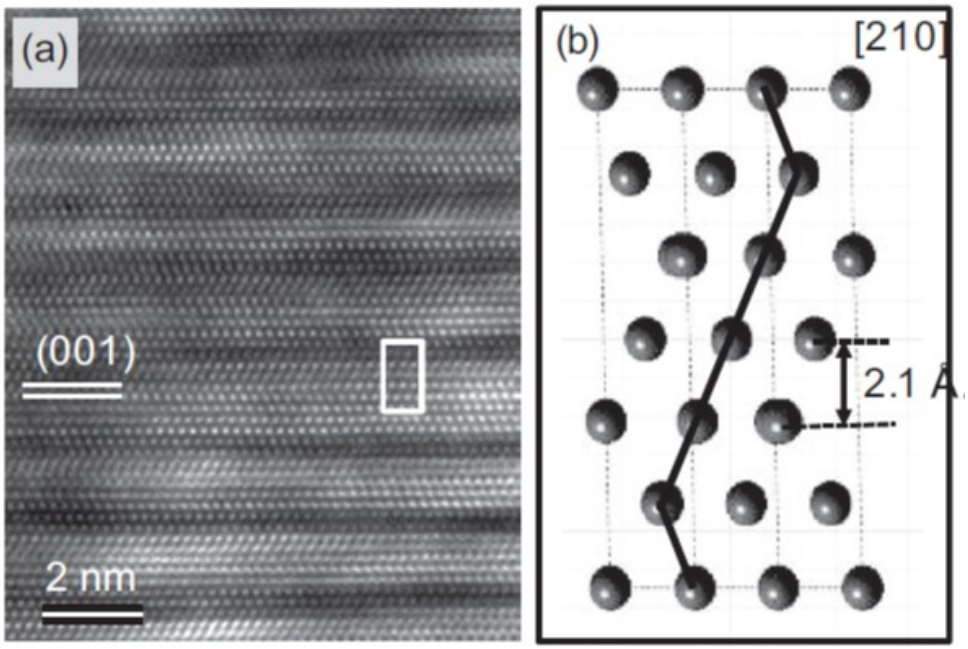

Figure 4.12: *(a) Noise filtered HRTEM image of $Ni_2Mn_{1.4}In_{0.6}$ crystal recorded along the [210] zone axis. The projected atom rows represented by the bright spots. The stacking of (001) basic planes (distance 2.1 Å) characterize the crystal lattice. It can be regarded as horizontal twinned lamellae. (b) The unit cell consisting of six (001) planes for crystal lattice model. The dark lines represents the specific stacking, following the uniform displacement model. The corresponding size of lattice structure is marked by rectangle in (a).*

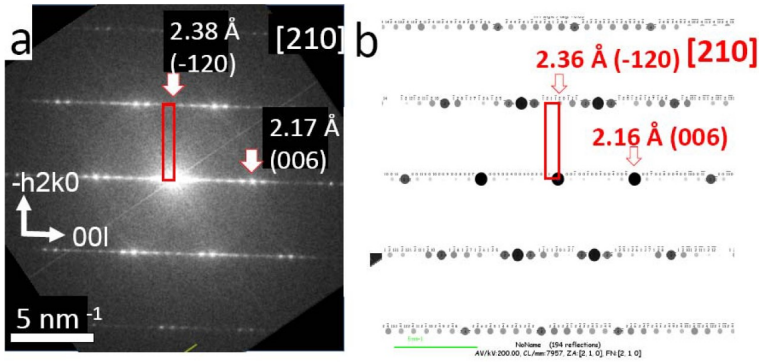

Figure 4.13: *(a) FFT of high-resolution pattern of $Ni_2Mn_{1.4}In_{0.6}$, along [210] zone axis. (b) The diffraction pattern of intensity distribution of reflections for [210] zone after simulation.*

4.3 Origin and Nature of Modulation in $Ni_{1.9}Pt_{0.1}MnGa$

Ni-Mn-Ga family is the most studied ferromagnetic shape memory compound due to its interesting properties like large MCE, large MFIS and large negative magnetoresistance. The origin of ferromagnetism in this compound is Runderman, Kittel, Kasuya and Yosida (RKKY) type indirect exchange interaction between Mn-Mn atoms which is mediated by Ni atom. The damped oscillatory nature of RKKY exchange coefficient results in FM or AFM magnetic coupling, which depends upon the separation between the pair of atoms. The largest value of MFIS $\approx$ 10% has been reported for $Ni_{1.95}Mn_{1.19}Ga_{0.86}$, which shows ferromagnetic behavior at Curie temperature ($T_C \approx 368$ K). The large MFIS in this material arises because of the modulated structure. The lower twinning stress of modulated structure results in easy movement of twin boundaries and hence results in large MFIS. MFIS is also observed in different systems such as $Ni_{1.95}Mn_{1.19}Ga_{0.86}$, $Ni_{2.28}Fe_{2.28}Ga$, $Ni_2Mn_{1.13}Ga_{0.8}Fe_{0.07}$ and $Ni_{2.04}Fe_{0.72}Co_{0.12}Ga_{1.08}$ because of the modulated structure in the martensite phase. Therefore, it is necessary to understand the crystal structure of these materials [162, 163].

Recently, a lot of studies were conducted to explain the modulated structure in Ni-Mn-Ga ferromagnetic shape memory compounds. Ni-Mn-Ga compounds show the martensite structure ($T_M \approx 210$ K) associated with the premartensite phase ($T_{PM} \approx 260$ K). This premartensite phase is known as precursor for the martensite phase transformation with the preserved austenite phase symmetry. Both the premartensite and martensite phase show the modulated structure [164]. It is necessary to understand the thermodynamic stability of premartensite phase and its relation to the martensite phase for the functional properties of these systems. There was a long lasting controversy about the order of modulation in premartensite and martensite phase. Singh *et al.* [165] confirmed from high resolution SXRPD that Ni_2MnGa shows the cubic $L2_1$ structure in the austenite phase. In the premartensite phase, the structure is $3M$ incommensurate with the preserved symmetry of austenite phase whereas, in martensite phase, the structure is orthorhombic $7M$ incommensurate with superspace group

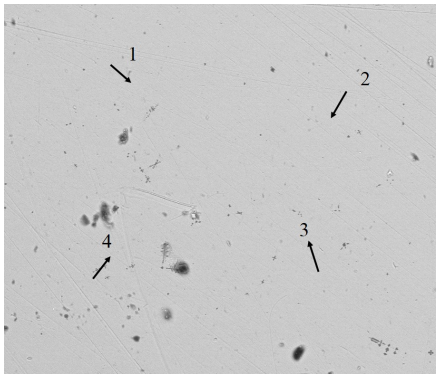

Figure 4.14: *RT SEM image of $Ni_{1.9}Pt_{0.1}MnGa$ at 50 μm. The black arrows indicate the areas where the composition was analyzed in detail.*

$Immm(00\gamma)s00$.

However, low temperature martensitic transition and brittleness hinder its technological applications and motivates for the search of other novel materials. In this aspect, $Ni_{2-x}Pt_xMnGa$ ($0 \leq x \leq 1$) shape memory compounds were prepared, which show higher transition temperature and better mechanical properties. In this section, a detailed investigation of modulated structure in $Ni_{1.9}Pt_{0.1}MnGa$ was studied experimentally by SXRPD and NPD.
Polycrystalline ingot of $Ni_{1.9}Pt_{0.1}MnGa$ was prepared from arc melting under argon atmosphere by taking appropriate quantities of the constituent elements with 3% more Mn. The ingot was sealed in vacuum with 300 mbar argon and annealed at 1173 K for 3 days for homogenization and subsequently quenched in ice water mixture. After that, the ingot was grounded into powder and then annealed at 773 K for 10 hours to remove the residual stress. This annealed powder was used for further characterization such as magnetization, SXRPD and NPD.

4.3.1 Scanning Electron Microscopy

Fig. 4.14 shows the SEM image of $Ni_{1.9}Pt_{0.1}MnGa$ at RT, which is clearly single phase. The composition was characterized by EDAX at four different spots, indicated by black arrows. The average composition turns out to be $Ni_{1.9}Pt_{0.1}MnGa$.

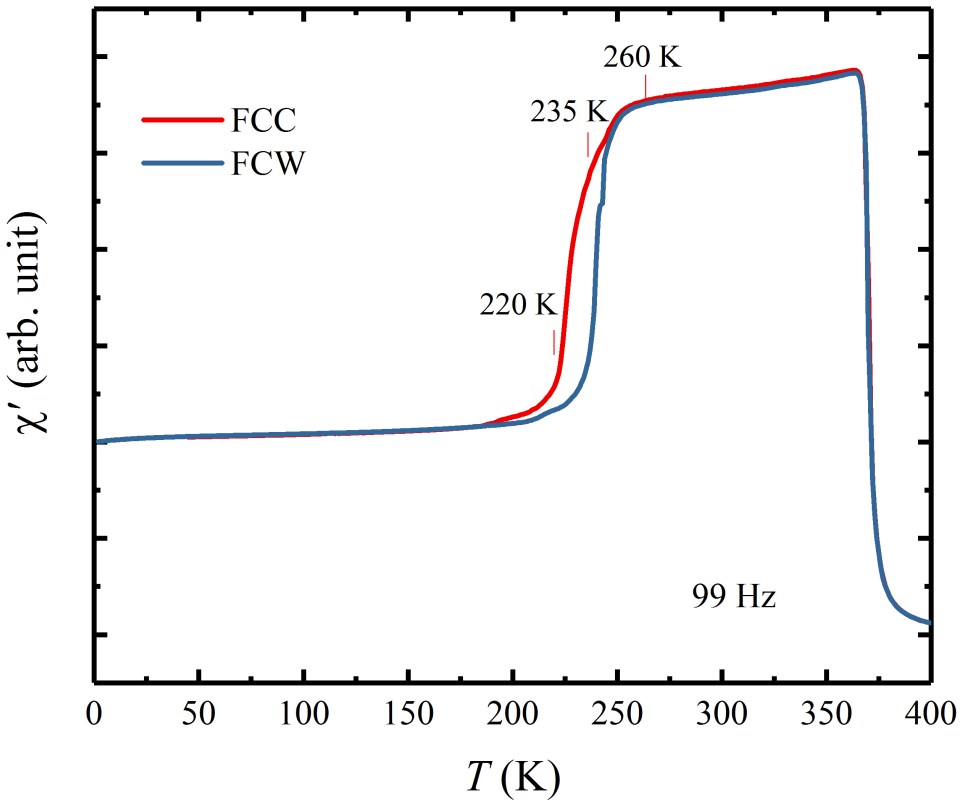

Figure 4.15: *Real part of ac-susceptibility of $Ni_{1.9}Pt_{0.1}MnGa$ for heating and cooling cycles as a function of temperature. Red tick marks present the different phases which were observed in the SXRPD data.*

4.3.2 Magnetization Measurements

The temperature dependence ac susceptibility measurement was done in VSM for powder sample, which was filled inside a capsule. Fig. 4.15 shows the temperature dependence ac-susceptibility measurement. It shows the sharp change from paramagnetic state to ferromagnetic state around $T_C \approx 370$ K. on further cooling there are two transitions: the first transition is observed from 260 to 235 K and another transition is from 235 to 220 K. The first transition from 260 to 235 K is observed with a small change in slope. The second transition from 235 to 220 K is observed with slightly larger slope. In general, the huge drop in ac susceptibility (or dc magnetization) in Ni-Mn based MSM Heusler compounds is because of the large magnetocrystalline anisotropy of the martensite phase in comparison to austenite phase. It is important to mention here that

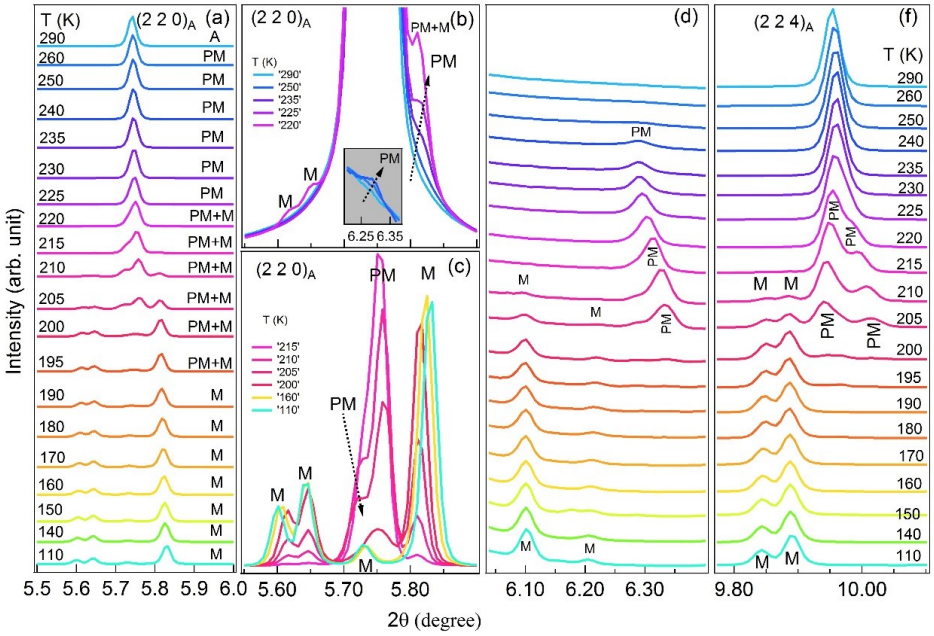

Figure 4.16: *High resolution SXRPD patterns of $Ni_{1.9}Pt_{0.1}MnGa$ for 3 selected 2θ ranges at different temperature during cooling cycles. The austenite peak (220) region is shown in (a), (b) and (c) represents the austenite peak (220) region on expanded scale, (d) satellite region and (e) (224) austenite peak region with an expanded scale for selected temperatures. Notation A, PM and M represents the Bragg peaks of the cubic austenite, premartensite and martensite phases, respectively. Inset in (b) shows the Bragg reflections on an expanded scale in 2θ range between 6.20 and 6.38 where the satellite reflection of 3M modulated premartensite phase is expected.*

about 40% of the drop of ac- susceptibility has been already occurred at 235 K in the premartensite phase as a result of 5% Pt substitution. Thus it seems that there are two premartensite phase transitions as a result of Pt substitution in Ni-Mn-Ga stoichiometric composition. This behavior is converse to the ac susceptibility or dc magnetization measurement of Ni-Mn-Ga as it shows only one dip in dc magnetization or ac susceptibility measurement.

4.3.3 High Resolution Synchrotron XRD

To confirm a clear correlation between the changes of slope in ac susceptibility, the temperature dependent high resolution SXRPD was measured in Desy Hamburg by using a wavelength of 0.20712 Å. These high resolution SXRPD patterns show a good agreement between the changes of slope in ac-susceptibility with temperature and structural changes in both premartensite and martensite phases. Fig. 4.16 shows the variation of SXRPD patterns from temperature 290 to 110 K in three selected 2θ ranges. This temperature range captures the entire sequence of austenite to martensite phase transition region. At 290 K, the SXRPD pattern is corresponds to the cubic austenite phase. Rietveld refinement gives an excellent fit between the observed and calculated peak profiles for the cubic structure (Fm-$3m$ space group) at 290 K. The refined lattice parameter $a = 5.84753(6)$ Å is slightly larger than the lattice parameter of stoichiometric Ni_2MnGa ($a = 5.82445$ (1) Å). It might be due to the larger size of Pt (1.77 Å) atom in comparison to Ni (1.37 Å) atom which is in good agreement with an earlier study. As the samples cool down from 290 K, several small intensity peaks appear in addition to the cubic austenite peak around 260 K. Two such peaks are marked on an expanded scale in Fig. 4.16(b) and in the inset of Fig. 4.16(b). These low intensity peaks are known as satellite peaks and appear due to the modulated nature of the premartensite phase already reported in Ni_2MnGa [102]. On further cooling up to $T = 240$ K, the intensity of satellite peaks increase without much effect on the cubic austenite peaks. Up to now, the situation is similar to the stoichiometric Ni_2MnGa, in which cooling below the premartensite phase transition temperature ($T_{PM} = 260$ K) leads to the appearance of low intensity peaks. The SXRPD in the temperature range from 260−240 K looks similar to the incommensurate $3M$-like modulated structure of the premartensite phase of Ni_2MnGa [102, 130, 131]. Therefore, Rietveld analysis of SXRPD of $Ni_{1.9}Pt_{0.1}MnGa$ was carried out at 240 K using $(3+1)-D$ superspace group approach by considering both main and the satellite reflections.

To refine the modulated structure of premartensite phase of $Ni_{1.9}Pt_{0.1}MnGa$, the same superspace group $Immm(00\gamma)s00$ was used. Fig. 4.17(b) shows a

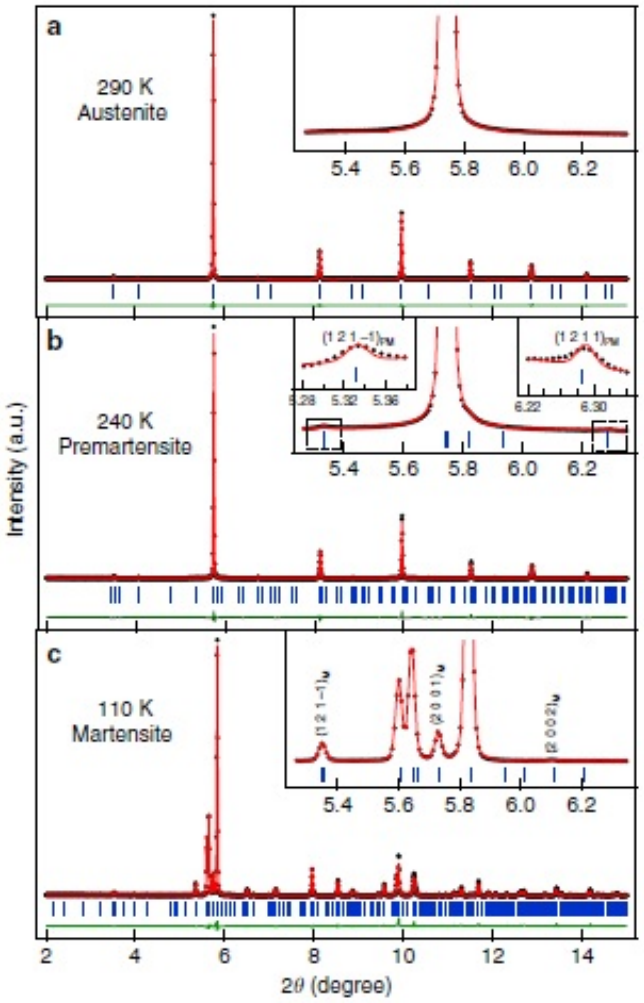

Figure 4.17: *Rietveld refinement of high resolution SXRPD patterns of* $Ni_{1.9}Pt_{0.1}MnGa$ *at (a) cubic austenite phase at 290 K, (b) premartensite phase at 240 K, (c) martensite phase at 110 K. The experimental data shown by black circles, fitted curve and residue are shown by red and green continuous lines respectively. The Bragg peak positions are represented by blue tick marks. Inset shows the fit for main peak region on an expanded scale (a), satellite reflections in the premartensite phase (b) and martensite phase (c) which are indicated as* $(hklm)_{PM}$ *and* $(hklm)_{M}$ *respectively.*

fit between observed and calculated peak profiles. At 240 K, the refined lattice parameters are found to be: $a = 4.1337(2)$ Å, $b = 5.8416(3)$ Å and $c = 4.1325(1)$ Å with a modulation wave vector ($\mathbf{q}$) of $\mathbf{q} = 0.325c^* = (1/3 - \delta)c^*$, where $\delta = 0.0083$ is the degree of incommensuration of modulation vector at 240 K. The

incommensurate nature of modulation is confirmed by magnitude of **q**. The approximant rational closest to the observed value is $(1/3)c^*$ suggesting $3M$-like modulation in the premartensite phase. Thus, the modulated structure of $Ni_{1.9}Pt_{0.1}MnGa$ in the premartensite phase in temperature range of 260-240 K, is identical to the premartensite phase of Ni_2MnGa. Both values of refined lattice parameters and modulation vector are close to the premartensite phase of Ni_2MnGa [131]. At 235 K, which is close to another slope change in ac susceptibility (marked with red tick in Fig. 4.15), the diffraction pattern shows another interesting feature. The spilitting of the Bragg peaks of cubic austenite structure begin to appear at 235 K (see Fig. 4.16(d) and (e)). However, there are no additional/new satellite reflections which means that this structure is corresponding to the premartensite phase only. Fig. 4.16(b) shows the satellite peaks marked with premartensite. This phase appears up to 225 K with the splitting of the cubic austenite peak which continue to increase from 235 K to 225 K. At T $\approx$ 220 K, new peaks have started appearing (marked with M in Fig. 4.16(c) $-$ (e)). This situation is similar to Ni_2MnGa, where new satellite peaks of premartensite phase appear after the premartensite phase is cooled below T_M [102]. These new intensity peaks grow at the expense of the premartensite phase peaks up to 190 K, whereas both main and satellite peaks of premartensite phase disappear completely. Below 190 K, there are no additional peaks in the structure up to lowest measurement temperature 110 K. No additional peak below 110 K appear as confirmed from the neutron diffraction measurements, explained in below part.

At 110 K in the martensite phase, Rietveld refinement was done using $(3+1)-D$ superspace group approach as in case of Ni_2MnGa. The main peaks that originate from the splitting of the cubic austenite peak could be indexed with an orthorhombic unit cell and in the space group $Immm$ similar to Ni_2MnGa. Le Bail refinement gives the following unit cell parameters a = 4.2390 (1) Å, b = 5.5682 (1) Å, and c = 4.2074 (1) Å. After that, the complete diffraction pattern including both main and satellite reflections was refined using the superspace group $Immm(00\gamma)s00$ with Rietveld refinement. An excellent fit between the observed and calculated profiles confirm that refinement has converged successfully. The incommensurate modulation vector was found to be $\mathbf{q} = 0.4290(2)c^* = (3/7+\delta)c^*$, where $\delta = 0.00112$ is the degree

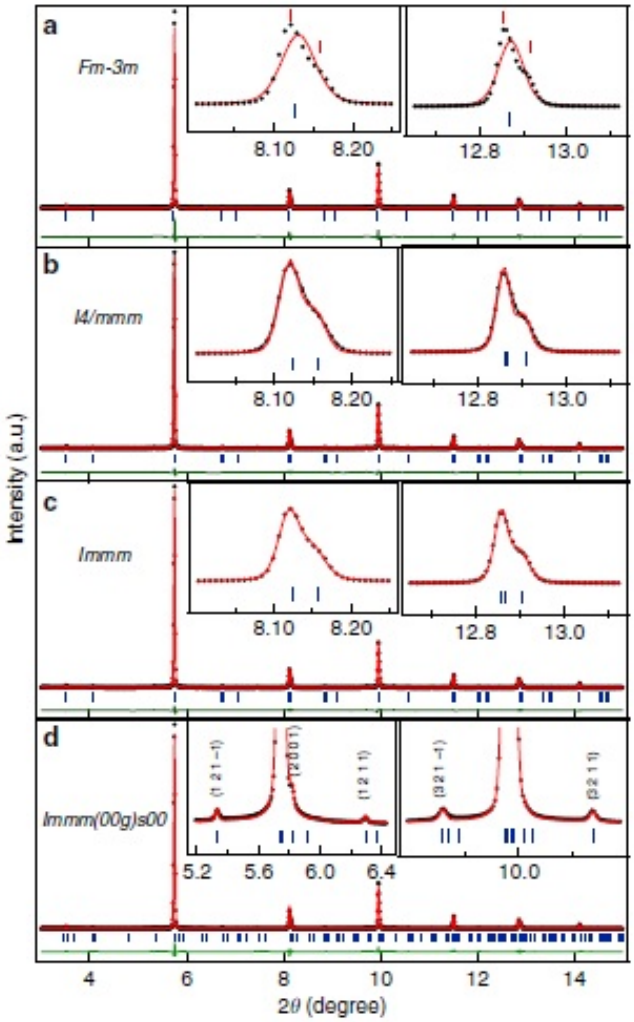

Figure 4.18: *Rietveld refinement of high resolution SXRPD patterns of $Ni_{1.9}Pt_{0.1}MnGa$ for main peaks at 225 K. (a) cubic austenite unit cell, (b) Bain-distorted tetragonal unit cell, (c) Orthorhombic unit cell, (d) 3M modulated incommensurate premartensite structure. Experimental data shown by black circles, fitted and residues by red and green continuous lines. Bluetick marks represent the Bragg peak positions. The inset in (a)-(c) show the fit for main reflections and (d) satellite reflections corresponding to the premartensite phase.*

of incommensuration. Thus, at 110 K, the refined structure shows nearly $7M$ type incommensurate modulated structure similar to the martensite phase of Ni_2MnGa [34, 132].

Thus, the structures of cubic austenite, premartensite in the temperature range from 260−240 K and at 110 K martensite (representative of the structure below 220 K) of $Ni_{1.9}Pt_{0.1}MnGa$, are similar to Ni_2MnGa. However, in the temperature range 235−195 K the structure of of the premartensite phase of $Ni_{1.9}Pt_{0.1}MnGa$ is quite unusual and shows only the splitting of the cubic austenite peaks without the presence of martensite peaks. This splitting of the cubic austenite peaks in the premartensite phase indicates the loss of pseudo-cubic symmetry of basic structure. This situation is unexpected in the premartensite phase as it is always considered to be a micromodulated phase and preserved cubic symmetry of the austenite peaks. At 225 K (representative of this new structure), Rietveld refinement presents the result between the calculated and observed intensities. First, Le Bail refinement was done using the cubic Fm-$3m$ space group by considering only main reflections (not satellites) similar to the Rietveld refinement of the premartensite and martensite phases stable in the temperature range of 245 K $< T <$ 260 K and $T <$ 225 K, respectively.

Fig. 4.18(a) shows that this model misses out of the new peaks, which arises due to the splitting of cubic austenite peaks (see the inset of Fig. 4.18(a)). It confirms the broken nature of cubic symmetry. So, the refinement was done by considering the tetragonal space group $I4/mmm$, which could capture the splitting but the observed and calculated peaks are not matching. In last, orthorhombic distortion (space group $I4/mmm$) was used for the martensite phase. It gives an excellent fit between the observed and calculated peak profiles (see Fig. 4.18(c) and inset). The refined unit cell parameters at 225 K of the basic structure are a = 4.1356 (2) Å, b = 5.8276 (2) Å, and c = 4.1371 (1) Å. It shows a clear evidence of the pseudo-tetragonal Bain distortion of the premartensite phase with $b/\sqrt{2}a \approx 0.9965$. In the next step, Rietveld refinement was done by considering the complete diffraction pattern including main and satellite reflections using superspace group $Immm(00\gamma)s00$. Rietveld refinement shows the excellent fit between observed and calculated peak profiles (Fig. 4.18(d) and inset). The refined modulation wave vector comes out to be $\mathbf{q} = 0.3393c^* = (1/3 + \delta)c^*$, where $\delta = 0.0059$ is the degree of incommensuration. These results of high resolution SXRPD data provide the evidence of new

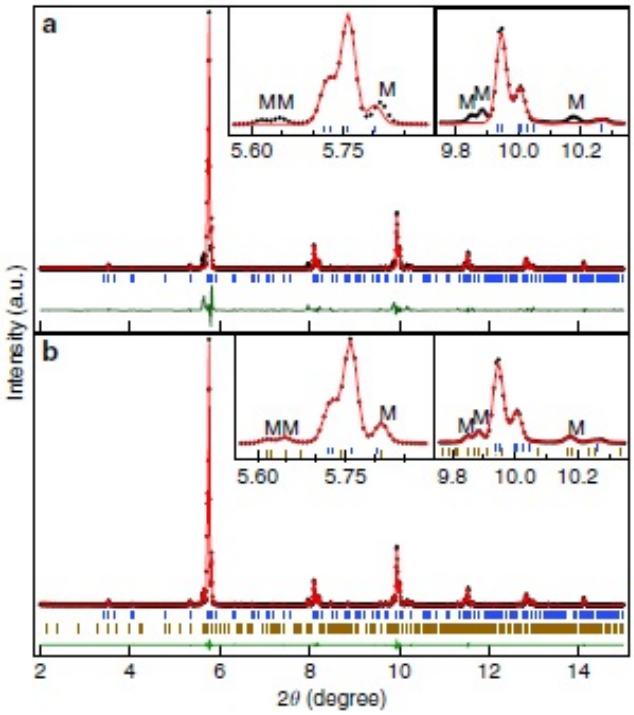

Figure 4.19: *Rietveld refinement of high resolution SXRPD patterns of $Ni_{1.9}Pt_{0.1}MnGa$ for main peaks at 225 K. (a) cubic austenite unit cell, (b) Bain-distorted tetragonal unit cell, (c) Orthorhombic unit cell, (d) 3M modulated incommensurate premartensite structure. Experimental data shown by black circles, fitted and residues by red and green continuous lines. Bluetick marks represent the Bragg peak positions. The inset in (a)-(c) show the fit for main reflections and (d) satellite reflections corresponding to the premartensite phase.*

incommensurately modulated $3M$-like premartensite phase with broken cubic austenite symmetry. $Ni_{1.9}Pt_{0.1}MnGa$ is the first example of macroscopic symmetry breaking and Bain distortion in the premartensite phase of MSM Heusler compound.

After observing, robust Bain distortion in the premartensite phase, the diffraction pattern was taken into consideration for the coexistence of the incommensurate $3M$-like Bain distorted premartensite and incommensurate $7M$-like martensite phase below 220 K. Fig. 4.19 shows the Rietveld refinement results of SXRPD data at 210 K. Inset of Fig. 4.19 shows the consideration of $3M$-like incommensurate premartensite phase which can not account some of the Bragg

reflections (marked as M in inset of Figure 4.19(a)). This diffraction pattern also can not be verified with single phase $7M$-like incommensurate martensite phase. In the next step, Rietveld refinement was done, based on the coexistence of both $3M$-like Bain distorted premartensite as well as $7M$- like martensite phase which gives an excellent fit between the observed and calculated profiles accounting for all of the peaks (Fig. 4.19(b)).
Thus, at 210 K, both $3M$-like premartensite and $7M$-like martensite phases coexist with incommensurate modulation. The superspace Rietveld refinement confirms the coexistence of $3M$-like and $7M$-like incommensurate structure in the entire temperature range of 210 to 195 K. The first-order phase transition is characterized by phase coexistence. These results show that the transition from Bain-distorted premartensite phase to the martensite phase, is a first-order phase transition. The martensite phase in $Ni_{1.9}Pt_{0.1}MnGa$ originates from the premartensite phase similar to Ni_2MnGa. However, a major difference in $Ni_{1.9}Pt_{0.1}MnGa$ arises because the premartensite phase from which the martensite phase results show robust Bain distortion. This situation is in contrast to Ni_2MnGa in which the martensite phase results from a premartensite phase that preserves the austenite cubic symmetry of the unit cell.

Fig. 4.20 shows temperature dependent lattice parameter variation and unit cell volume for the equivalent cubic, premartensite ($a_{\mathrm{pm}} \approx (1/\sqrt{2})a_c$, $b_{\mathrm{pm}} \approx a_{\mathrm{c}}$, $c_{\mathrm{pm}} \approx (1/\sqrt{2})a_{\mathrm{c}}$) and martensite phase ($a_{\mathrm{m}} \approx (1/\sqrt{2})a_c$, $b_{\mathrm{m}} \approx a_c$, $c_m \approx (1/\sqrt{2})a_{\mathrm{c}}$). The unit cell volume of all the phases decreases with decreasing temperature. However, the unit cell volume of the cubic austenite phase changes smoothly from austenite to the premartensite (T_1) phase transition in the temperature range (260-245 K), similarly to that in Ni_2MnGa as expected for a weak first-order phase transition [102]. On further lowering the temperature around $T \approx 235$ K, a discontinuous change in volume is observed with a concomitant spilitting of the cubic austenite peaks (see Figs. 4.20(a) and 4.16(e)) and a change in the slope of ac-susceptibility vs. temperature plot (see Fig. 4.15). Similarly, a discontinuous change in $\frac{b}{a}$ ratio with temperature (inset of Fig. 4.20) corresponding to the different phases is also observed. The formation of the premartensite phase (T_1) in the cubic austenite matrix is followed by robust Bain- distorted premartensite phase (T_2) in the premartensite (T_1) matrix.

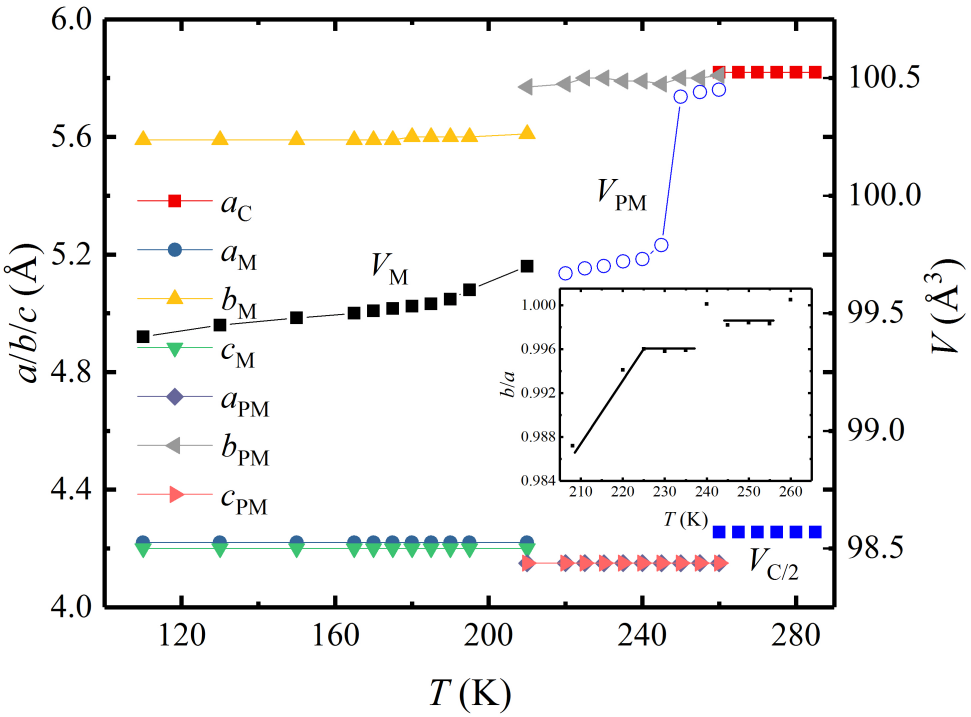

Figure 4.20: *Temperature dependence variation of $Ni_{1.9}Pt_{0.1}MnGa$ (a) the refined unit cell parameters a, b, c and volume in the austenite (A), 3M-like premartensite (PM), and 7M-like martensite (M) phase obtained from Rietveld refinement for the cooling cycles. The volume of cubic austenite phase is scaled with 1/2 for comparison. Subscripts C, PM, and M are used for cubic austenite, premartensite and martensite phases respectively. Inset shows the variation of b/a ratio (Bain distortion) with temperature of premartensite phase (T_1) and (T_2) respectively.*

Due to the gradual evolution of the Bain distortion, the fully Bain-distorted martensite phase through all transition in the premartensite (T_2) phase is kinetically more favorable for maintaining an invariant habit plane.

The displacement of atoms for premartensite phase (T_1) at 240 K and premartensite phase (T_2) at 225 K obtained from Rietveld refinement are compared in Fig. 4.21. These values are represented in table 4.7. It clearly indicates the atomic displacement change between two phases. This is an isostructural phase transition because of both premartensite phases belong to the same superspace group $Immm(00\gamma)s00$ in which the atomic positions shift without affecting

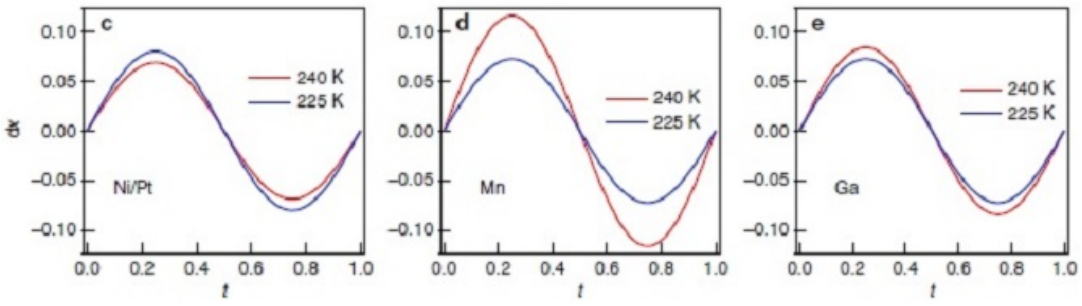

Figure 4.21: *The displacement (dx) of atoms for $Ni_{1.9}Pt_{0.1}MnGa$ show premartensite phase (T_1) at 240 K and premartensite phase (T_2) at 225 K with t parameter.*

the Wyckoff site symmetries and overall space group. The $3-D$ approximant structures of both premartensite phase (T_1) and premartensite phase (T_2) are compared in table 4.8. The unit cell parameters at the isostructural phase transition show discontinuous change which clearly reveals the presence of strong spin lattice i.e. magnetoelastic coupling. The isostructural phase transitions are reported in few compounds for example electronic transitions in chalcogenides under high pressure, between two ferroelectric phases, in $CaTiO_3$ between two antiferrodistorted structures and in multiferroics across the magnetic phase transition leading to excess spontaneous polarization due to magnetoelectric coupling [123, 125, 126, 127]. These results provide an evidence of an isostructural phase transition from a nearly cubic-like premartensite phase to a robust Bain-distorted premartensite phase in MSM Heusler compound $Ni_{1.9}Pt_{0.1}MnGa$.

At low temperature, an incommensurate phase can undergo a transition to the lock-in commensurate phase in ground state. Recently, Singh *et al.* [102] has shown that the modulation vector **q** shows a smooth analytic behavior down to 5 K in the stoichiometric Ni_2MnGa composition from high resolution SXRPD study. Ni_2MnGa does not show evidence of any devilish plateau or commensurate lock-in phase. Rietveld refinement of SXRPD data was carried out at various temperatures to determine the modulation vector **q** as a function of temperature down to 110 K. The modulation wave vector **q** variation with temperature is shown in Fig. 4.22. A jump of the modulation vector **q** is clearly

Table 4.7: *Atomic positions (x, y, z) and amplitudes A_i of the modulation function obtained from the Rietveld refinement of SXRPD data for the premartensite phases: T_1 at 240 K and T_2 at 225 K. Brown color parameters are corresponding to the*
Crystal system: Orthorhombic
Space Group: $Immm(00\gamma)s00$
Basic cell Å:
$T = 240$ K: $a^* = 4.1337(25), b^* = 5.8416(30), c^* = 4.1326(12)$
$T = 225$ K: $a^* = 4.1356(26), b^* = 5.8276(20), c^* = 4.1371(19)$
Modulation vector:
$T = 240$ K, $\mathbf{q} = 0.325c^*$
$T = 225$ K, $\mathbf{q} = 0.3376(5)c^*$

Atoms	Wyckoff position	Modulation amplitude	x	y	z	Occupancy	U_{iso} (Å^2)
Ni	4h		0.5	0.25	0	1.9	0.0115(19) [0.0122(6)]
Pt	4h		0.5	0.25	0	0.1	0.0115(19) [0.0122(6)]
		A_1	0.017(18) [0.0194(18)]	0	0		
Mn	2a		0	0	0	1	0.005(2) [0.0065(10)]
		A_1	0.03(2) [0.017(7)]	0	0		
Ga	2d		0	0.5	0	1	0.011(2) [0.0106(7)]
		A_1	0.020(17) [0.018(5)]	0	0		

Table 4.8: *Lattice parameters, space group and atomic positions of* $3-D$ *rational approximate structure of* $Ni_{1.9}Pt_{0.1}MnGa$ *derived from* $(3+1)-D$ *incommensurate premartensite* T_1 *at 240 K and* T_2 *at 225 K.*

Crystal system: Orthorhombic
Space Group: *Pnmn*
Lattice parameters:
$T = 240$ K: $a = 4.1337$ Å, $b = 5.8397$ Å, $c = 12.4001$ Å
$T = 225$ K: $a = 4.138969$ Å, $b = 8.27392$ Å, $c = 12.40434$ Å

Atoms	Wyckoff position	x	x	y	z	Occupancy	U_{iso} (Å^2)	U_{iso} (Å^2)
Mn1	2b	0	0	0	0	1	0.004796	0.006459
Mn2	4g	0.0244	0.0146	0	1/3	1	0.004796	0.006459
Ga1	2a	0	0	1/2	0	1	0.011083	0.01063
Ga2	4g	0.0176	0.0152	1/2	1/3	1	0.011083	0.01063
Ni1	4f	1/2	1/2	1/4	0	0.95	0.011497	0.012245
Ni2	8h	0.5144	0.5168	1/4	1/3	0.95	0.011497	0.012245
Pt1	4f	1/2	1/2	1/4	0	0.05	0.011497	0.012245
Pt2	8h	0.5144	0.5168	1/4	1/3	0.05	0.011497	0.012245

observed from $3M$ modulated premartensite phase (T_1) to premartensite phase (T_2) through an isostructural phase transition while both phase continue to remain incommensurate. A discontinuous change in the modulation vector $\mathbf{q}$ is also accompanied from the incommensurate $3M$-like premartensite phase (T_2) to the $7M$-like incommensurate martensite phase which confirms the first-order nature of this transition as well. It is consistent with the observation of discontinuous change in phase coexistence and volume around T_{M}. Interestingly, the value of $\mathbf{q}$ for premartensite phase (T_1) is slightly less than the value 0.33 of commensurate modulation vector while, the modulation vector $\mathbf{q}$ of premartensite phase T_2 is slightly larger than 0.33. Both premartensite phases give an incommensurate modulation vector. However, the possibility of modulation vector $\mathbf{q}$ passing through 0.33 ($\frac{1}{3}$) commensurate value in the discontinuous jump region with a plateau for modulation vector $\mathbf{q}$ of $\frac{1}{3}$ can not be ruled out.

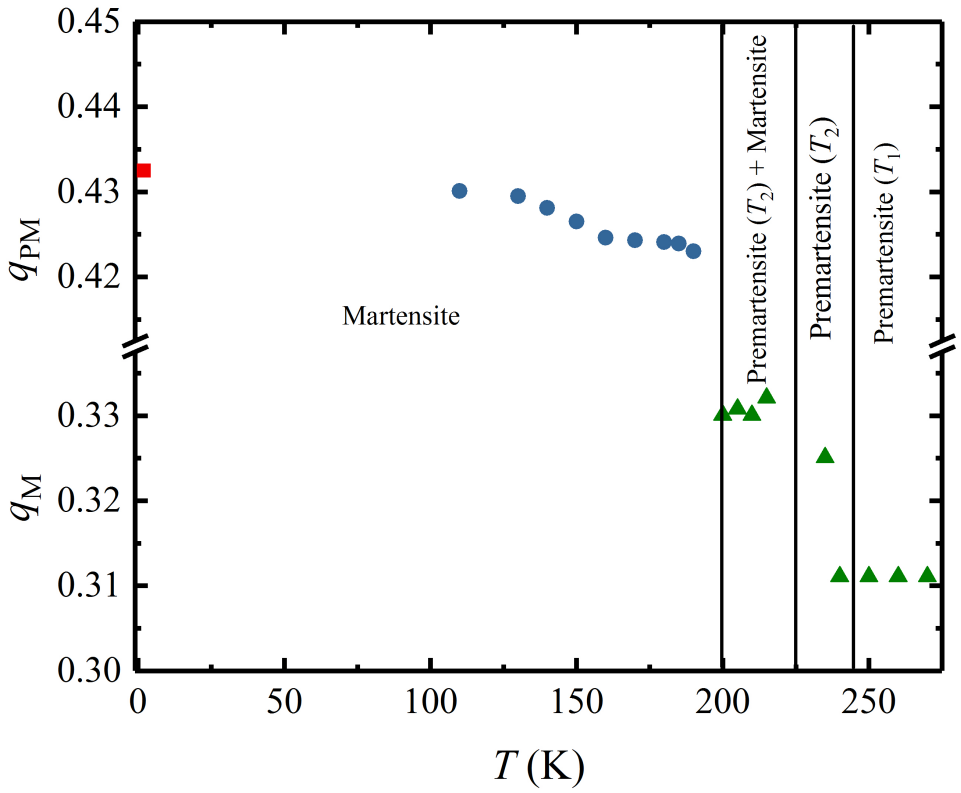

Figure 4.22: *Temperature dependent variation of the magnitude of modulation vector* $\mathbf{q}$ *as a function of temperature obtained from superspace Rietveld refinement during cooling. Different phases are separated by solid line.*

4.3.4 Neutron Powder Diffraction

The verification that the incommensurate phase would lock-into a commensurate phase in the ground state was also done at 10 K by Le Bail refinement of high resolution NPD data as shown in Fig. 4.23. The lattice parameters obtained from Rietveld refinement of NPD pattern are $a = 4.2445(9)$ Å, $b = 5.5504$ (11) Å, $c = 4.2086$ (8) Å and the value of incommensurate modulation vector $\mathbf{q} = 0.4324 \pm 0.0002$. This $\mathbf{q}$ value confirms that $Ni_{1.9}Pt_{0.1}MnGa$ exhibits incommensurate structure down to 10 K. The behavior of $\mathbf{q}$ remains smooth analytic in the entire temperature range of stability of the martensite phase without any intermediate or commensurate lock-in phase of ground state in Pt substituted Ni_2MnGa. This is similar to the undoped composition of Ni_2MnGa[102].

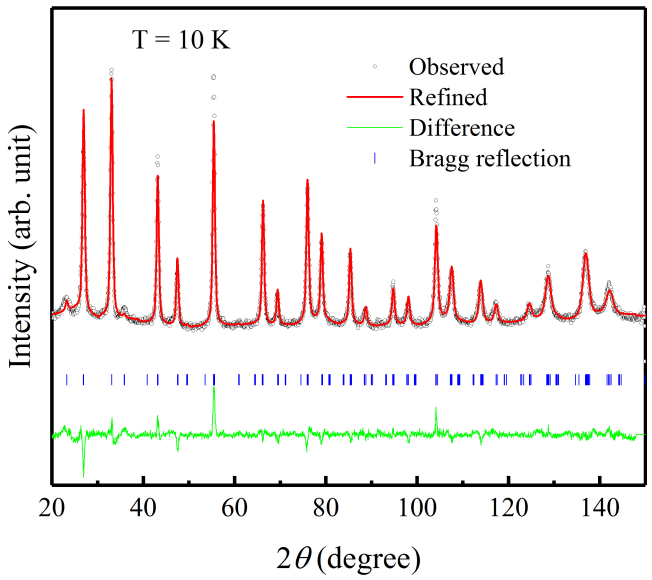

Figure 4.23: *Le Bail refinement for the neutron diffraction pattern at 10 K. The experimental data are shown by black circles, fitted and residues are shown by red and green continuous lines, respectively. The blue tick marks represent the Bragg peak positions.*

4.3.5 Summary

The ac susceptibility measurement of $Ni_{1.9}Pt_{0.1}MnGa$ powder sample shows the presence of premartensite phase unlike in $Ni_2Mn_{1.4}In_{0.6}$ MSM Heusler compound. This premartensite phase was believed to be precursor for martensite phase in Ni_2MnGa MSM Heusler compound. Here, the evidence for macroscopic symmetry breaking leads to robust Bain distortion in the premartensite phase of Ni_2MnGa as a result of 5% Pt substitution has been shown from Rietveld refinement of high resolution SXRPD patterns. The robust Bain distorted premartensite phase (T_2) results from another premartensite phase (T_1) which has preserved austenite cubic like symmetry through an isostructural phase transition. On further cooling, the martensite phase has been observed from the premartensite phase (T_2) with additional Bain distortion. Le Bail refinement of NPD data at 10 K shows that the incommensurate phase would lock-into a commensurate phase in the ground state. All these observations (incommensurate ground state, inhomogenous atomic displacement and presence of phasons in the modulated phase) are explicable within the framework of the soft

phonon mode model as the most plausible model for the origin of modulation in $Ni_{1.9}Pt_{0.1}MnGa$ MSM Heusler compound.

These studies of $Ni_{1.9}Pt_{0.1}MnGa$ MSM Heusler compound underline the importance of superspace group analysis of the diffraction data to understand the physics behind the modulation and critically evaluate the applicability of two existing models for the origin of modulation in magnetic shape memory Heusler compounds. The origin of modulated structure in different Ni-Mn based magnetic shape memory Heusler compounds may not be universal and it must be investigated thoroughly in different material compositions.

5 MCE in $Ni_{2+x}Mn_{1-x}Z$ (Z= In, Ga) Heusler compounds

Among the promising materials for MCE, Ni-Mn based MSM Heusler compounds are attractive candidates for both fundamental research and application point of view. These compounds show first-order martensitic phase transition from high temperature, high symmetry cubic austenite phase to low temperature, low symmetry martensite phase [28, 52, 144, 145, 147, 151, 148]. First-order phase transition involves both structure and magnetic entropy, while second-order phase transition has only magnetic contribution. Due to this, first-order phase transition results in higher value of MCE in comparison to second-order phase transition [16, 52, 53, 68]. This chapter shows the MCE in two different MSM Heusler compounds $Ni_{2.2}Mn_{0.8}Ga$ and $Ni_{1.8}Mn_{1.8}In_{0.4}$. First, the magnetic properties of magnetostructural transition were studied from the field dependent and temperature dependent magnetic isotherms. Since, the value of MCE is related to the magnetization change between austenite and martensite, width of thermal and magnetic hysteresis and magnetic moment. Therefore, a careful analysis of magnetization measurement was done by applying large no. of magnetic fields. In next step, the isothermal entropy change was calculated from these magnetization measurements to get an indication of the reversibility. This topic is followed by the measurement of adiabatic temperature change in pulsed magnetic field. The reversibility of adiabatic temperature change was confirmed by applying more than one pulse at different temperatures. The origin of reversibility was explained on the basis of GCC for different kind of structures, which is calculated from the lattice parameters of both austenite and martensite phase. In the last section, powder x-ray diffraction was collected in both phases. The unit cell parameters were calculated from Le Bail refinement.

5.1 Overview of the MCE

Conventional MCE is observed in the austenitic phase around the ferromagnetic transition. An increase in the sample temperature is observed by applying magnetic field adiabatically. In addition to that, inverse MCE is observed around the martensitic first-order phase transition which leads to a decrease in the sample temperature with increasing magnetic field. For Ni-Mn based MSM Heusler compounds, the total adiabatic temperature change at the first-order martensitic phase transition can be written as $\Delta T_{\mathrm{ad}} = \Delta T_{\mathrm{ad}}^{str} + \Delta T_{\mathrm{ad}}^{\mathrm{mag}}$, where $\Delta T_{\mathrm{ad}}^{\mathrm{str}}$ and $\Delta T_{\mathrm{ad}}^{\mathrm{mag}}$ denote the structural and magnetic contribution of the temperature change, respectively. If we apply the magnetic field adiabatically, then magnetic moments align which heats up the sample $\Delta T_{\mathrm{ad}}^{\mathrm{mag}} > 0$. During same time, the structural phase transition from the low-symmetry and low-temperature martensitic phase to the high-temperature high-symmetry austenitic phase leads to a very large cooling effect. Thus, the heat absorption due to the structural transformation exceeds the heat release from the magnetic subsystem. As a result, the sample temperature decreases $\Delta T_{\mathrm{ad}} < 0$ by applying the magnetic field adiabatically [28].

5.2 MCE in $Ni_{2.2}Mn_{0.8}Ga$

Ferromagnetic shape memory compounds are good candidates for the use in magnetic cooling technology because of small volume change at the martensite transition and high lattice coherence results in fast kinetics of thermoelastic transformation. Therefore, a lot of study for MCE in $Ni_{2+x}Mn_{1-x}Ga$ has been reported in literature [27, 139, 140, 149, 150]. A small substitution of 3d or 5d transition metal in $Ni_{2+x}Mn_{1-x}Ga$ changes the magnetic moment and martensite transition temperature which affects the MCE properties [151, 152]. Polycrystalline ingot of $Ni_{2.2}Mn_{0.8}Ga$ was prepared by arc-melting from the constituent elements of Ni, Mn and Ga under Ar- atmosphere. The procedure was repeated several times to ensure good homogeneity. These prepared ingots were wrapped in Mo foil and annealed in quartz tube at 900°C for 3 days and then quenched in ice water mixture. The high quality of the samples was confirmed by SEM.

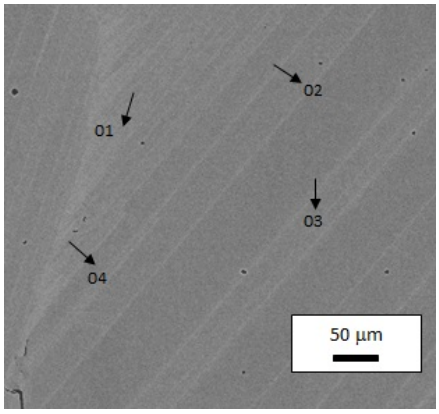

Figure 5.1: *RT SEM image of $Ni_{2.2}Mn_{0.8}Ga$. The black arrows indicate the areas, where the composition was analyzed in detail.*

5.2.1 Scanning Electron Microscopy

A careful analysis by a SEM in backscattered electron detection configuration revealed that the sample is single phase with a homogeneous composition distribution. The SEM image is shown in Fig. 5.1, which contains some black dots. These black dots represent unreacted Mn. The composition analysis was done by energy dispersive analysis of x-rays (EDAX) at different spots, indicated by arrows in Fig. 5.1. The final nominal composition turns out to be $Ni_{2.19}Mn_{0.81}Ga$.

5.2.2 Magnetization Measurements

The temperature-dependent magnetization curves $M(T)$ of $Ni_{2.2}Mn_{0.8}Ga$ were measured in external magnetic fields of 0.01 T and 6 T during cooling and heating cycles as shown in Fig. 5.2. Upon cooling, the austenitic to the martensitic phase transition starts at $M_s = 323$ K (martensite start temperature) and ends at $M_f = 315$ K (martensite finish temperature). Upon heating, the reverse transformation, martensite to austenite, is found to start at $A_s = 320$ K (austenite start temperature) and to finish at $A_f = 328$ K (austenite finish temperature). The hysteresis width observed from these characteristic temperatures is about 5 K, which is small in comparison with other MSM Heusler compounds [29, 64, 140, 141, 143]. $M(T)$ curves show that the martensitic transition shifts

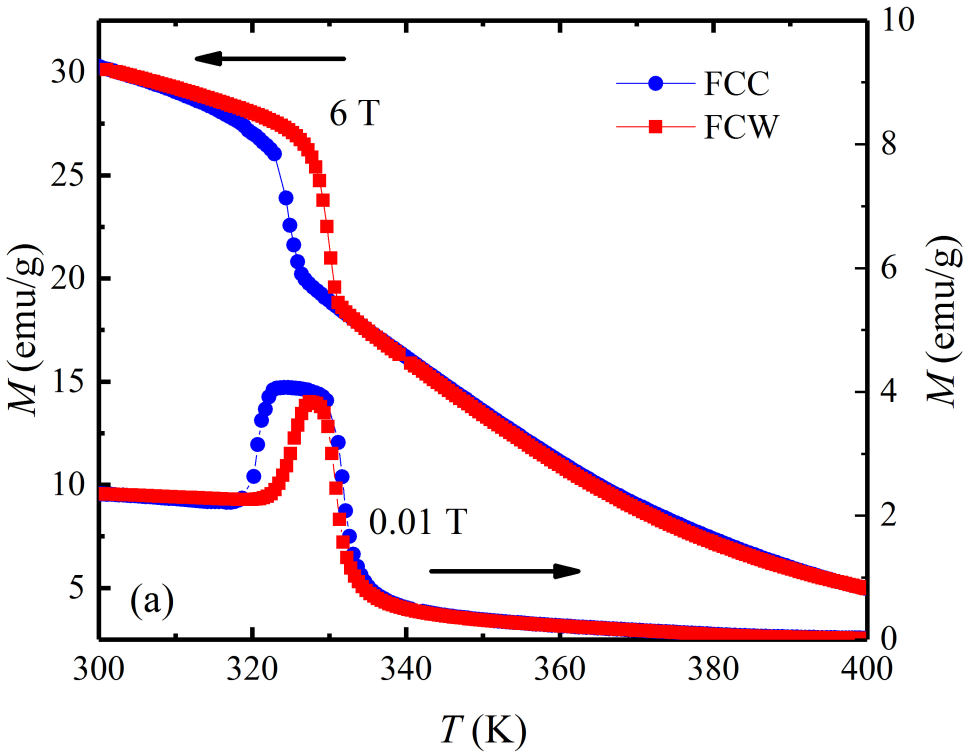

Figure 5.2: *Field cooled warming and cooling magnetization $M(T)$ curves at 0.01 T and 6 T for $Ni_{2.2}Mn_{0.8}Ga$.*

towards to higher temperatures by applying magnetic field of 6 T (see Fig. 5.2). Since, magnetic field stabilizes the phase with the higher magnetic moment, in this case the martensitic phase. Therefore, the transition from austenite to martensite can be induced by magnetic field. However, the temperature range at which this transition can be induced is limited by the shift of the transition with magnetic field. Motivated by the very small thermal hysteresis, we recorded magnetization data as a function of the magnetic field using two different protocols to determine the magnetic hysteresis. Following protocol 1, the sample was heated to the austenite phase up to 400 K, then cooled in zero field down to 200 K to ensure the sample being fully in the martensite phase, and then subsequently heated up to the measurement temperature where the $M(H)$ data were taken (see Fig. 5.3). In protocol 2, $M(H)$ loops were recorded one after the other without any thermal cycling as typically used for second-order phase transitions as shown in Fig. 5.4 . The data do not show any signifi-

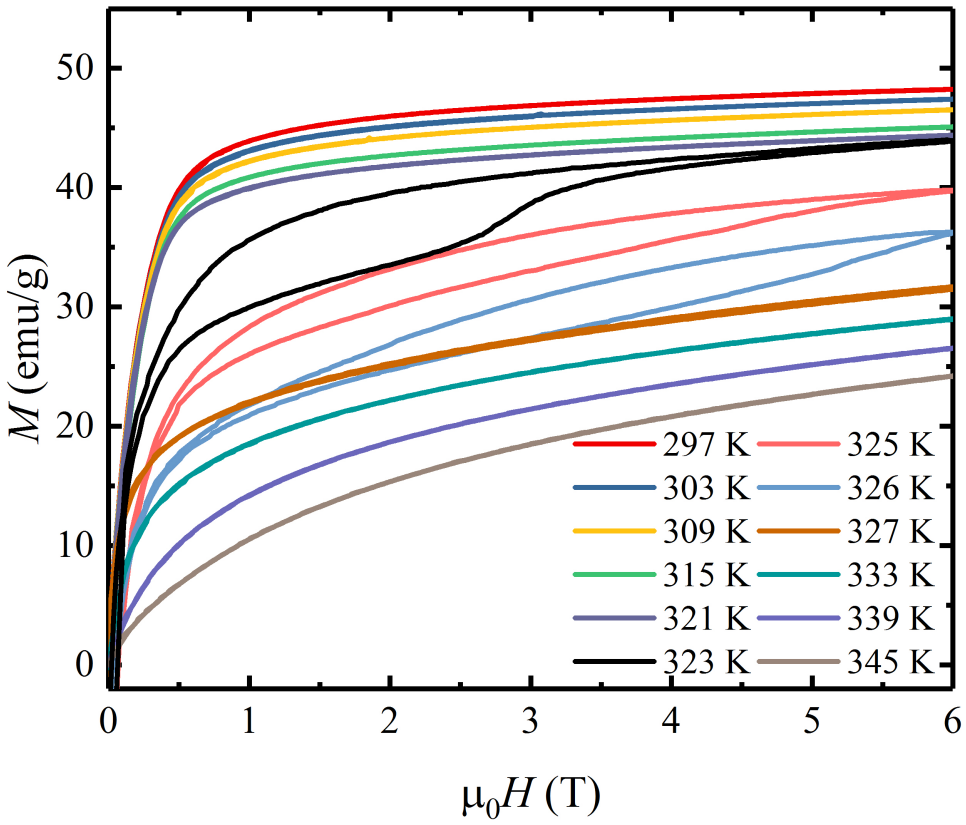

Figure 5.3: *$M(H)$ isotherms of $Ni_{2.2}Mn_{0.8}Ga$ with protocol 1(sample was overheated to austenite and then undercooled to the martensite before approaching the target temperature) in static magnetic field up to 6 T from 297 to 345 K at 6 K temperature difference, including field induced transition at 323, 325 and 326 K.*

cant difference in the isothermal $M(H)$ curves recorded using the two different protocols. This gives an indication of reversible behavior of MCE.

5.2.3 Isothermal Entropy Change from *M(H)* Measurements

The magnetic entropy change (ΔS_{M}) from these isothermal $M(H)$ curves using following Maxewell's equation:

$$\Delta S_M = S(T,H) - S(T,0) = \int_0^H \left(\frac{\partial M}{\partial T}\right)_H dH. \tag{5.1}$$

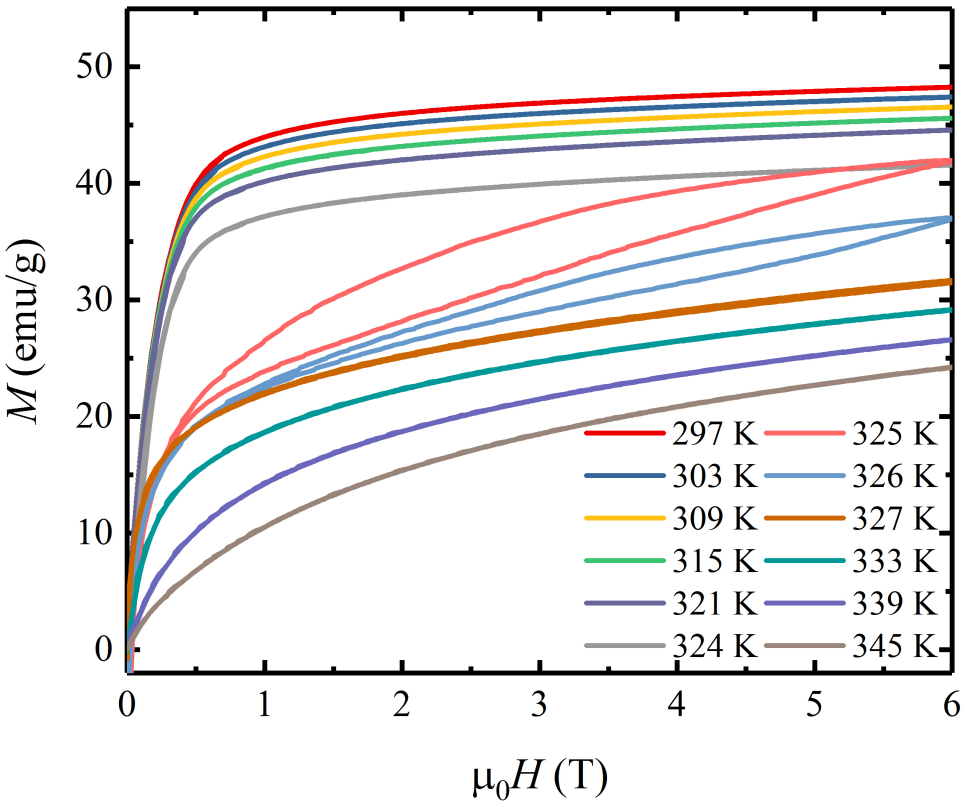

Figure 5.4: *$M(H)$ isotherms of $Ni_{2.2}Mn_{0.8}Ga$ with protocol 2 (target temperature was reached without overheating and undercooling) taken at different temperatures in static magnetic fields up to 6 T between 297 and 345 K at 6 K temperature difference. It includes field induced transition temperatures 324, 325 and 326 K.*

As expected, the $\Delta S_{\mathrm{M}}(T)$ curves show almost identical values for both protocols at all measured magnetic fields (see Fig. 5.3 and 5.4). We only got a minor difference between at 300 K for both protocol values in a magnetic field of 1 T. This difference in the martensite phase could be explained by a twinning of the martensite [154]. The small thermal hysteresis, reversibility in magnetization in the region of the martensitic transformation, and similar values of ΔS_{M} obtained for both protocols indicate that $Ni_{2.2}Mn_{0.8}Ga$ is a promising candidate for the observation of a reversible MCE and for future magnetocaloric applications.

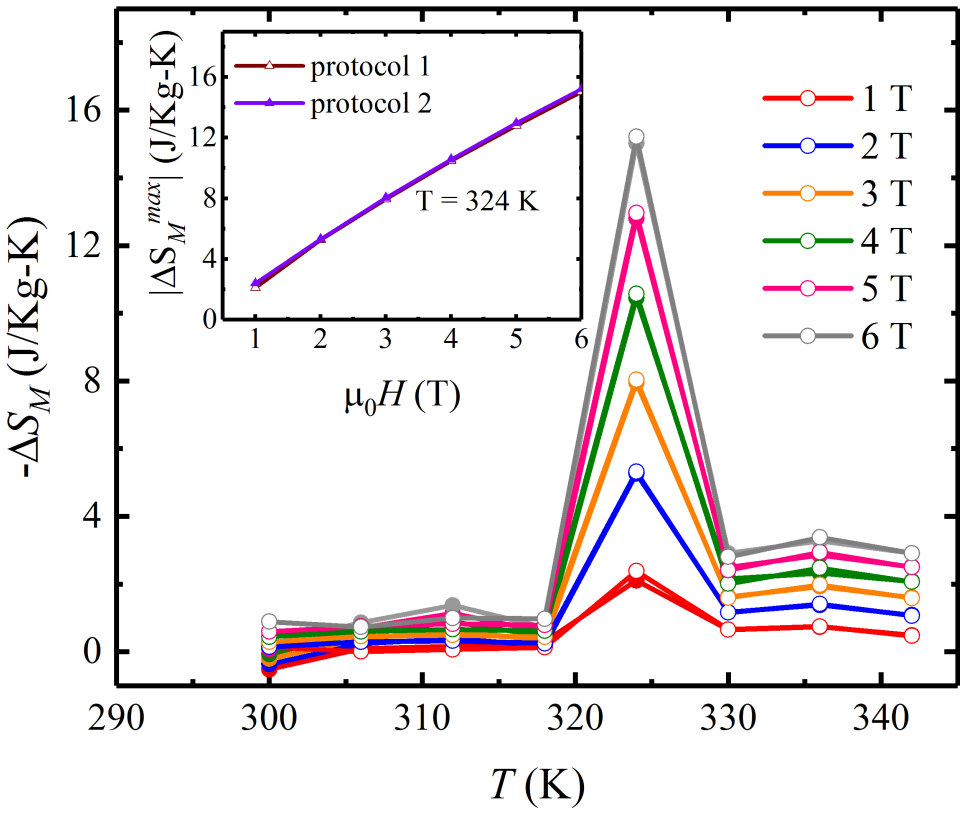

Figure 5.5: *Isothermal magnetic entropy of $Ni_{2.2}Mn_{0.8}Ga$ as a function of temperature under different applied magnetic fields shown by solid and open circles for protocol 1 and 2, respectively. Inset shows the variation of ΔS_M for different magnetic field at $T = 324$ K for both protocols.*

5.2.4 Isothermal Entropy change from *M(T)* Measurements

The isothermal magnetic entropy change ΔS_{M} calculated from the magnetization isotherms $M(T)$ is depicted in Fig. 5.6. The plot of ΔS_{M} exhibits a peak calculated from $M(T)$ curves measured upon heating and cooling, respectively. The peak values of ΔS_{M} calculated from $M(T)$ measurements exhibit higher value upon heating from cooling for both magnetic field change of 0 to 2 T and 0 to 6 T. The maximum value of $\Delta S_{\mathrm{M}} = 30$ J/Kg-K upon heating at the reverse martensitic temperature is larger than the value at the direct transformation $\Delta S_{\mathrm{M}} = 23$ J/Kg-K upon cooling in a magnetic field change of 6 T. The curve and maximum value of ΔS_{M} calculated from $M(T)$ measurements slightly dif-

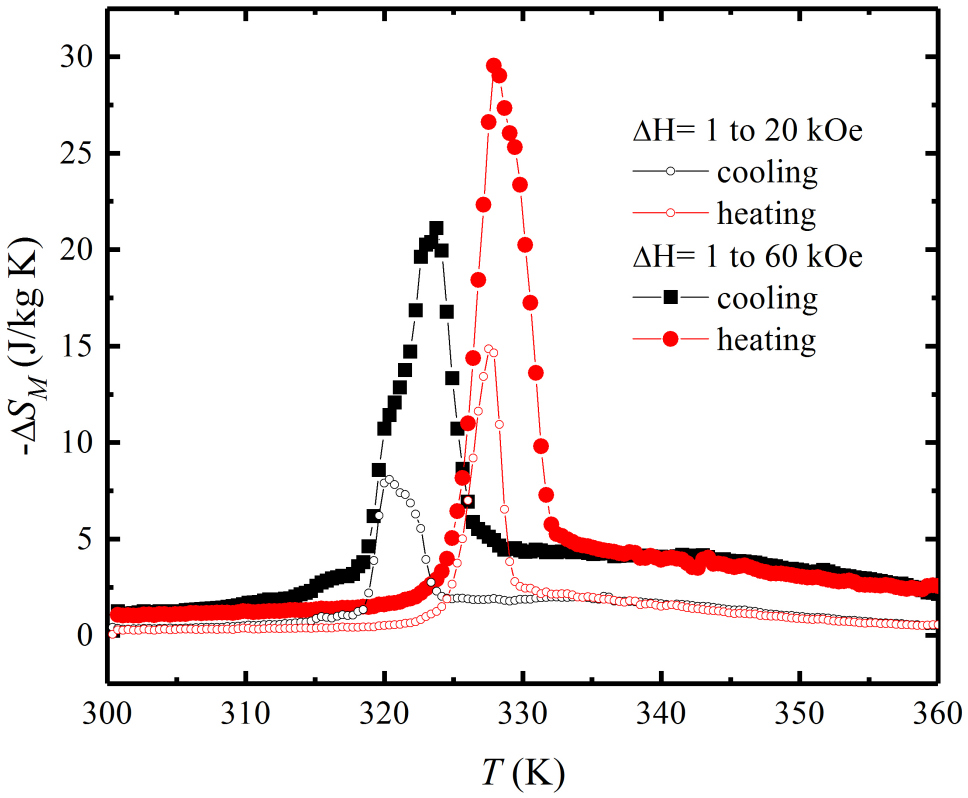

Figure 5.6: *Isothermal magnetic entropy change* ΔS_M *of* $Ni_{2.2}Mn_{0.8}Ga$ *calculated from* $M(T)$ *curves.*

fer from the isothermal $M(H)$ measurements. This difference arises because of the magnetization change, ΔM, is larger upon the reverse martensitic transition [140, 142].

5.2.5 Adiabatic Temperature Change in Pulsed Magnetic Field

Fig. 5.7 shows selected $\Delta T_{\mathrm{ad}}(t)$ as a function of time at different temperatures for a 6 T pulsed magnetic field. All plotted data were recorded after reaching the measurement temperature on cooling from 350 K or from the previous measured temperature. It is important to note that for all temperatures, $\Delta T_{\mathrm{ad}}(t)$ goes back to the initial value before the pulse applies. This indicates the reversibility of the MCE. The inset of Fig. 5.7 displays $\Delta T_{\mathrm{ad}}^{\mathrm{max}}$, taken as the maximum in the

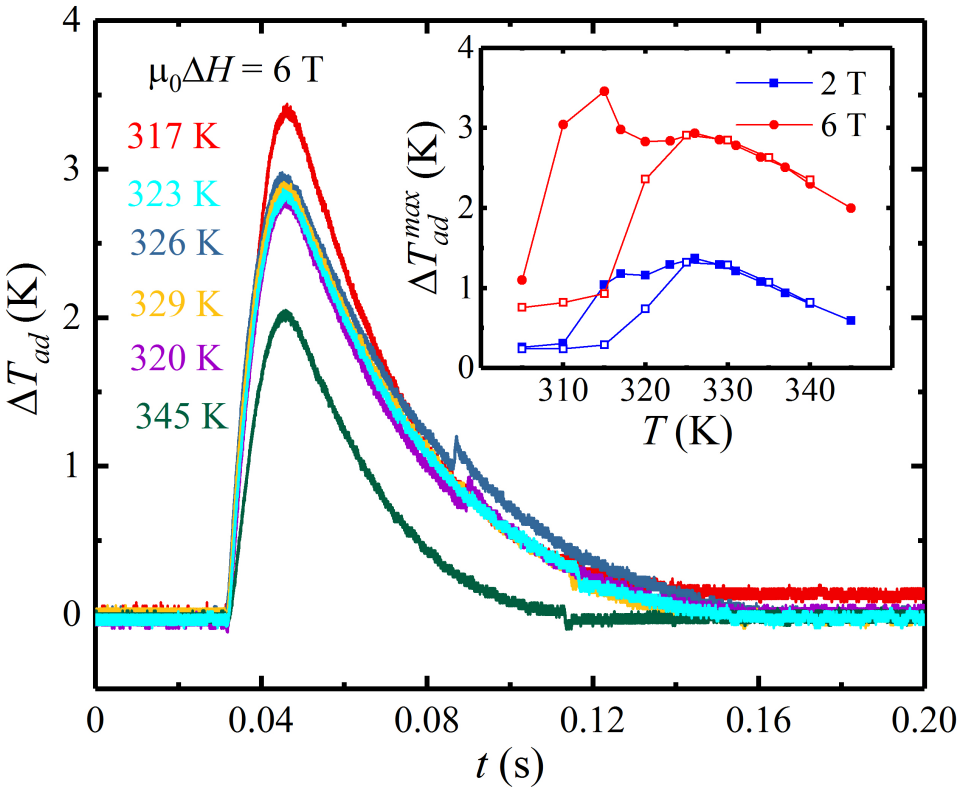

Figure 5.7: *Adiabatic temperature change, ΔT_{ad}, of $Ni_{2.2}Mn_{0.8}Ga$ as a function of time at 6 T magnetic field for different temperatures reached on cooling protocol. Inset shows ΔT_{ad}^{max} as a function of temperature for pulsed fields of 2 and 6 T. Open symbols represent data taken upon heating and closed upon cooling.*

$\Delta T_{\mathrm{ad}}(t)$ curve, for applied magnetic fields of 2 and 6 T, recorded both on cooling and heating. For both fields, the broad shape of the maximum in the $\Delta T_{\mathrm{ad}}^{\mathrm{max}}$ curve, which is desirable for applications, covers a temperature window of about 35 K. Under a magnetic pulse of 6 T, $\Delta T_{\mathrm{ad}}^{\mathrm{max}}(T)$ reaches its maximum of 3.5 K.

To achieve higher efficiencies in magnetic cooling devices, the reversibility upon magnetic field cycling is crucial. To study the reversibility of the MCE in $Ni_{2.2}Mn_{0.8}Ga$, $\Delta T_{\mathrm{ad}}(t)$ was measured for three subsequent 6 T magnetic field pulses at 326 K, which is just above the martensite start temperature, $M_{\mathrm{s}} = 323$ K (see Fig. 5.8 (a)). Before pulse 1, the sample was heated to the austenitic phase and subsequently cooled to the measurement temperature.

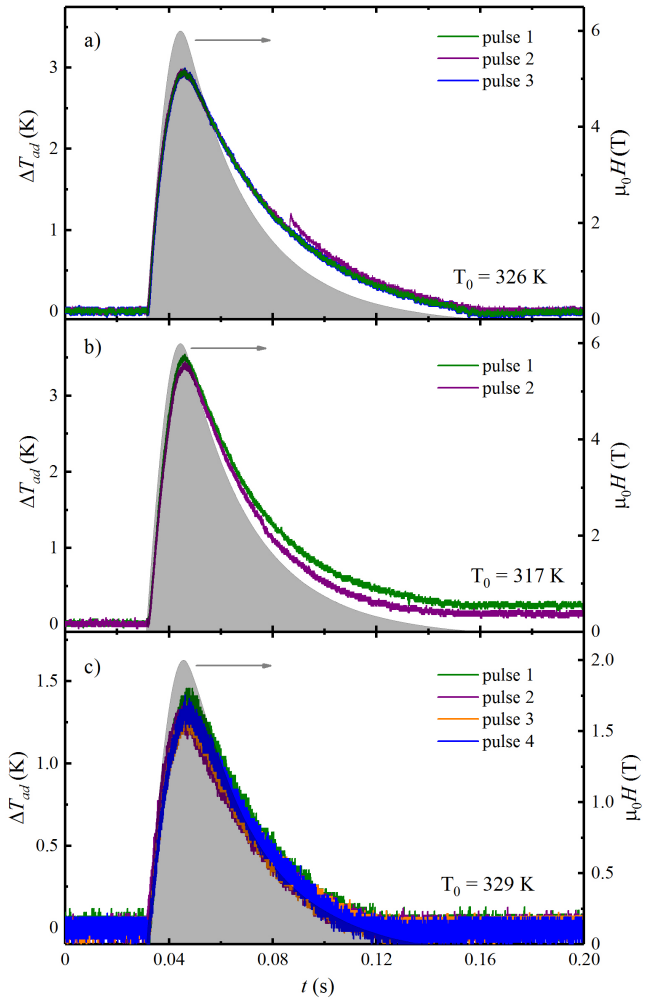

Figure 5.8: *Time dependence of ΔT_{ad} measured at (a) 326 K and (b) 317 K reached upon cooling, for a magnetic-field pulse of 6 T and (c) at 329 K reached upon heating, for a magnetic-field pulse of 2 T. Two, three and four pulses were applied consecutively at 317 K, 326 K and 329 K, respectively. See text for details. The right axes refer to the magnetic field profile.*

Pulse 2 and 3 was followed immediately after pulse 1. After pulse 1 $\Delta T_{\mathrm{ad}}(t)$ exhibits an almost reversible behavior, only a small offset of 0.14 K remains. This value is almost unchanged for pulse 2 and pulse 3. We repeated the previously described experiment after further cooling down to 317 K. This temperature is in between the martensite start ($M_{\mathrm{s}} = 323$ K) and martensite finish ($M_{\mathrm{f}} = 315$ K) temperatures (see Fig. 5.8(b)). After pulse 1 we find only a tiny irreversible offset of 0.26 K. After pulse 2 the offset of 0.13 K is even smaller, while the $\Delta T_{\mathrm{ad}}^{\mathrm{max}}$

for both pulses is almost the same. We note that the recorded offsets are smaller than the uncertainty in the ΔT measurement [99]. Additionally, we investigated the reversibility of the MCE at 329 K ($T > A_s$). Here the measurement temperature was approached upon heating from well below the martensitic transition. At 329 K four consecutive magnetic pulses up to 2 T were applied. As can be seen in Fig.5.8, $\Delta T_{ad}(t)$ is reversible for all pulses. Thus, the previous results are a fair indication of the fast kinetics of the thermoelastic transformation which is reversible due to the small hysteresis. Moreover, the pulsed magnetic fields measurements evidence that $Ni_{2.2}Mn_{0.8}Ga$ exhibits an almost perfect reversible MCE on the time scale of magnetocaloric devices.

5.2.6 Temperature Dependent XRD

To determine the transformation matrix **U** for $Ni_{2.2}Mn_{0.8}Ga$ we conducted PXRD experiments at 350 K in the austenite and at 300 K in the martensite phases. The Le Bail refinement of the PXRD patterns in the austenite and martensite phases are shown in Fig. 5.9. At RT where $Ni_{2.2}Mn_{0.8}Ga$ is in martensitic phase ($M_s = 323$ K, see also Fig. 5.2) all reflections present in the PXRD pattern can be indexed by a body-centered tetragonal structure (space group $I4/mmm$) with refined lattice parameters $a = b = 3.9013$ Å and $c = 6.5129$ Å, while at 350 K $Ni_{2.2}Mn_{0.8}Ga$ is in the austenitic phase in a cubic structure (space group Fm-$3m$). The refined lattice parameter is $a = 5.8286$ Å. A small fraction of martensite phase coexists with the austenite phase at 350 K, which can be attributed to the effect of residual stresses induced martensite phase generated due to grinding the ingot into powder [131, 132]. In our case, for a transformation from the face-centered cubic (Fm-$3m$) to the body-centered tetragonal ($I4/mmm$) structure the lattice parameters of body-centered unit cell can be converted to the face-centered unit cell by the following relationships: $a = a_F = \sqrt{2}a_I$ and $c = c_F = c_I$ where, the index 'I' stands for body-centered [137]. These stretches satisfy $\alpha > 0, \beta > 0$ and $\alpha \neq \beta$ [138]. So, the deformation matrix of one of the corresponding martensite variant from the unit cell

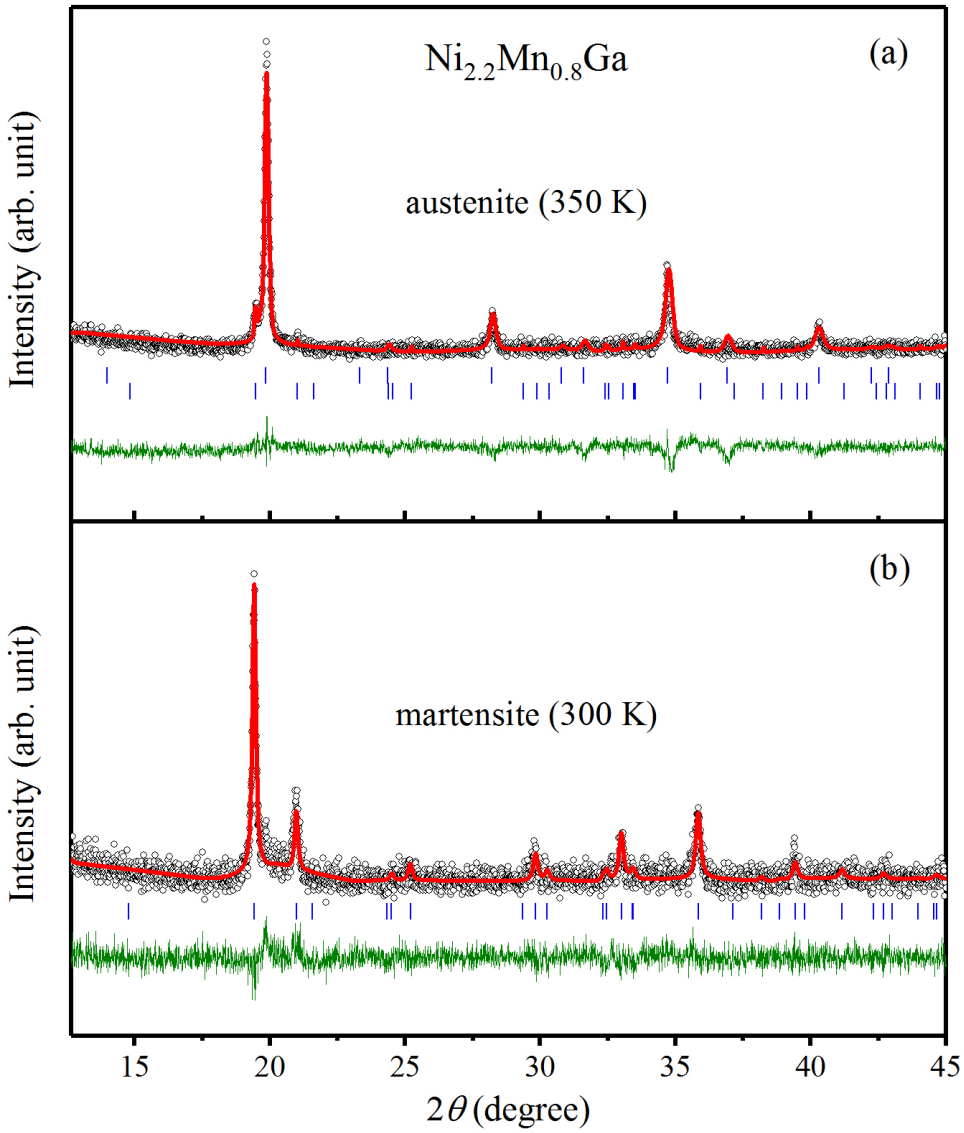

Figure 5.9: *Le Bail refinements for PXRD patterns of $Ni_{2.2}Mn_{0.8}Ga$ in (a) austenite and (b) martensite phases. The experimental data are shown by black circles. The fitted curve and residue are shown by by red and green continuous lines (bottom-most), respectively. The blue ticks represent Bragg-peak positions.*

parameters of $Ni_{2.2}Mn_{0.8}Ga$ turn out to be:

$$\mathbf{U}_1 = \begin{pmatrix} 1.1174 & 0 & 0 \\ 0 & 0.9466 & 0 \\ 0 & 0 & 0.9466 \end{pmatrix}. \tag{5.2}$$

The other two martensite variants $\mathbf{U}_2$ and $\mathbf{U}_3$ follow directly from $\mathbf{U}_1$ according to Eq. 2.15. The determinant of this deformation matrix turns out to be very close to one $|\mathbf{U}| = 1.0012$. The deviation from unity is only 0.12%. This value is found to be substantially smaller in comparison to the previous reported MSM Heusler compounds Mn_2NiGa and $Ni_{2.2}Mn_{0.75}Ga$. These compounds exhibits a large thermal hysteresis of 50 and 14 K, respectively. The value of $|\mathbf{U}|$ for Mn_2NiGa and $Ni_{2.2}Mn_{0.75}Ga$ deviate 0.64% and 0.61% from unity which is more in comparison to our study of $Ni_{2.2}Mn_{0.8}Ga$ MSM Heusler compound [137, 149]. Hence, exemplifying the validity of GCC of austenite and martensite phases in $Ni_{2.2}Mn_{0.8}Ga$.

5.2.7 Summary

We have studied the reversible adiabatic tempertaure change $\Delta T_{\mathrm{ad}}(t)$ in $Ni_{2.2}Mn_{0.8}Ga$ MSM Heusler compound and its relation to the structural properties of cubic austenite and tetrgonal martensite phase. The reversibility of directly measured adiabatic tempertaure change $\Delta T_{\mathrm{ad}}(t)$ in shape memory Heusler compounds is influenced by the hysteresis width as well as the sharpness of magnetostructural transition. In addition to that kinetic arrest which arises from the structural and magnetic inhomogeneous state can also affect this reversibility. The reduction of thermal hysteresis improves lattice coherence and results in faster kinetics of the magnetostructural transformation. Thus, occurrence of small energy barrier at interface leads to reduction of energy required for creating interfaces which in turn attribute the reversible behavior to the highly mobile transition layer between the two phases. We conclude that our finding of geometric compatibility to improve reversibility of MCE in the region of martensitic transformation will provide a new route for designing novel MCE materials with strongly reduced irreversible behavior.

5.3 MCE in $Ni_{1.8}Mn_{1.8}In_{0.4}$

Among the most promising materials, Ni-Mn-In MSM Heusler compounds are attractive candidates for both fundamental research and application point of view [12, 28]. These compounds show various functional properties such as

MSM, magnetic superelasticity, magnetocaloric and barocaloric effect, which originates from magnetoelastic couplings. $Ni_2Mn_{1.4}In_{0.6}$ prototype shape memory compound exhibits a paramagnetic to ferromagnetic transition around 315 K on cooling, followed by a first-order structural transition from high temperature cubic austenite phase to low temperature monoclinic martensite phase around 246 K [12, 29]. $Ni_2Mn_{1.4}In_{0.6}$ exhibits the conventional MCE (increase in sample temperature upon application of magnetic field) around the ferromagnetic transition in the austenite phase. Adiitionally, an inverse MCE (decrease in sample temperature by applying magnetic field) is observed around the first-order martensitic transition leads to decrease in sample temperature with increasing magnetic field [12]. The first-order character of the martensitic transition results in hysteresis losses and fatigue which leads to irreversibility in magnetic refrigeration cycle [111, 143]. Therefore, nowadays, most of the studies have been done on aiming for reducing the hysteresis in MSM Heusler compounds. Hysteresis reduction can be done by the substitution of an additional element or changing the stoichiometry of Ni-Mn-In [39, 132, 152]. Here, we reduce the hysteresis in $Ni_2Mn_{1.4}In_{0.6}$ by changing the stoichiometry of Ni-Mn-In.
Polycrystalline ingot of $Ni_{1.8}Mn_{1.8}In_{0.4}$ was prepared by arc-melting stoichiometric amounts of the constituent elements Ni, Mn and In under Ar atmosphere. The ingot was remelted several times to assure high homogeneity and annealed at 900°C for 3 days and then quenched in ice water mixture. This prepared ingot was used for further measurements.

5.3.1 Scanning Electron Microscopy

Fig. 5.10 shows the SEM image of $Ni_{1.8}Mn_{1.8}In_{0.4}$ at RT. SEM image reveal that the sample is single phase with a homogeneous composition distribution. SEM image has some black dots which represents the unreacted Mn. The composition analysis was done by EDAX which turns out to be $Ni_{1.8}Mn_{1.8}In_{0.4}$ as an average from different parts of the SEM image.

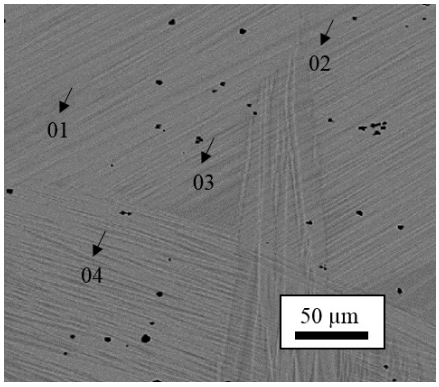

Figure 5.10: *RT SEM image of $Ni_{1.8}Mn_{1.8}In_{0.4}$. The black arrows indicate the areas where the composition was analyzed in detail.*

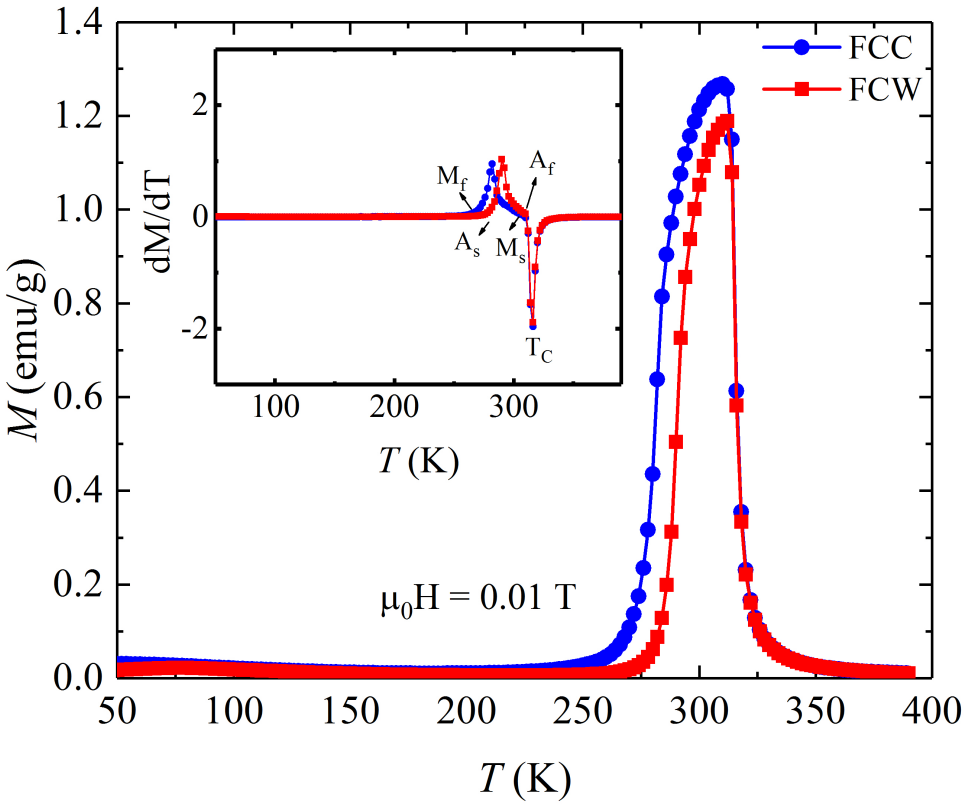

Figure 5.11: *Field cooled cooling (FCC) and Field cooled warming (FCW) magnetization measurements $M(T)$ curves at 0.01 T for $Ni_{1.8}Mn_{1.8}In_{0.4}$. Inset shows the first-order derivative of magnetization with temperature.*

5.3.2 Magnetization Measurements

Fig. 5.11 shows the $M(T)$ curve of $Ni_{1.8}Mn_{1.8}In_{0.4}$ at low magnetic field of 0.01 T for FCC and FCW protocols. On cooling, the material undergoes the direct transformation from martensite to austenite phase, whereas, the reverse transformation from martensite to austenite takes place on heating. Inset in Fig. 5.11 shows the first-order derivative of magnetization with temperature which was used to calculate the characteristic temperatures: austenite start (A_s = 277 K), austenite finish (A_f = 309 K), martensite start (M_s = 307 K) and martensite finish (M_f = 260 K) upon heating and cooling respectively and Curie temperature T_C of 316 K. The calculated thermal hysteresis width from these characteristic temperatures come out to be 9.5 K which is smaller than the reported parent compound $Ni_2Mn_{1.4}In_{0.6}$ from previous studies [12, 29, 142].

A small thermal hysteresis in $Ni_{1.8}Mn_{1.8}In_{0.4}$ motivated us to measure the isothermal magnetic entropy change ΔS_M in static magnetic field. To do this, the temperature dependence of the magnetization, $M(T)$, measured at various magnetic fields upon heating and cooling in the vicinity of the martensitic phase transition is shown in Fig. 5.12. Inset in Fig. 5.12 shows the shift of the martensitic phase transition towards lower temperatures. The magnetic field stabilizes the ferromagnetic austenite phase. The martensitic transition temperature shifts around 2 K as the magnetic field changes from 0.1 to 5 T.
Fig. 5.13 shows the $M(H)$ data for fcc and fcw at three different temperatures, indicating that it is possible to induce the reverse martensitic transition by application of a magnetic field. These $M(H)$ curves show that a magnetic field of 14 T is sufficient to observe a completed transition. Before reaching the target temperature, for each $M(H)$ measurement, the sample was overheated to the austenite phase (350 K) to complete martensite phase (100 K) in zero magnetic field and then heated up to the target temperature. This protocol assure that the sample is always in the fully martensite state, initial state and we can exclude any influence of hysteresis effects on these $M(H)$ curves. At 265 K, the inflexion point in $M(H)$ curve indicates that a critical field of 20 T is sufficient for inducing the martensitic transition from the martensite to the austenite [29]. The sample is transformed back to the martensitic state by removing the mag-

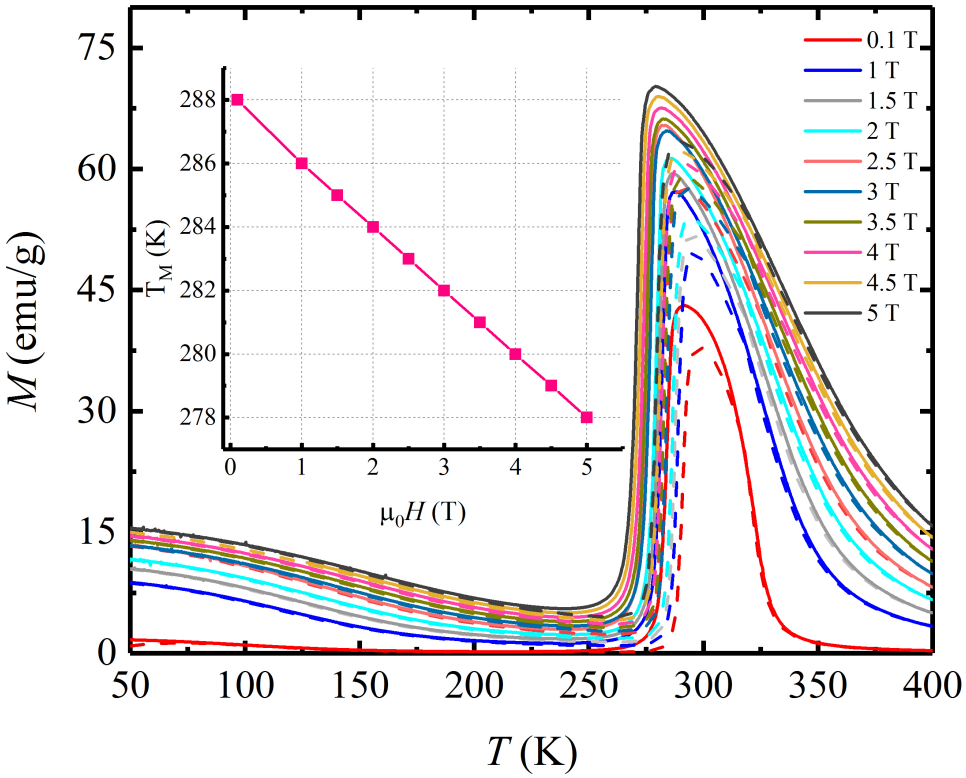

Figure 5.12: *Isotherms $M(T)$ of $Ni_{1.8}Mn_{1.8}In_{0.4}$ at magnetic field of 0.1 to 5 T FCC and FCW are represented by solid and dashed lines respectively. Inset shows the shift of martensitic transition temperature with magnetic field.*

netic field. Note, for temperature close to the austenite transition temperature at T_A, a small part of the sample remains in the austenitic phase after removing the magnetic field. These $M(H)$ curves give a hysteresis of $2-3$ T between critical fields upon increasing and decreasing the magnetic field. The critical field, $H_A(T)$ decreases upon increasing the temperature toward T_A.

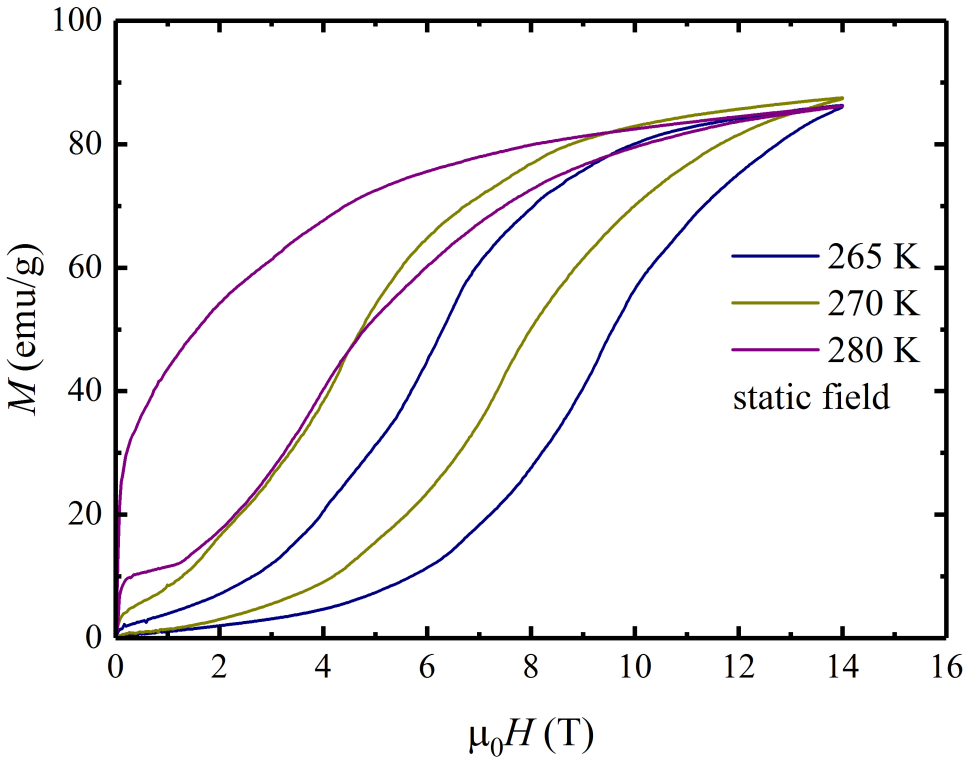

Figure 5.13: *Isotherms $M(H)$ of $Ni_{1.8}Mn_{1.8}In_{0.4}$ at different temperatures for FCC and FCW by applying a static magnetic field of 14 T.*

5.3.3 Isothermal Entropy Change from *M(T)* Measurements

In the next step, the isothermal entropy change ΔS_{M} was calculated from $M(T)$ measurements using the following Maxwell relation [142].

$$\left(\frac{\partial S}{\partial H}\right)_T = \left(\frac{\partial M}{\partial T}\right)_H \tag{5.3}$$

The value of ΔS_{M}, calculated from the $M(T)$ curves, measured upon heating and cooling is found to be almost the same and exhibits a peak around the austenite to martensite transition temperature. Negative value of ΔS_{M}, occurs because of the Curie temperature. The maximum value of ΔS_{M} is exemplified in inset of Fig. 5.14. A smaller thermal hysteresis of 9.5 K and similar value of ΔS_{M} for both heating and cooling in $Ni_{1.8}Mn_{1.8}In_{0.4}$ may show an improved cofactor

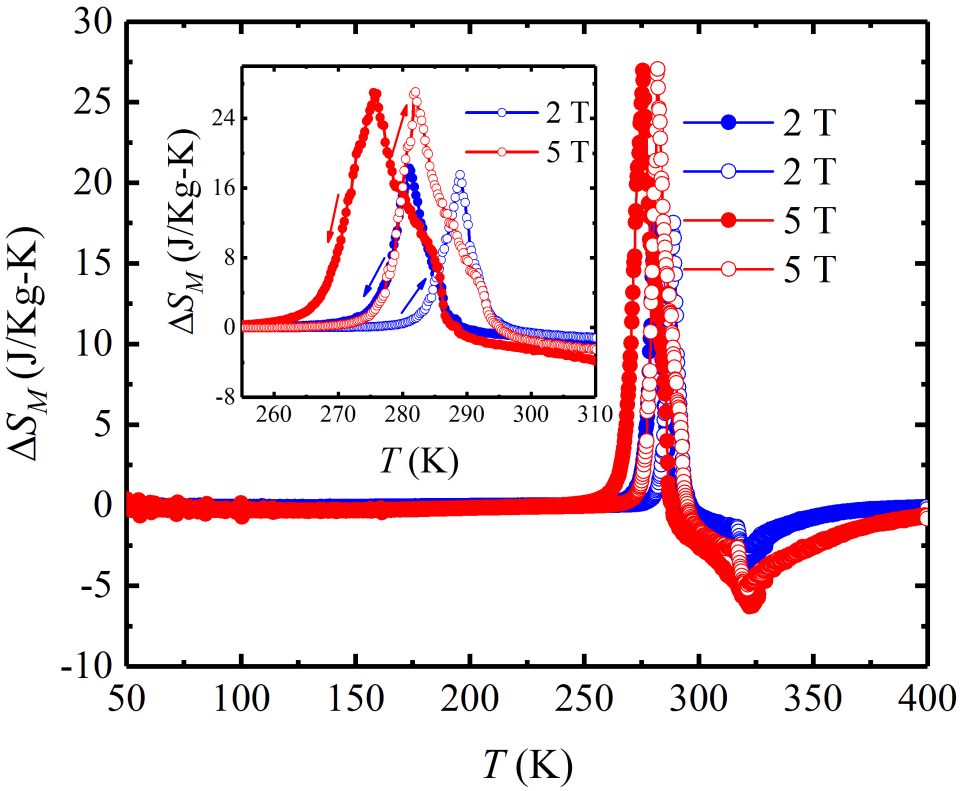

Figure 5.14: *Isothermal magnetic entropy change ΔS_M of $Ni_{1.8}Mn_{1.8}In_{0.4}$ calculated from $M(T)$ curves upon heating (open circles) and cooling (closed circles). Inset shows both heating and cooling curves of ΔS_M on an expanded scale around the martensite transition.*

condition of crystallographic change at martensite phase transition [33, 64].

5.3.4 Temperature Dependent Synchrotron XRD

The austenite phase has cubic structure in Fm-$3m$ space group with cell parameter $a = 6.00482$ Å [see Fig.5.15]. Inset in Fig. 5.15(a) shows the excellent fit for the main peak. At 115 K, The martensite phase has more numbers of Bragg reflections, indicating that the structure is no longer cubic. These reflections cannot be indexed by tetragonal, monoclinic or orthorhombic crystal systems. In the literature, for Ni-Mn based Heusler compounds, these type of complicated diffraction patterns have been reported as modulated structures [55, 132]. Therefore, this diffraction pattern was further analyzed taking into

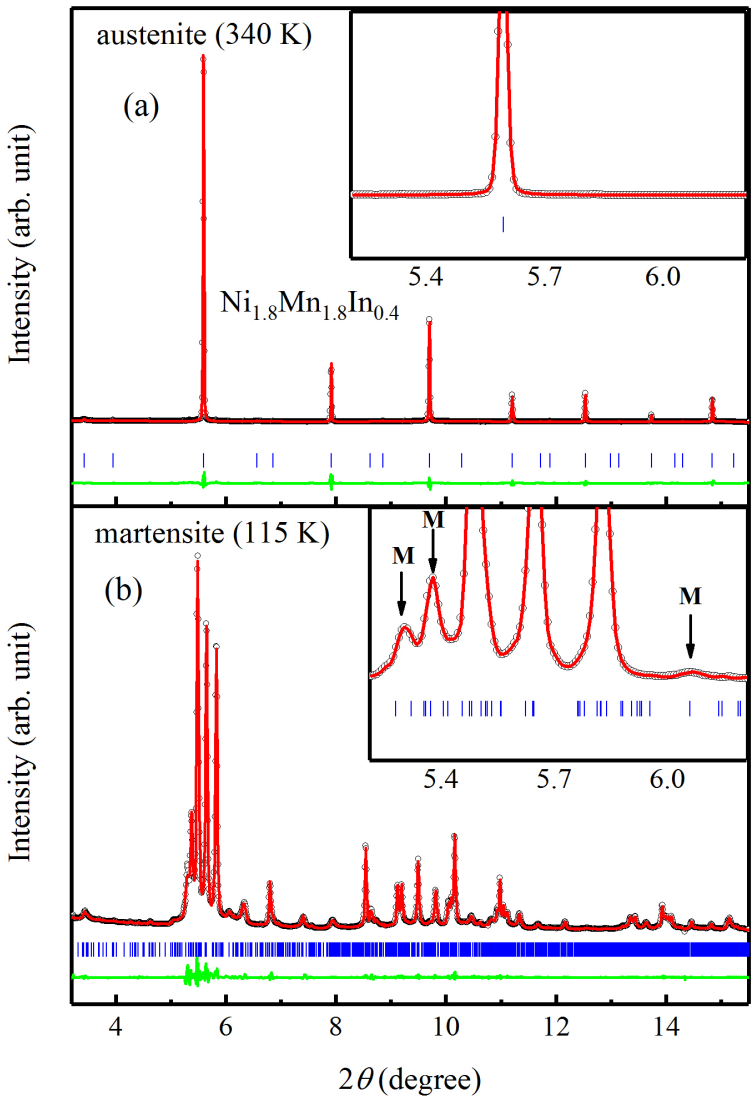

Figure 5.15: *SXRPD in austenite and martensite region for $Ni_{1.8}Mn_{1.8}In_{0.4}$. Inset shows the fit for main peak on an expanded scale. Arrows in (b) represent the satellite reflections in the martensite phase.*

account both main and satellite reflections. A careful analysis of all Bragg reflections present in the martensite phase of $Ni_{1.8}Mn_{1.8}In_{0.4}$ shows that it has a modulated monoclinic structure (S.G. $I2/m$) with refined lattice parameters $a = 4.4299$ Å, $b = 5.5972$ Å, $c = 13.2897$ Å and $\beta = 93.1993°$. The presence of satellite reflections have been shown in inset of Fig. 5.15(b) on expanded scale. The martensite phase has found to be similar to $3M$ modulation reported in our

previous study for $Ni_2Mn_{1.4}In_{0.6}$ [55]. These unit cell parameters of both austenite and martensite phases were used to calculate the transformation matrix **U** for the modulated monoclinic structure. From this transformation matrix **U**, one can obtain all three eigenvalues of the matrix **U**. The middle eigenvalue of the matrix is 1.0006, which is almost close to one ($|\lambda_2 - 1| = 0.0006$) with 0.06% deviation from unity. The deviation of λ_2 value is smaller than the previous reported shape memory compounds [12, 33, 65]. A detailed comparison of thermal hysteresis and middle eigenvalue has been given in the table 5.1. Therefore, it turns out that $Ni_{1.8}Mn_{1.8}In_{0.4}$ follows the cofactor condition for cubic austenite to monoclinic martensite [33, 67].

Table 5.1: *A comparison of the thermal hysteresis and middle eigenvalue for different shape memory compounds [12, 65, 158, 159]*

Compounds	Thermal hysteresis	middle eigenvalue
Ni-Co-Mn-In	12	0.9972
Ni-Ti-Cu	20	0.9986
Ni-Ti-Cu-Pd	11.5	1.0014
Ni-Ti-Au	7	0.9997
Ni-Ti-Pd	12	0.9998

5.3.5 Magnetostriction Measurement in Pulsed Magnetic Field

The magnetostriction measurement was done in 20 T pulsed magnetic field at different temperatures from 260 to 350 K. To avoid the magnetic inhomogeneous state, each measurement was done by heating the sample above the austenite state and then undercooled the martensite state before reaching the target temperature T_i. The relative length change is calculated from the following formula:

$$\frac{\Delta l}{l_0} = \frac{l - l_0}{l_0} \tag{5.4}$$

Where, l_0 is the initial length before the pulse applies [154]. The relative length change as a function of magnetic field at different temperatures are shown in Fig. 5.16. At 350 K, the sample is in fully austenite phase and there is no

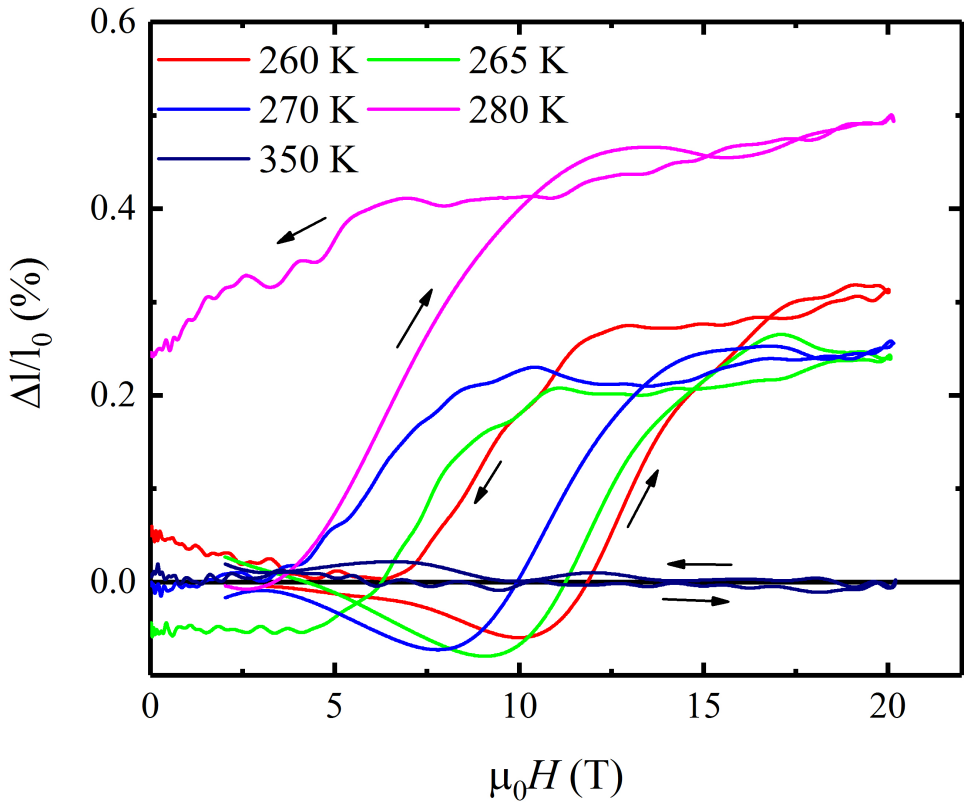

Figure 5.16: *The relative length change of of $Ni_{1.8}Mn_{1.8}In_{0.4}$ as a function of magnetic field at different temperatures.*

significant change in sample length by applying the magnetic field. At lower temperatures (250, 260 and 270 K) below A_s, magnetic field induces the transition from martensite to austenite. Initially, the sample compresses and then expands to a relative length change of 0.3%. The cubic structure of austenite phase possesses a larger volume than the monoclinic martensite structure. This effect is reversible and a larger value is obtained in comparison to the other Ni-Mn based MSM Heusler compounds [120, 154, 156]. This initial compression occurs because of the re-orientation of martensite variant as a preparation to the structural transition. At A_s <280 K, some austenite is always present in the sample, which can be clearly seen in the $M(H)$ curve. This amount of austenite phase prohibits the initial compression and a relatively larger change of sample length is obtained. As we go to the lower temperature ($T_i < M_f$), around 280 K, magnetic field induces the transition but after removing the magnetic

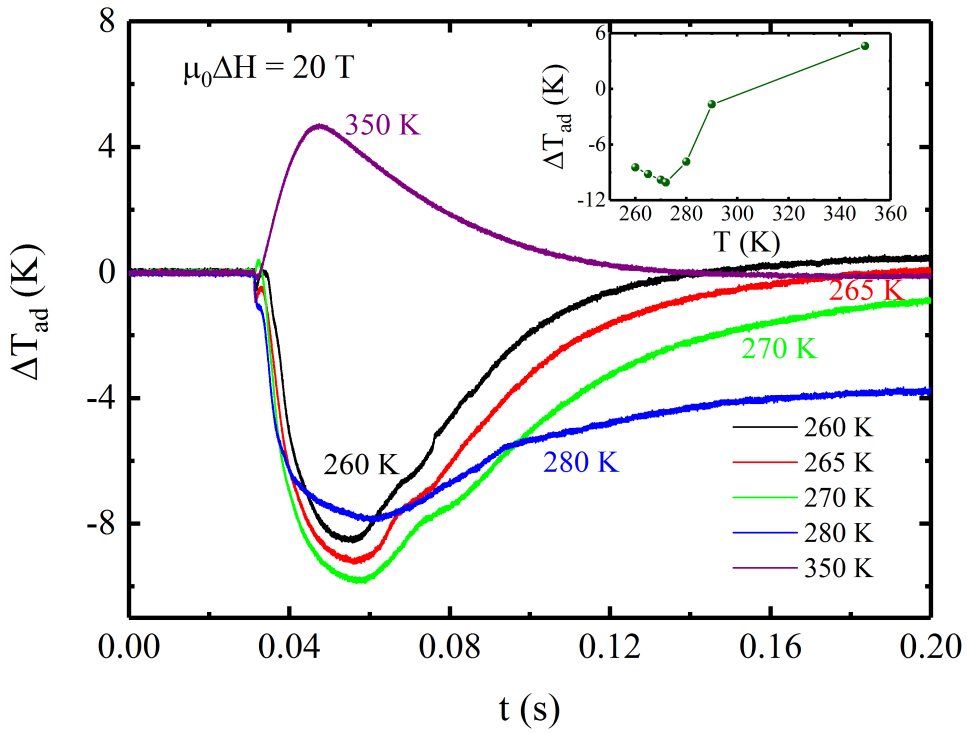

Figure 5.17: *The time dependence of ΔT_{ad} measured at different sample temperatures for a magnetic-field pulse of 20 T. Inset shows the variation of maximum value of adiabatic temperature change for $Ni_{1.8}Mn_{1.8}In_{0.4}$ measured in 20 T pulsed magnetic fields. Each measurement was preceded by heating up the sample to the fully austenitic phase and then cooling down to the completely martensitic phase before approaching the measurement temperature.*

field, the sample does not transform back to the complete martensitic phase and a remanent expansion value of around 0.2% is observed.

5.3.6 Adiabatic Temperature Change in Pulsed Magnetic Field

Direct adiabatic temperature change was measured near real operational conditions in pulsed magnetic fields up to 20 T, which provide us a comprehensive access to the dynamic MCE and the high-field properties of materials with first- and second-order phase transitions. As expected, a conventional MCE was observed around the Curie temperature in the austenitic phase (see the data at

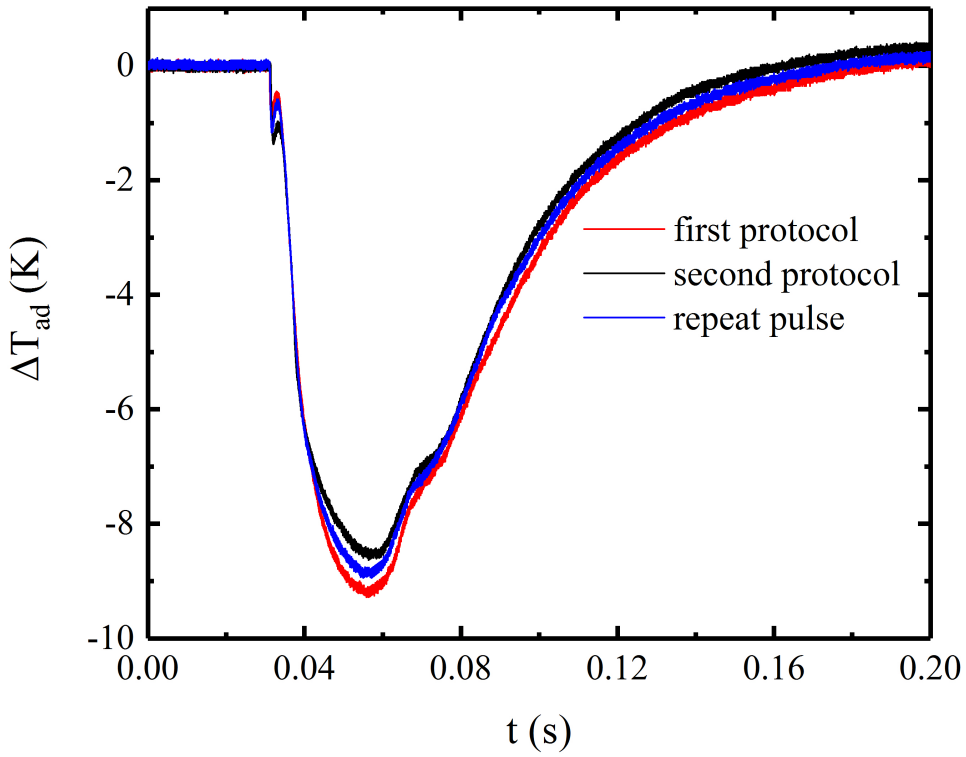

Figure 5.18: *Time dependence of ΔT_{ad} measured at 265 K for $Ni_{1.8}Mn_{1.8}In_{0.4}$ by applying a magnetic field of 20 T at three different pulses.*

350 K in Fig. 5.17). After removing the magnetic field (down sweep) the sample reaches again the initial temperature, which is a strong proof of reversible MCE. However, for temperatures below the martensitic transition, the initial state cannot be reached when the magnetic field is removed and the sample ends up in a mixed state which is magnetically different from the initial one. Consequently, the observed ΔT_{ad} is reduced as can be seen clearly at 270 and 280 K. The observed irreversibility for temperatures below the martensitic transition has been widely studied as a unavoidable character of every first-order transition. But the outstanding spot in these measurements is the reversible behavior of ΔT_{ad} at 260 and 265 K in the lower part of hysteresis region. Obviously (see Fig. 5.11) these temperatures sit within the hysteretic region. Yet ΔT_{ad} at these two temperatures are completely reproducible like in case of 350 K. Inset in Fig. 5.17 shows the variation of ΔT_{ad} with magnetic field. The maximum value of ΔT_{ad} is $\approx$ 10 K at 265 and 270 K sample temperature.

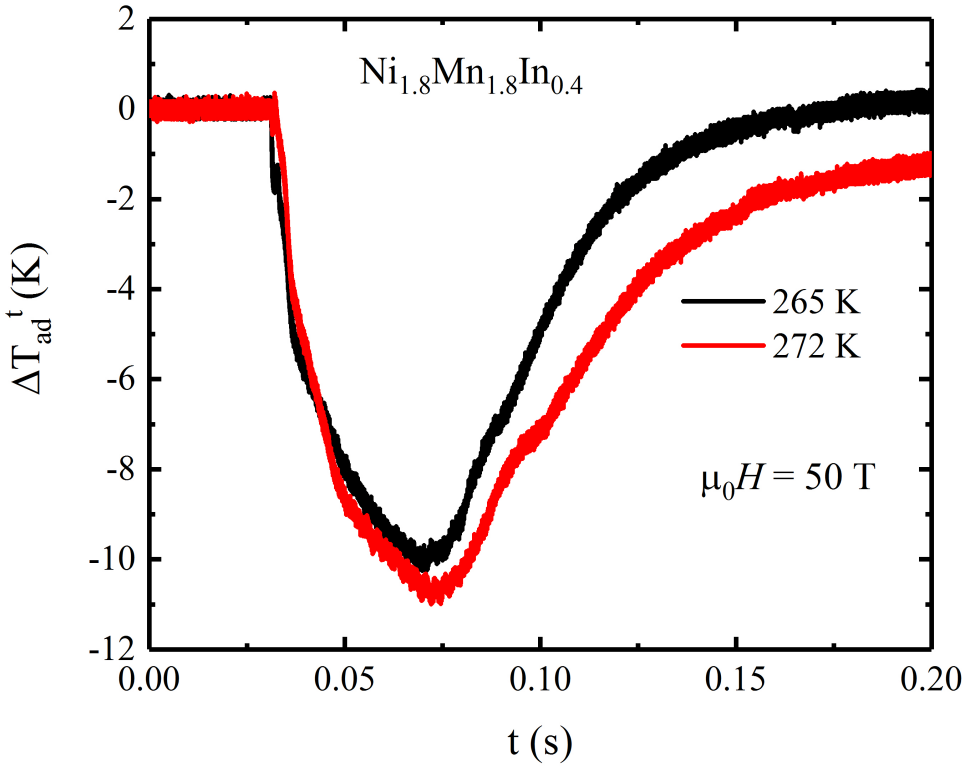

Figure 5.19: *The time dependence of ΔT_{ad} measured at 265 and 272 K of $Ni_{1.8}Mn_{1.8}In_{0.4}$ by applying a magnetic field of 50 T.*

Fig. 5.18 shows the obtained ΔT_{ad} as a function of time at $T_{\mathrm{i}} = 265$ K for a 20 T magnetic field pulse. This temperature sits within the hysteretic region. However, ΔT_{ad} is completely reproducible like in case of 350 K. Just to be sure we double-checked it by measuring ΔT_{ad} in two subsequent magnetic field sweeps for 265 K. According to our data MCE is completely reversible as it comes back to the starting temperature after removing the magnetic field. Moreover, a 50 T pulse was applied to measure the adiabatic temperature change in $Ni_{1.8}Mn_{1.8}In_{0.4}$. The maximum value of ΔT_{ad} at 50 T pulse is $\approx$10 K. This value of ΔT_{ad} is same as 20 T pulse, which confirms that 20 T magnetic field was sufficient to induce the reverse martensitic transition from martensite to austenite.

5.3.7 Summary

A strategy for reducing hysteresis at the martensite phase transition is suggested by using crystallographic theory of martensite and successively applied using compositional variation in non magnetic materials showing martensite transformation [33]. This strategy has been applied to $Ni_{1.8}Mn_{1.8}In_{0.4}$ MSM Heusler compound which gives a very small value of thermal hysteresis ≈ 9.5 K in comparison to other MSM Heusler compounds [12, 29, 142, 143]. The reduction of thermal hysteresis results in same value of ΔS_{M} for FCC and FCW. Similar value of ΔS_{M} indicates the improved cofactor condition ($\lambda_2 = 1$) which is found very close to unity (1.0006) and deviates only 0.06%. Following this, field induced magnetostriction and adiabatic temperature change was measured in pulsed magnetic field. The relative length change of around 0.3% was observed at three different temperatures 260, 265 and 270 K. The reversible adiabatic temperature change ΔT_{ad} of -10 K was observed in the lower part of hysteresis region at 265 K by applying a magnetic field of 20 T. It was confirmed by applying three pulses. Furthermore, ΔT_{ad} of -10 K was observed by applying a pulse of 50 T, confirms that 20 T was high enough to induce the reverse martensitic transition.

6 Minimizing hysteresis in $Ni_{2+x}Mn_{1-x}Z$(Z= In) Heusler compounds

This chapter gives a detailed analysis of minimizing hysteresis under hydrostatic pressure in Ni-Mn based MSM Heusler compounds. Large MCE in MSM Heusler compounds put them forward as efficient materials for magnetic refrigeration. However, irreversibility due to the hysteresis of first-order phase transition made them challenging for the magnetic refrigeration. Therefore, minimizing hysteresis is essential in order to improve the reversibility with successive magnetic field cycle. Under the application of hydrostatic pressure, sample composition remains unaffected without altering the change in electron count and structural disorder. Hydrostatic pressure reduces thermal hysteresis by approaching the GCC (explained in chapter 2) for phase transforming MSM Heusler compounds.

6.1 Influence of Pressure

The MCE can be influenced by chemical (substitution of interstitial element) as well as physical (hydrostatic) pressure [12, 112]. The substitution or doping of interstitial elements change the interatomic distance as well as magnetic interaction. Chemical pressure tunes the magnetic and crystallographic phase transition temperatures, which can affect the MCE. It can also be used to coincide both magnetic and crystallographic transition temperature, giving rise to coupled first-order transition temperature. An example of both effect can be seen in Mn-Co-Ge compounds [160]. Thus, chemical pressure is an invaluable tool to tune as well as to create magnetoelastic and magnetostructural coupling

[112].

Another way to affect the MCE is the use of physical pressure by changing interatomic distance and magnetocrystalline coupling [81, 161]. Unlike its chemical counterpart, physical pressure retains the composition, purity and shape of sample without suffering from the parasitic effects which originates in the substitution [12, 28]. The hydrostatic pressure effect was studied on $Ni_{45.7}Co_{4.2}Mn_{36.6}In_{13.5}$ MSM Heusler compound. The magnetization measurement of $Ni_{45.7}Co_{4.2}Mn_{36.6}In_{13.5}$ shows that the martensitic transition shifted to higher temperature in the presence of hydrostatic pressure [28]. Gottschall *et al.* [28] had focused only to bring the martensitic transition near RT. In the thesis, the attention was paid to reduce the hysteresis under hydrostatic pressure for improving the reversibility of MCE.

6.2 Sample Preparation and Initial Characterization

Polycrystalline ingots of composition $Ni_2Mn_{1.4}In_{0.6}$ and $Ni_{1.8}Co_{0.2}Mn_{1.4}In_{0.6}$ were prepared from high purity elements of Ni, Co, Mn and In with 3% excess of Mn by arc melting (repeated several times after flipping the button to ensure homogeneity) and subsequent annealing in a quartz ampoule under Ar atmosphere and quenched in an ice water mixture. The annealing temperature and time were 973 K for 72 hours and 1173 K for 24 hours for $Ni_2Mn_{1.4}In_{0.6}$ and $Ni_{1.8}Co_{0.2}Mn_{1.4}In_{0.6}$, respectively and initially characterized by SEM. Both samples are single phase. The final composition turns out to be same as initial composition in both samples from EDAX measurement.

6.3 Pressure Dependent Magnetization of $Ni_2Mn_{1.4}In_{0.6}$

At atmospheric pressure, $Ni_2Mn_{1.4}In_{0.6}$ show the martensitic transition T_M = 272 K from austenite to martensite during cooling while the reverse transition, occurs at T_A = 283 K from martensite to auustenite and gives a thermal hys-

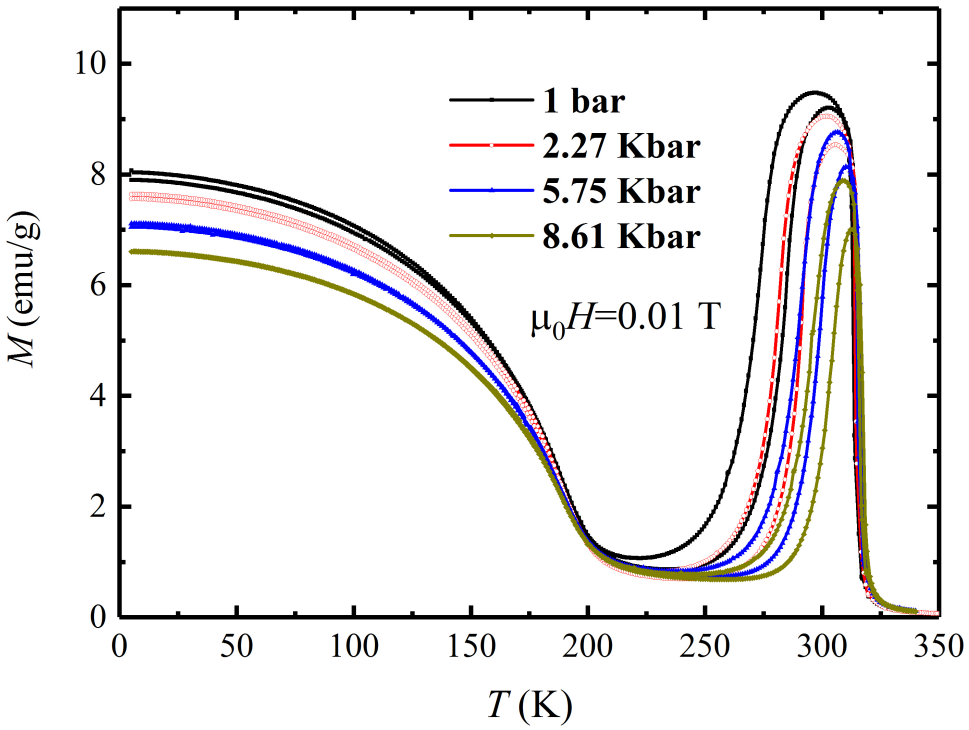

Figure 6.1: *Field cooled heating and cooling magnetization measurements by applying a magnetic field of 0.01 T for $Ni_2Mn_{1.4}In_{0.6}$ at different pressures.*

teresis of approximately 11 K because of the first-order nature of martensitic transition as shown in Fig. 6.1. Hydrostatic pressure stabilizes the antiferromagnetic martensite phase and shifts T_M to a higher temperature of 2.8 K/kbar. These values agrees well on similar compositions, reported in literature [96, 153]. The application of hydrostatic pressure decreases the hysteresis linearly to about 34% (7.3 K for P = 9 kbar) from its original value (11 K at P = 0 kbar) with a rate of 0.46 K/kbar with increasing pressure (see Fig. 6.2). Curie temperature T_C is also found to shift towards to higher temperatures with increasing pressure but with a slower rate of 0.24 K/kbar of the martensitic tranistion, in an excellent agreement with the literature [156]. If the shift of the transition temperatures (T_M and T_A) for both the martensite and ferromagnetic to paramagnetic austenite transitions may continue as the same bove 10 kbar with increasing pressure, then we estimate that the two transitions should merge at around 15 kbar for this compound and this hysteresis should vanish at approximately 24 kbar [155]. Fig. 6.2 shows the variation of thermal hysteresis with

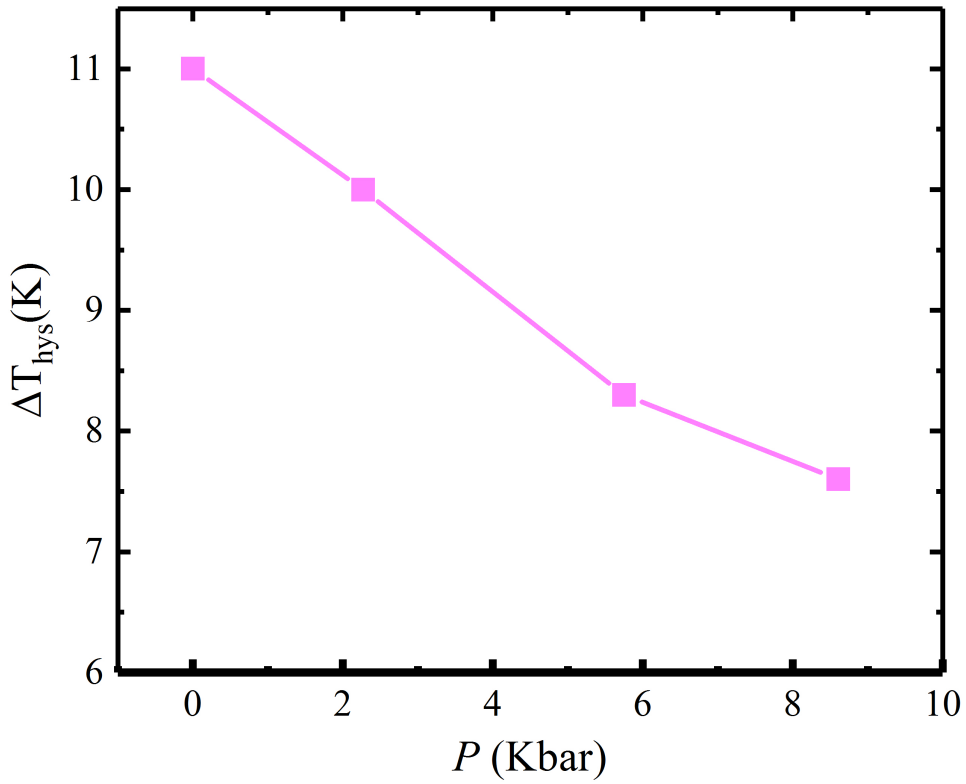

Figure 6.2: *Thermal hysteresis of magnetostructural martensitic phase transition as a function of pressure for* $Ni_2Mn_{1.4}In_{0.6}$.

pressure which is almost linearly decreases as pressure increases. The decrease in thermal hysteresis with pressure suggests that the austenite martensite phase compatibility is enhanced under hydrostatic pressure [66, 153].

6.4 Pressure Dependent XRD of $Ni_2Mn_{1.4}In_{0.6}$

To study the GCC, XRD was done under hydrostatic pressure in both austenite and martensite phase. Prior to XRD, $Ni_2Mn_{1.4}In_{0.6}$ ingot was grounded into powder and annealed at 973 K for 10 hours followed by quenching into ice water mixture to remove residual stress. The annealed powder was sieved under 10 μm in particle size. Fig. 6.3 shows the XRD pattern in austenite phase at 320 K for 4 different pressures. The experimental condition about XRD is described in chapter 3. The structure is cubic in austenite phase and can

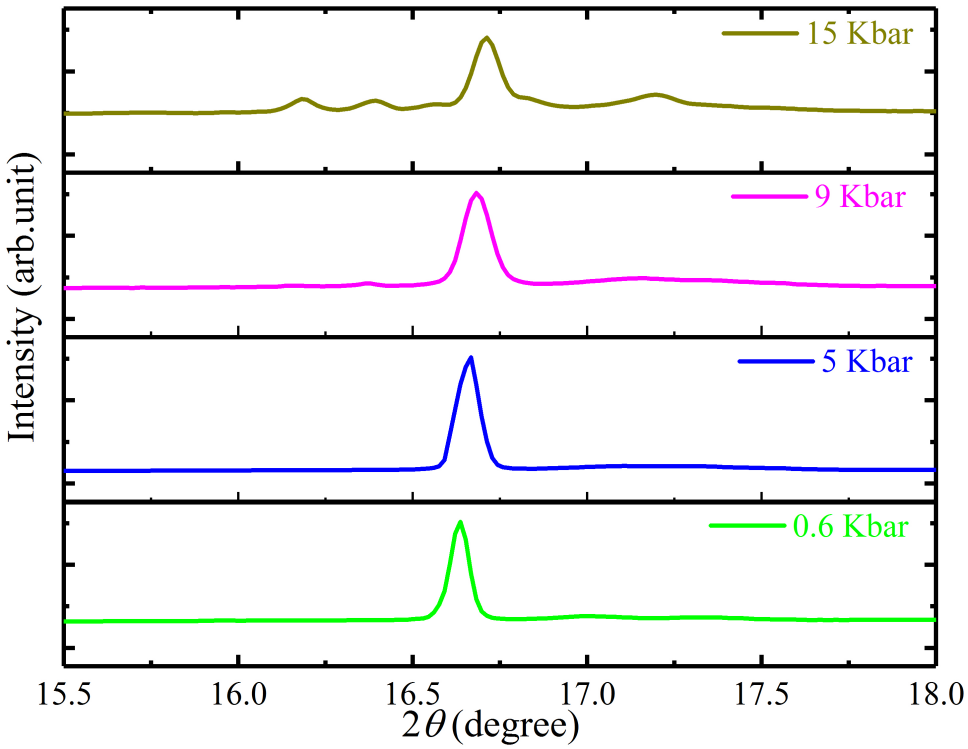

Figure 6.3: *Pressure dependent XRD in austenite phase at 320 K for* $Ni_2Mn_{1.4}In_{0.6}$.

be successfully refined with $L2_1$ (space group Fm-$3m$) cubic structure. Thus, these XRD patterns confirms that the cubic structure is not affected with the hydrostatic pressure and remains all over the same with and without pressure [53, 55]. XRD patterns were also taken in martensite phase at 240 K with the same pressure values as in the austenite phase. At 240 K, more number of Bragg reflections appear which indicates that the structure is no longer cubic and can be succesfully refine with $3M$ modulated structure [55]. Fig. 6.4 shows the modulated structure in the martensite phase for $Ni_2Mn_{1.4}In_{0.6}$. At 0.6 kbar there is a peak from sample holder indicated by red star which becomes invisible at high pressure value. Le Bail refinement was done to calculate the lattice parameter of both austenite and martensite phase. Fig. 6.5 and 6.6 shows the variation of lattice parameters, volume and monoclinic angle with pressure. The lattice parameters of monoclinic phase a_m and c_m were normalized for comarison with cubic phase and decreases with pressure. Similarly, the volume of cubic

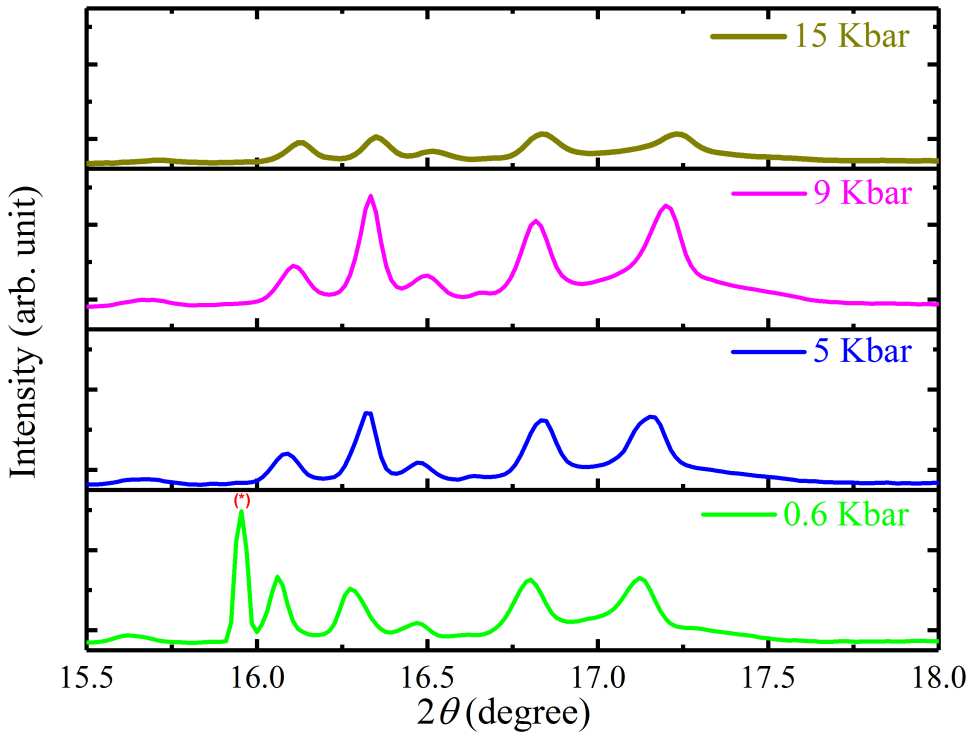

Figure 6.4: *XRD for $Ni_2Mn_{1.4}In_{0.6}$ in martensite phase at 240 K for different pressures. Red star represents the peak due to sample holder.*

and monoclinic phase also decreases with pressure while the monoclinic angle β is found to be nonlinear upon the increase of the applied pressure.

The GCC for monoclinic martensite structure is quantified by the middle eigenvalue λ_2 of the transformation stretch matrix **U** which is obtained from the lattice parameter of both austenite and martensite phase. Fig. 6.7 shows the middle eigenvalue variation at different pressure. It shows the similar trend as the thermal hysteresis and approaches increasingly closer to 1 with increasing pressure. These results confirm that decrease in thermal hysteresis results from the improved GCC between austenite and martensite phase.

The effect of hydrostatic pressure was studied not only on the thermal hysteresis but also on the latent heat of the transition because of the energy barrier itself as reported by Zhang *et al.* [66] in composition tuned λ_2 study. The clausius clapeyron equation was used to calculate the latent heat of the structural

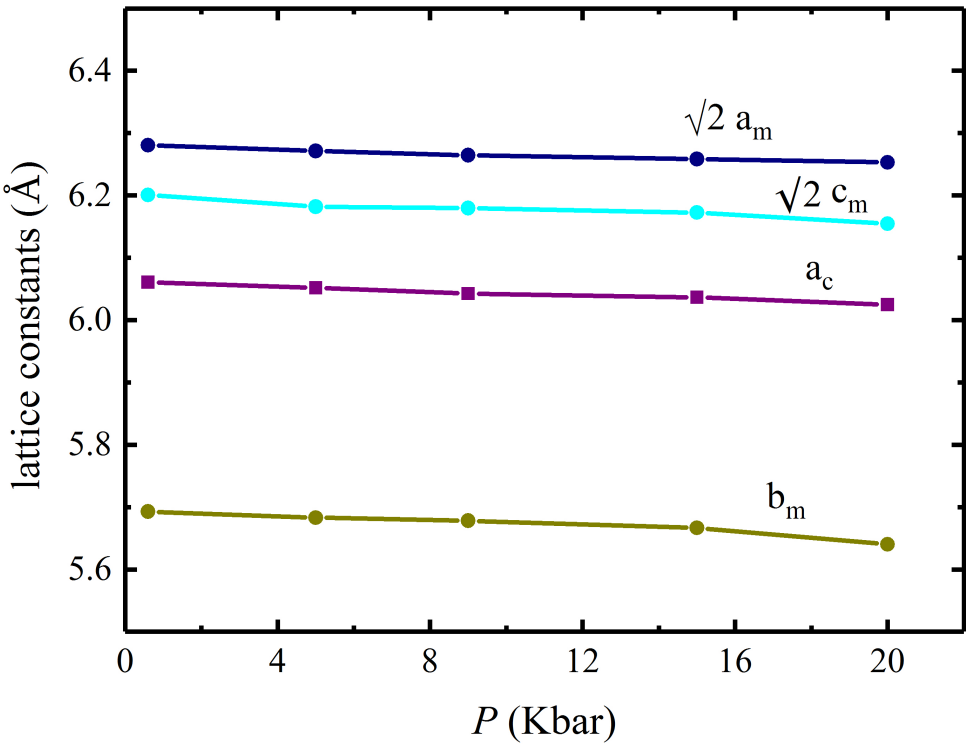

Figure 6.5: *Lattice parameter variation of $Ni_2Mn_{1.4}In_{0.6}$ for cubic and monoclinic structure as a function of pressure.*

martensitic transformation [155]:

$$\frac{\rho(\Delta V/V)}{\Delta S_t} = \left(\frac{\partial T_t}{\partial P}\right)_H \tag{6.1}$$

Where, ΔS_t : Entroy change due to the structural phase transition in the absence of field,

$\Delta V/V$: Relative volume change at the phase transition,

$\frac{\partial T_t}{\partial P}$: Shift of the phase transition with pressure at a given field, and

ρ : Density of the material.

The density of material for $Ni_2Mn_{1.4}In_{0.6}$ is given by $\rho = 8.231\times\ 10^3\ \frac{Kg}{m^3}$. By using equation 6.1, one can calculate ΔS_t. Since, $\Delta S_t = \frac{L}{T_t}$, where L is the latent heat and T_t is transition temperature. Thus, latent heat can be calculated from the high pressure XRD and magnetization data. Since, both cooling and heating transitions shift at different rates with pressure, and thus have different

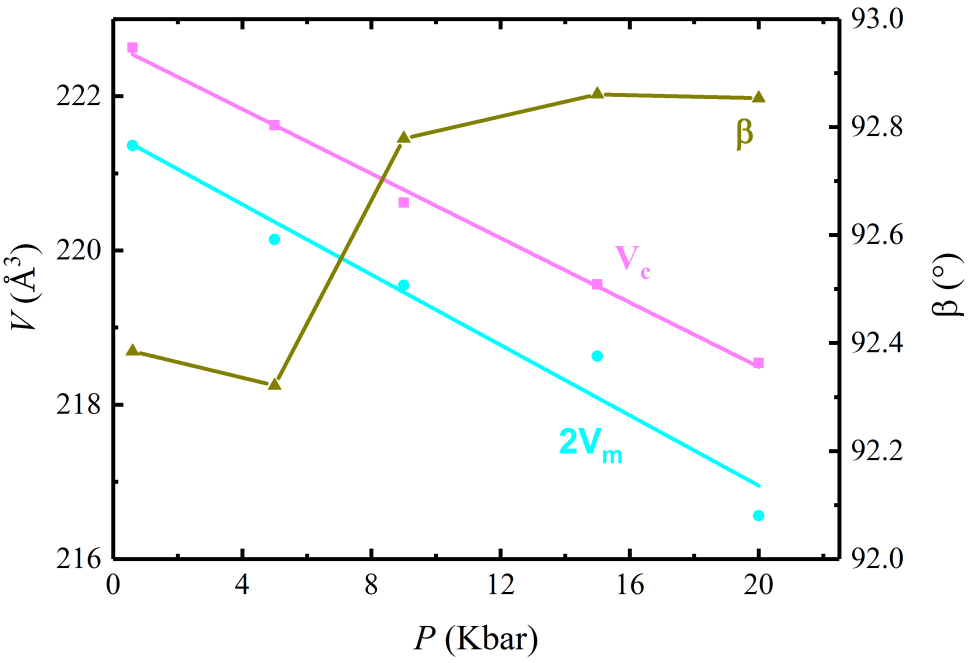

Figure 6.6: *Volume and monoclinic angle of $Ni_2Mn_{1.4}In_{0.6}$ as a function of pressure.*

transition temperatures T_t. It reflects a different energy barriers and latent heat at the transition depending on the direction it is crossed. As, the transition temperature T_t is different at different pressure for heating and cooling transitions. So, two sets of latent heat (cooling and heating) are obtained which decreases with increasing pressure. It indicates that the energy barrier between austenite and martensite phase is decreased.

The enhanced compatibility between austenite and martensite phase under hydrostatic pressure can also be understood from the isothermal compressibility of the individual phases from structural point of view. The isothermal compressibility (β) calculates from the structural parameter of both austenite and martensite phase and turns out to be $\beta_{aus} = 1.003 \times 10^{-3}$ Kbar^{-1} and $\beta_{mar} = 0.957 \times 10^{-3}$ Kbar^{-1}, respectively. A slightly larger value of β for austenite phase indicates that the austenite phase is more compressible in compare to the martensite phase. It makes the lattice parameter mismatch smaller and both phases more compatible with increasing pressure by bringing λ_2 closer to unity.

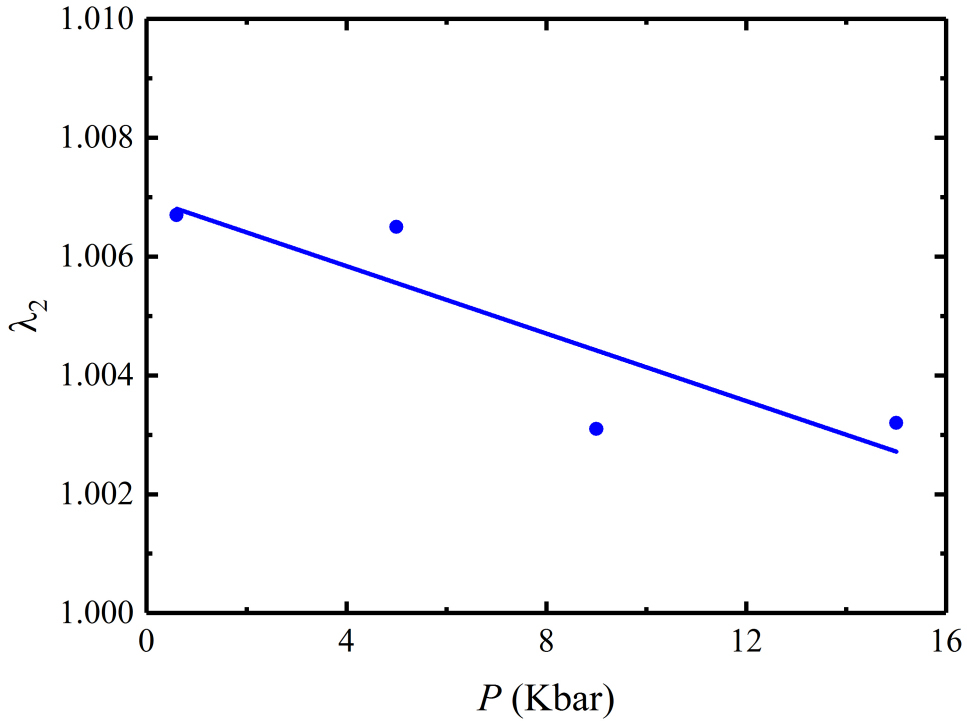

Figure 6.7: *middle eigenvalue for* $Ni_2Mn_{1.4}In_{0.6}$ *as a function of pressure.*

6.5 Generalization of Hydrostatic Pressure

Hydrostatic pressure reduces the thermal hysteresis, which is essential in order to achieve MSM and consequently, a reversible MCE. The lower thermal hysteresis and latent heat of first-order phase transition makes the MCE more reversible and consequently, lower energy cost and more efficient for perspective applications. It can be elaborated as in case of magnetic refrigeration based on MCE, the refrigeration capacity (amount of heat that can be extracted) is given by the area below the entropy change vs. temperature curve. However, using a material which shows the first- order phase transition in a refrigeration cycle, it can be quantified as the area of the overlap between the entropy change vs. temperature curves measured on heating/cooling or application/removal of the magnetic field, which are separated by thermal/field hysteresis [157]. Thus, minimizing thermal hysteresis creates a larger overlap and so that maximize the refrigeration capacity in this compound.

In order to check that the phase compatibility under hydrostatic pressure is

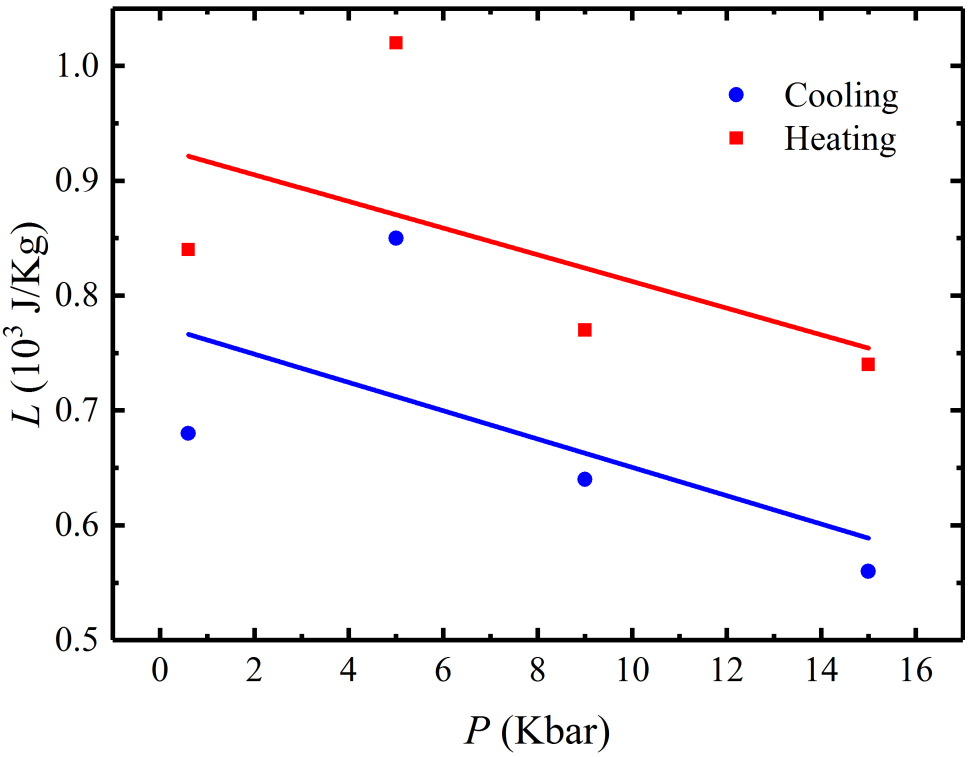

Figure 6.8: *Latent heat during heating and cooling of* $Ni_2Mn_{1.4}In_{0.6}$ *with pressure.*

valid only for $Ni_2Mn_{1.4}In_{0.6}$ or applicable to all Ni-Mn based MSM Heusler compounds. The magnetization under hydrostatic pressure was measured for other compound $Ni_{1.8}Co_{0.2}Mn_{1.4}In_{0.6}$. Similar to $Ni_2Mn_{1.4}In_{0.6}$, $Ni_{1.8}Co_{0.2}Mn_{1.4}In_{0.6}$ also shows martensitic phase transition from cubic austenite to modulated monoclinic martensite with an approximate thermal hysteresis of 28 K. The GCC for $Ni_{1.8}Co_{0.2}Mn_{1.4}In_{0.6}$ was calculated from NPD.

6.6 Pressure Dependent Magnetization of $Ni_{1.8}Co_{0.2}Mn_{1.4}In_{0.6}$

$Ni_{1.8}Co_{0.2}Mn_{1.4}In_{0.6}$ shows the first-order phase transition at 200 K from ferromagnetic cubic austenite to antiferromagnetic $3M$ modulated monoclinic martensite structure with an approximate thermal hysteresis of 28 K. The mag-

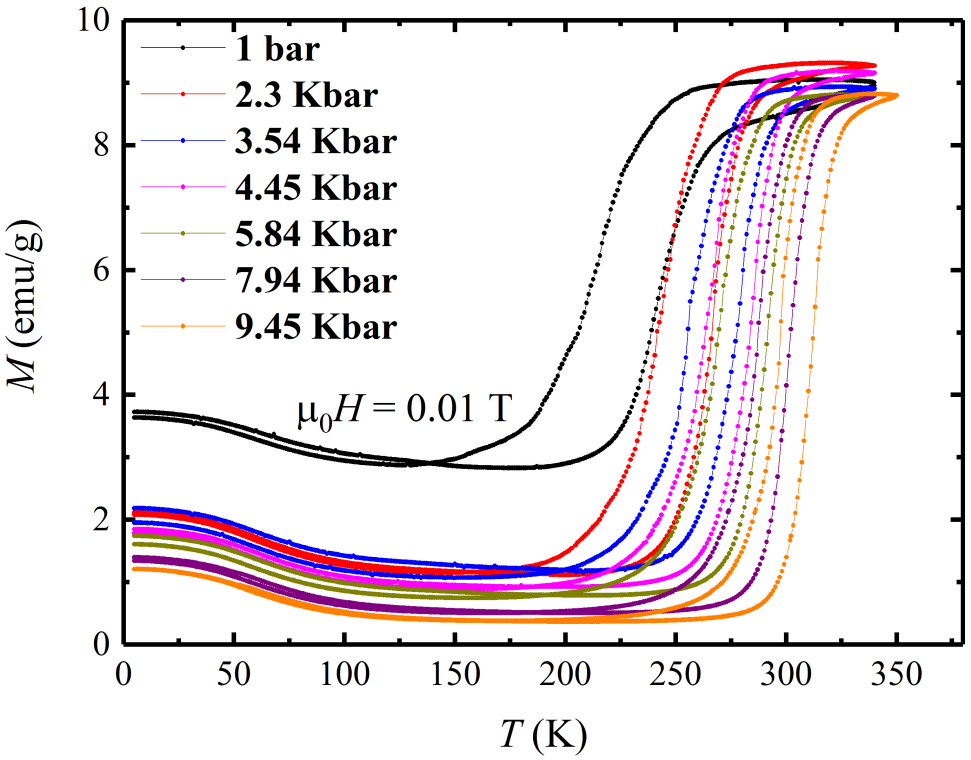

Figure 6.9: *Field cooled heating and cooling magnetization measurements by applying a magnetic field of 0.01 T for $Ni_{1.8}Co_{0.2}Mn_{1.4}In_{0.6}$ at different pressures.*

netization (FCC and FCW) measurements were done on $Ni_{1.8}Co_{0.2}Mn_{1.4}In_{0.6}$ by applying a magnetic field of 0.01 T at different pressures as shown in Fig. 6.9. Fig. 6.10 shows the variation of thermal hysteresis with pressure for $Ni_{1.8}Co_{0.2}Mn_{1.4}In_{0.6}$. Thermal hysteresis decreases as the pressure increases. However, the decrease in thermal hysteresis was non linear.

6.7 Neutron Powder Diffraction of $Ni_{1.8}Co_{0.2}Mn_{1.4}In_{0.6}$

Fig. 6.11 shows the NPD pattern for $Ni_{1.8}Co_{0.2}Mn_{1.4}In_{0.6}$ in the austenite (300 K) and martensite (2 K) phase. NPD was collected at the D2B high-resolution neutron powder diffractometer (ILL, Grenoble). The data was taken

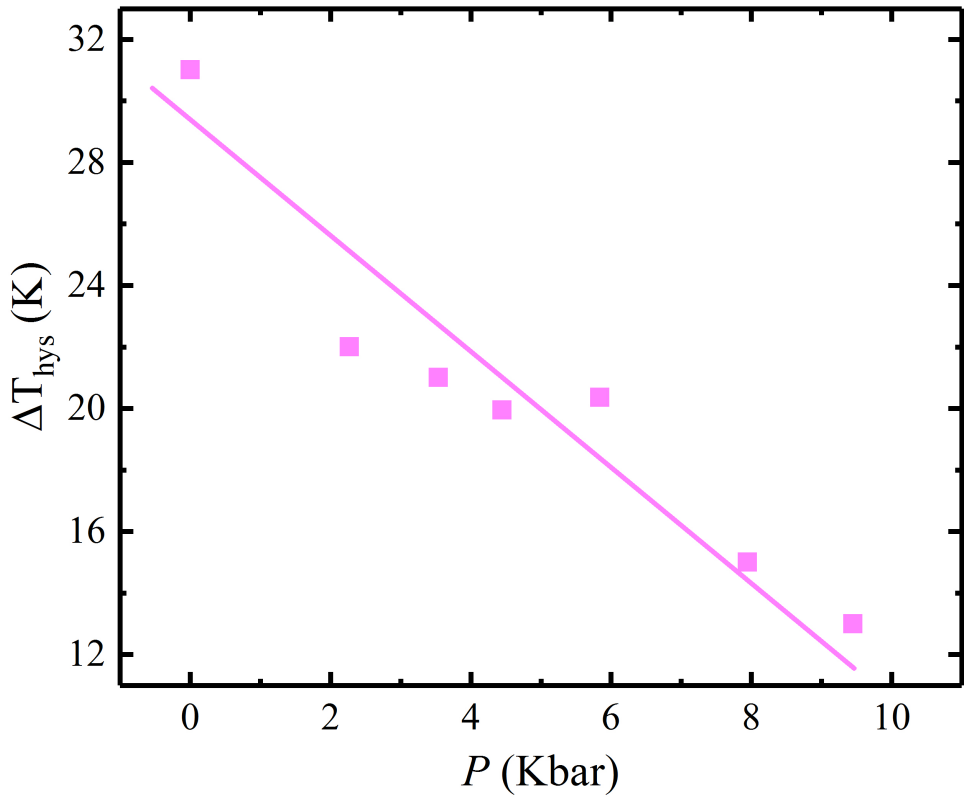

Figure 6.10: *Thermal hysteresis of magnetostructural martensitic phase transition as a function of pressure for* $Ni_{1.8}Co_{0.2}Mn_{1.4}In_{0.6}$.

on powder sample by using a neutron wavelength of 1.59 Å in the high-intensity mode. The powder sample was loaded in a vanadium cylindrical sample holder. The lattice parameters of the powder diffraction patterns were calculated from Le Bail refinement using the JANA2006 software package [58]. The obtained lattice parameters are $a = 5.9893$ Å at 300 K in the austenite phase and $a = 4.4022$, $b = 5.5407$, $c = 4.3216$ and $\beta = 94.2410°$ at 2 K in monoclinic martensite phase. The deformation matrix 2.18 is calculated from these lattice parameters. Following this, the middle eigenvalue λ_2 of the transformation comes out to be 0.9899, which is very close to 1. Thus, $Ni_{1.8}Co_{0.2}Mn_{1.4}In_{0.6}$ satisfy the GCC for cubic austenite to monoclinic martensite structure.

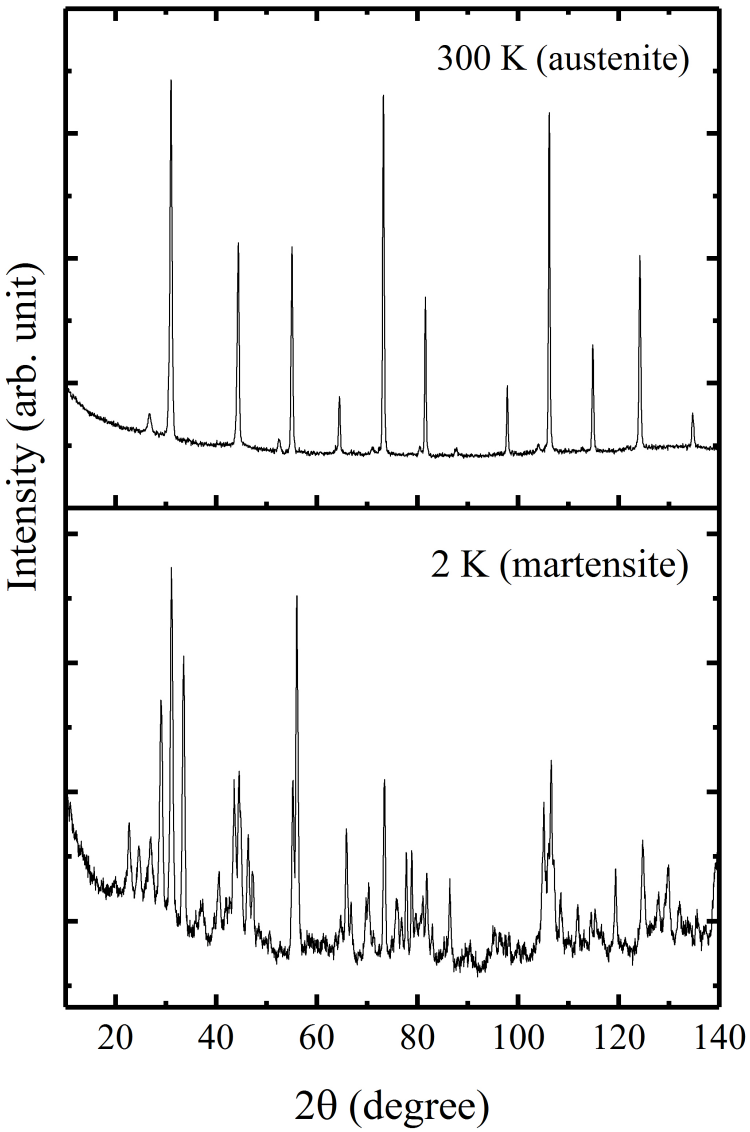

Figure 6.11: *Neutron diffraction pattern in the austenite (300 K) and martensite phase (2 K) of* $Ni_{1.8}Co_{0.2}Mn_{1.4}In_{0.6}$ *in upper and lower panel respectively.*

6.8 Summary

Pressure dependent magnetization was done on $Ni_2Mn_{1.4}In_{0.6}$ and $Ni_{1.8}Co_{0.2}Mn_{1.4}In_{0.6}$ MSM Heusler compounds which reveals that the thermal hysteresis across the martensitic transition decreases with a shift of martensite transition temperature T_M towards to higher temperature upon the application

of hydrostatic pressure. Pressure dependent XRD for $Ni_2Mn_{1.4}In_{0.6}$ was done to investigate the origin of this behavior which reveals that both the lower latent heat and hysteresis minimization with pressure are linked because of increasingly GCC. The increase in pressure more closely satisfies $\lambda_2 = 1$ condition. Lattice parameters of austenite and martensite phase result in a value of $\lambda_2 = 1.0070$ for $Ni_2Mn_{1.4}In_{0.6}$ deviates by 0.7% , while $Ni_{1.8}Co_{0.2}Mn_{1.4}In_{0.6}$ gives a value of $\lambda_2 = 0.9899$ with a deviation of approximately 1% from unity. These studues show that hydrostatic pressure effect on $Ni_{1.8}Co_{0.2}Mn_{1.4}In_{0.6}$ is even more drastic in comparison to $Ni_2Mn_{1.4}In_{0.6}$. The cooling and heating phase transition temperatures of $Ni_{1.8}Co_{0.2}Mn_{1.4}In_{0.6}$ in comparison to $Ni_2Mn_{1.4}In_{0.6}$ are much more sensitive to pressure and shifts to higher temperature with a higher rate of 6.8 K/kbar and 8.4 K/kbar respectively. These values are much larger than those reported by Liu *et al.* [12] for the same composition. Consequently, thermal hysteresis of $Ni_{1.8}Co_{0.2}Mn_{1.4}In_{0.6}$ decreases by half of the ambient pressure value upon application of 10 kbar (28.7 K for P = 0 and 14.3 K for P = 10 kbar) which demonstrates that this behavior is more widely found in Ni-Mn based MSM Heusler compounds. These results show that the GCC between austenite and martensite phase at martensitic transition in MSM Heusler compounds can be tuned and enhanced under the application of hydrostatic pressure. These studies underlines that hydrostatic pressure is an external parameter to overcome the large hysteresis and energy barrier problem in phase transforming MSM Heusler compounds aiming at applications in magnetic refrigeration.

7 Conclusion and Outlook

In this work, the martensitic transition of Ni-Mn based MSM Heusler compounds was investigated with regard to the modulated structure and magnetocaloric properties. Among the large variety of MSM Heusler compounds, the modulated structure was investigated in $Ni_2Mn_{1.4}In_{0.6}$ and $Ni_{1.9}Pt_{0.1}MnGa$ from SXRPD and NPD analysis. The MCE was measured for the optimized compositions of $Ni_{2.2}Mn_{0.8}Ga$ and $Ni_{1.8}Mn_{1.8}In_{0.4}$ in pulsed magnetic field. These compounds exhibit almost reversible behavior because of the reduction of hysteresis from the parent compositions Ni_2MnGa and $Ni_2Mn_{1.4}In_{0.6}$. A strategy of chemical pressure was used to reduce the hysteresis. In addition to that the hysteresis reduction was found by applying physical pressure also in off- stoichiometric $Ni_2Mn_{1.4}In_{0.6}$ and $Ni_{1.8}Co_{0.2}Mn_{1.4}In_{0.6}$ MSM Heusler compounds. Both chemical and physical pressure reduces thermal hysteresis because of the improved GCC by enhancing the compatibility of austenite and martensite phases.

The main conclusions are as follows:

- This thesis investigate the modulated structures of $Ni_2Mn_{1.4}In_{0.6}$ and $Ni_{1.9}Pt_{0.1}MnGa$ by two existing models: adaptive phase model and soft phonon model. The modulated structure was studied first from Le Bail refinement of high resolution SXRPD and NPD patterns in the austenite and martensite phases using $(3+1)-D$ superspace formalism. After that, Rietveld refinement was done. Due to uniform displacement of atoms, $Ni_2Mn_{1.4}In_{0.6}$ follow the adaptive phase model [55]. NPD of $Ni_2Mn_{1.4}In_{0.6}$ shows that at low temperature, the magnetic structure of the martensite phase is anitisite disordered antiferromagnetic. Here, two Mn atoms at two different crystallographic positions are antiferromagnetically coupled. Furthermore, the uniform displacement in $Ni_2Mn_{1.4}In_{0.6}$ was also supported

by HRTEM. In contrast to $Ni_2Mn_{1.4}In_{0.6}$, $Ni_{1.9}Pt_{0.1}MnGa$ shows the robust Bain distortion in the premartensite phase from high resolution SXRPD data. The austenite to martensite transition occurs in three intermediate steps: (i) First transition arises from cubic austenite to $3M$ like incommensurate modulated premartensite phase (T_1) by preserving the cubic austenite symmetry with negligible Bain distortion. (ii) Second transition is from $3M$ like incommensurate modulated premartensite phase (T_1) to $3M$ like incommensurate modulated premartensite phase (T_2) with robust Bain distortion by preserving the superspace group symmetry. (iii) Final transition is from $3M$ like incommensurate modulated premartensite phase to the $7M$ like incommensurate modulated martensite phase. Thus, a small substitution of Pt in Ni_2MnGa facilitates a gradual increase in Bain distortion by maintaining an invariant habit plane requirement all through the three transitions until the martensite phase is formed. The origin of modulation in $Ni_{1.9}Pt_{0.1}MnGa$ is related to a TA_2 soft acoustic phonon mode of the austenite phase [166]. These studies will help to understand the origin of modulation in Ni-Mn based MSM Heusler compounds.

- To check reversibility, a comprehensive study of MCE (ΔS_{M} and ΔT_{ad}) was done on two MSM Heusler compounds $Ni_{2.2}Mn_{0.8}Ga$ and $Ni_{1.8}Mn_{1.8}In_{0.4}$ due to the lower thermal hysteresis in comparison to the previous study. $Ni_{2.2}Mn_{0.8}Ga$ undergoes cubic austenite to tetragonal martensite transition with a thermal hysteresis of 5 K. The isothermal entropy change ΔS_{M} was calculated from $M(H)$ measurements using two different protocols, which acquires the same value of ΔS_{M}, indicating the reversible behavior. These $M(H)$ measurements also show that a field of 6 T was high enough to induce the martensite transition. Therefore, ΔT_{ad} was calculated up to 6 T in pulsed magnetic field. A complete reversible behavior of ΔT_{ad} was observed below, above and within the hysteresis region. This reversible behavior was attributed because of closer GCC ($|\mathbf{U}| = 1.0012$) of cubic austenite to tetragonal martensite phase i.e. small volume change between two phases [68]. $Ni_{1.8}Mn_{1.8}In_{0.4}$ exhibit smaller thermal hysteresis of 9.5 K in comparison to the most studied off-stoichiometric $Ni_2Mn_{1.4}In_{0.6}$ MSM Heusler compound [143, 144, 148, 154].

The isothermal entropy change ΔS_{M} calculated from heating and cooling $M(T)$ curves also exhibits same maxima of ΔS_{M} untill 5 T. An improved reversible behavior of magnetostriction and adiabatic temperature change was also found at three different temperatures, which lies in hysteresis region due to the improved GCC i.e. ($|\lambda_2 - 1| = 0.0006$) of cubic austenite to modulated monoclinic martensite phase.

- Hysteresis reduction was also found by applying hydrostatic pressure. The pressure dependent magnetization experiments were performed in $Ni_2Mn_{1.4}In_{0.6}$ and $Ni_{1.8}Co_{0.2}Mn_{1.4}In_{0.6}$ MSM Heusler compounds which show that the thermal hysteresis is linearly decreased across the martensite transition upon the application of hydrostatic pressure. In addition, latent heat also decreases with pressure. The origin of decrement in thermal hysteresis was investigated from high pressure XRD. It reveals that both thermal hysteresis and latent heat decrease with pressure because of a close satisfaction of GCC. These results conclude that GCC between austenite and martensite phase can be tuned and enhanced by physical pressure [155]. The present study underlines the importance of pressure as an external parameter to overcome the large hysteresis and energy barrier problem in phase transforming MSM Heusler compounds aiming at applications in magnetic refrigeration.

These results stimulate further studies of modulation in MSM Heusler compounds and underline the importance of superspace group analysis of the diffraction data to understand the physics of modulation in these compounds. In view of the fact that large MCE and MFIS are intimately linked with the existence of modulated structure. It is shown that chemical and physical pressure are invaluable tools not only to tune the transition temperature but also to reduce the thermal hysteresis by changing magnetic interaction and thus the interatomic distances. The concept of GCC illustrates how the thermal hysteresis can be reduced in magnetocaloric materials in order to improve the reversibility. This reversibility in cyclic process could enhance the sustainability and reduce the cost of magnetocaloric materials aiming at applications in magnetic refrigeration.

In this thesis, it was demonstrated that how the modulated structure can be manipulated via the chemical composition and atomic substitution. The lower twinning stress of modulated structure results in an easy movement of the material from austenite to martensite and so that it can improves the reversibility of MCE. Therefore, the modulated structure should be studied in these materials carefully.

A small substitution of Pt in Ni_2MnGa changes the modulated structure. However, brittleness and low temperature martensite transition temperature limits its technological applications. Therefore, It will be interesting to study the modulated structure for higher amount of Pt substitution in Ni_2MnGa. There is need to perform the temperature dependent behavior of modulation vector for the material $Ni_2Mn_{1.4}In_{0.6}$ that show adaptive phase model to see that either the incommensuarute wave vector of uniform atomic displacemen lock into commensurate phase or it remain incommensurate.

Based on the finding that the hysteresis reduction can be done by satisfying GCC of two crystallographic phases. In this work, GCC was studied only for two transformation from cubic austenite to tetragonal martensite and cubic austenite to monoclinic martensite. It would be interesting to study the other martensitic transformation such as cubic austenite to orthorhombic martensite. The pressure dependent magnetization studies show the reduction of hysteresis and follows the GCC. Therefore, MCE measurements should also be done under the application of hydrostatic pressure to confirm the reversible behavior.

Bibliography

[1] http: //ozone.unep.org/new_site/en/montreal_protocol.php.

[2] J. R. Gómez, R. F. Garcia, A. D. M. Catoira, and M. R. Gómez, Renew. and Sust. Energ. Rev. **13**, 74 (2013).

[3] K. P. Skokov, A. Y. Karpenkov, D. Y. Karpenkov, and O. Gutfleisch, J. Appl. Phys. **113**, 17A945 (2013).

[4] R. Bjørk, C. Bahl, and K. Nielsen, Int. J. Refrig. **63**, 48 (2016).

[5] B. Yu, M. Liu, P. W. Egolf, and A. Kitanovski, Int. J. Refrig. **33**, 1029 (2010).

[6] E. Warburg, Ann. Phys. **17**, 74 (1881).

[7] A. Smith, C. R. Bahl, R. Bjørk, K. Engelbrecht, K. K. Nielsen, and N. Pryds, Adv. Eng. Mater. **2**, 1288 (2012).

[8] K. P. Skokov, D. Y. Karpenkov, M. D. Kuźmin, I. A. Radulov, T. Gottschall, B. Kaeswurm, M. Fries, and O. Gutfleisch, J. Appl. Phys. **115**, 17A941 (2014).

[9] I. A. Radulov, K. P. Skokov, T. Gottschall, and O. Gutfleisch, J. Mag. Mag. Mater. **396**, 228 (2015).

[10] J. Lyubina, R. Schäfer, N. Martin, L. Schultz, and O. Gutfleisch, Adv. Mater. **22**, 3735 (2010).

[11] V. Franco, J. Blàzquez, B Ingale, and A. Conde, Annu. Rev. Mater. Sci. **42**, 305 (2012).

[12] J. Liu, T. Gottschall, K. P. Skokov, J. D. Moore, and O. Gutfleisch, Nat. Mater. **11**, 620 (2012).

[13] M. Balli, O. Sari, C. Mahmed, C. Besson, P. Bonhote, D. Duc, and J. Forchelet, Appl. Energy **98**, 556 (2012).

[14] K. Engelbrecht, D. Eriksen, C. Bahl, R. Bjørk, J. Geyti, J. Lozano, K. Nielsen, F. Saxild, A. smith, and N. Pryds, Intl. J. Refrig. **35**, 1498 (2012).

[15] A. M. Tishin, K. A. Gschneidner, and V. K. Pecharsky, Phys. Rev. B **59**, 503 (1999).

[16] V. K. Pecharsky, and K. A. Gschneidner, Appl. Phys. Lett. **70**, 3299 (1997).

[17] V. K. Pecharsky, and K. A. Gschneidner Jr., Phys. Rev. Lett. **78**, 4494 (1997).

[18] A. Kitanovski, and P. W. Egolf, Intl. J. Refrig. **29**, 3 (2006).

[19] J. Kynicky, M. Smith, and X. Cheng, Elements **8**, 361 (2012).

[20] A. Fujita, Y. Akamatsu, and K. Fukamichi, J. Appl. Phys. **85**, 4756 (1999).

[21] S. Fujieda, A. Fujita, and K. Fukamichi, Appl. Phys. Lett. **81**, 1276 (2002).

[22] E. Brück, J. Phys. D : Appl. Phys. **38**, R381 (2005).

[23] X. B. Liu, and Z. Altounian, J. Mag. Mag. Mater. **264**, 209 (2003).

[24] M. Krautz, K. Skokov, T. Gottschall, C. S. Teixeira, A. Waske, J. Liu, L. Schultz, and O. Gutfleisch, J. Alloys Compd. **598**, 27 (2014).

[25] O. Tegus, E. Brück, K. H. J. Buschow, and F. R. De Boer, Nature **415**, 150 (2002).

[26] O. Gutfleisch, A. Yan, and K. H. J. Müller, J. Appl. Phys. **97**, 10M305 (2005).

[27] S. Singh, Ph.D. thesis, Devi Ahilya Vishwavidyalaya, Indore (2012).

[28] T. Gottschall, Ph.D. thesis, Technical University of Darmstadt (2016).

[29] M. Ghorbani Zavareh, C. Salazar Mejía, A. K. Nayak, Y. Skourski, J. Wosnitza, C. Felser, and M. Nicklas, Appl. Phys. Lett. **106**, 071904 (2015).

[30] S. Kaufmann, U. K. Rößler, O. Heczko, M. Wuttig, J. Buschbeck, L. Schultz, and S. Fähler, Phys. Rev. Lett. **104**, 145702 (2010).

[31] O. Heusler, Annalen der Physik **411**, 155 (1934).

[32] T. Graf, C. Felser, and Stuart S. P. Parkin, Prog. Sol. Stat. Chem. **39**, 1 (2011).

[33] Y. Song, X. Chen, V. Dabade, T. W. Shield, and R. D. James Nature **502**, 85 (2013).

[34] S. Singh, P. Kushwaha, F. Scheibel, H. P. Liermann, S. R. Barman, M. Acet, C. Felser, and D. Pandey, Phys. Rev. B **92**, 02015 (2015).

[35] S. Chatterjee, S. Giri, S. K. De, and S. Majumdar, Phys. Rev. B **79**, 092410 (2009).

[36] S. Singh, R. Rawat, S. E. Muthu, S. W. D′Souza, E. Suard, A. Senyshyn, S. Banik, P. Rajput, S. Bhardwaj, A. M. Awasthi, R. Ranjan, S. Arumugam, D. L. Schlagel, T. A. Lograsso, A. Chakrabarti, and S. R. Barman, Phys. Rev. Lett. **109**, 246601 (2012).

[37] A. K. Nayak, C. Shekhar, J. Winterlik, A. Gupta, and C. Felser, Appl. Phys. Lett. **100**, 152404 (2012).

[38] O. Mescheriakova, S. Chadov, A. K. Nayak, U. K. Rößssler, J. Kübler, G. André, A. A. Tsirlin, J. Kiss, S. Hausdorf, A. Kalache, W. Schnelle, M. Nicklas, and C. Felser, Phys. Rev. Lett. **113**, 087203 (2014).

[39] A. K. Nayak, C. Salazar Mejía, S. W. D′Souza, S. Chadov, Y. Skourski, C. Felser, and M. Nicklas, Phys. Rev. B **90**, 220408 (2014).

[40] A. K. Nayak, M. Nicklas, S. Chadov, C. Shekhar, Y. Skourski, J. Winterlik, and C. Felser, Phys. Rev. Lett. **110**, 127204 (2013).

[41] H. Kurt, K. Rode, M. Venkatesan, P. Stamenov, and J. M. D. Coey, Phys. Rev. B **83**, 020405(R) (2011).

[42] B. M. Wang, Y. Liu, P. Ren, B. Xia, K. B. Ruan, J. B. Yi, J. Ding, X. G. Li, and L. Wang, Phys. Rev. Lett. **106**, 077203 (2011).

[43] Y. Sutou, Y. Imano, N. Koeda, T. Omori, R. Kainuma, K. Ishida, and K. Oikawa, Appl. Phys. Lett. **85**, 4358 (2004).

[44] K. Ullakko, J. K. Huang, C. Kantner, and R. C. O′Handley, Appl. Phys. Lett. **69**, 1966 (1996).

[45] K. Ullakko, J. K. Huang, V. V. Kokorin, and R. C. O′Handley, Scr. Mater. **36**, 1133 (1997).

[46] A. Sozinov, A. A. Likhachev, N. Lanska, and K. Ullakko, Appl. Phys. Lett. **80**, 1746 (2002).

[47] R. C. O′Handley, J. Appl. Phys. **83**, 3263 (1998).

[48] F. X. Hu, B. G. Shen, and J. R. Sun, Appl. Phys. Lett. **76**, 3460 (2000).

[49] F. X. Hu, B. G. Shen, J. R. Sun, and G. H. Wu., Phys. Rev. B. **64**, 012409 (2001).

[50] T. Krenke, E. Duman, M. Acet, E. F. Wassermann, X. Moya, and L. Mañosa, A. Planes, Nat. Mater. **4**, 450 (2005).

[51] A. K. Nayak, K. G. Suresh, and A. K. Nigam, J. Phys. D : Appl. Phys. **42**, 035009 (2009).

[52] X. Moya, L. Mañosa, A. Planes, T. Krenke, M. Acet, and E. F. Wassermann, Mater. Sci. and Eng.: A **911**, 438 (2006).

[53] S. Singh, L. Caron, S. W. D′Souza, T. Fichtner, G. Porcari, S. Fabbrici, C. Shekhar, S. Chadov, and M. Solzi, Adv. Mater. **28**, 3321 (2016).

[54] S. Singh, S. R. Barman, and D. Pandey, Z. Kristallogr. **230(1)**, 13 (2015).

[55] P. Devi, S. Singh, B. Dutta, K. Manna, S. W. D′Souza, Y. Ikeda, E. Suard, V. Petricek, P. Simon, P. Werner, S. Chadhov, Stuart S. P. Parkin, C. Felser, and D. Pandey, Phys. Rev. B **97**, 224102 (2018).

[56] T. Wagner, and A. Schönleber, Acta Cryst. **B65**, 249 (2009).

[57] J. R. Carvajal, FULLPROF, a Rietveld refinement and pattern matching analysis program, Laboratoire Leon Brillouin, CEA-CNRS, France, (2000).

[58] V. Petricek, M. Dusek, and L. Palatinus, JANA2000: The Crystallographic Computing System (Institute of Physics, Prague, Czech Republic, 2000).

[59] A. Leineweber, and V. Petricek, J. Appl. Cryst. **49**, 1027 (2007).

[60] P. Stephens, J. Appl. Cryst. **32**, 281 (1999).

[61] P. M. De Wolff, Acta Cryst. **A30**, 777 (1974).

[62] T. Janssen, A. Janner, A. Looijenga, and P. M. De Wolff, International tables for Crystallography **C**, 907 (2004).

[63] S. V. Smaalen, Incommensurate Crystallography. IUCr Monographs on Crystyallography 21, Oxford University Press (2007).

[64] V. Srivastava, X. Chen, and R. D. James, Appl. Phys. Lett. **97**, 014101 (2010).

[65] J. Cui, Y. S. Chu, O. O. Famodu, Y. Furuya, J. H. Simpers, R. D. James, A. Ludwig, S. Thienhaus, M. Wuttig, Z. Zhang, and I. Takeuchi, Nature **5**, 286 (2006).

[66] Z. Zhang, R. D. James, and S. Müller, Acta Mater. **57**, 4332 (2009).

[67] K. Bhattacharya, *Microstructure of martensite: Why it forms and how it gives rise to the shape memory effect*, (Oxford Series on Materials Modelling, 2003).

[68] P. Devi, M. Ghorbani Zavareh, C. Salazar Mejía, K. Hofmann, B. Albert, M. Nicklas, and S. Singh, Phys. Rev. Mat. **2**, 122401 (R) (2018).

[69] P. Langevin, Ann. Chim. Phys. **5**, 70 (1905).

[70] A. Weiss, Pierre; Piccard, J. Phys. (Paris) **5**, 103 (1917).

[71] W. F. Giaque, and D. P. MacDougall, Phys. Rev. **43**, 768 (1933).

[72] G. V. Brown, J. Appl. Phys. **47**, 3673 (1976).

[73] J. Barclay, and W. Steyert, Active magnetic regenerator, US Patent 4,332,135 (1982).

[74] V. K. Pecharsky, K. A. Gschneidner Jr., O. Pecharsky, and A. M. Tishin, Phys. Rev. B **64**, 144406 (2001).

[75] P. Debye, Ann. Chim. Phys. **81**, 1154 (1926).

[76] A. M. Tishin, Cryogenics **30**, 127 (1990).

[77] V. K. Pecharsky, and K. A. Gschneidner Jr., J. Appl. Phys. **85**, 5365 (1999).

[78] B. R. Hansen, Ph.D. thesis, Technical University of Denmark (2010).

[79] V. K. Pecharsky, and K. A. Gschneidner Jr., J. Magn. Magn. Mater. **200**, 44 (1999).

[80] A. M. Tishin, *Handbook of magnetic materials*, (Elsevier, Amsterdam, 1999).

[81] E. Brück, J. Kamarad, V. Sechovsky, Z. Arnold, O. Tegus, and F. R. de Boer, Phys. Rev. Lett. **310**, e1008 (2007).

[82] B. K. Ponomarev, Prib. Tekh. Eksp. **3**, 153 (1983).

[83] S. Y. Dan'kov, A. M. Tishin, V. K. Pecharsky, and K. A. Gschneidner Jr., Rev. Sci. Instrum. **68**, 2432 (1997).

[84] B. R. Gopal, R. Chahine, and T. K. Bose, Rev. Sci. Instrum. **68**, 1818 (1997).

[85] B. R. Gopal, R. Chahine, M. Foldeaki, and T. K. Bose, Rev. Sci. Instrum. **66**, 232 (1995).

[86] M. Foldeaki, R. Chahine, and T. K. Bose, J. Appl. Phys. **77**, 3528 (1995).

[87] M. W. Zemansky, *Heat and Thermodynamics*, 6th ed. (McGraw-Hill, New York, 1981).

[88] V. K. Pecharsky and K. A. Gschneidner Jr., J. Appl. Phys. **86**, 565 (1999).

[89] V. K. Pecharsky and K. A. Gschneidner Jr., Adv. Cryog. Eng. **42A**, 423 (1996).

[90] T. Kong, Ph.D. thesis, Iowa State University (2016).

[91] W. Kraus, and G. Nolze, 'Powder cell Version 2.4, 1982', Federal Institute for Materials Research and Testing (BAM), Unter den Eichen 87, D-12205 Berlin, Germany.

[92] D. R. Black, D. Windover, A. Henins, J. Filliben, and J. P. Cline, 'Standard reference material 660B for x-ray Metrology', International Center for Diffraction Data, (2000).

[93] A. G. Khachaturyan, S. M. Shapiro, and S. Semenovskaya, Phys. Rev. B **43**, 10832 (1991).

[94] A. P. Hammersley, J. Appl. Cryst. **49**, 646 (2016).

[95] M. Dušek, V. Petříček, M. Wunschel, R. E. Dinnebier, and S. V. Smaalen, J. Appl. Cryst. **34**, 398 (2001).

[96] L. Mañosa, D. G. Alonso, A. Planes, E. Bonnot, M. Barrio, J. L. Tamarit, S. Aksoy, and M. Acet, Nat. Mater. **9**, 478 (2010).

[97] Quantum Design vibrating sample magnetometer (VSM) Option, User's Manual (2011).

[98] K. Koyama, S. Hane, K. Kamishima, and T. Goto, Rev. Sci. Instrum. **69**, 3009 (1998).

[99] M. Ghorbani Zavareh, Ph.D. thesis, Technical University Dresden (2016).

[100] A. Kirste, Ph.D. thesis, Technical University of Berlin (2003).

[101] Y. Skourski, M. D. Kuzmín, K. P. Skokov, A. V. Andreev, and J. Wosnitza, Phys. Rev. B **83**, 214420 (2011).

[102] S. Singh, J. Bednarcik, S. R. Barman, C. Felser, and D. Pandey, Phys. Rev. B **92**, 054112 (2015).

[103] M. E. Gruner, S. Fähler, and P. Entel, Phys. Stat. Sol. **251**, 2067 (2014).

[104] R. Niemann, U. K. Rößler, M. E. Gruner, O. Heczko, L. Schultz, and S. Fähler, Adv. Eng. Mater. **14**, 562 (2012).

[105] H. Yan, Y. Zhang, N. Xu, A. Senyshyn, H. G. Brokmeier, C. Esling, X. Zhao, and L. Zuo, Acta Mater. **88**, 375 (2015).

[106] A. Smith, Eur. Phys. J. H **38**, 507 (2013).

[107] W. F. Giaque, J. Am. Chem. Soc. **49**, 1864 (1927).

[108] S. Fujieda, A. Fujita, and K. Fukamichi, Appl. Phys. Lett. **81**, 1276 (2002).

[109] A. L. Le Bail, Powder Diffr. **20**, 4 (2005).

[110] T. Jannsen, A. Janner, A. L. Vos, and P. M. De Wolff, Phys. Rev. B **c**, 907 (2006).

[111] N. T. Trung, Ph.D. thesis, Technical University of Delft (2010).

[112] L. Caron, N. T. Trung, and E. Brück, Phys. Rev. B **84**, 020414(R) (2011).

[113] F. X. Hu, B. G. Shen, J. R. Sun, Z. H. Cheng, G. H. Rao, and X. X. Zhang, Appl. Phys. Lett. **78**, 3675 (2001).

[114] N. T. Trung, Z. Q. Ou, T. J. Gortenmulder, O. Tegus, K. H. J. Buschow, and E. Brück, Appl. Phys. Lett. **94**, 102513 (2009).

[115] T. Krenke, E. Duman, M. Acet, E. F. Wassermann, X. Moya, L. Mañosa, and A. Planes, Nat. Mater. **4**, 450 (2005).

[116] S. M. Shapiro, Y. Noda, Y. Fujii, and Y. Yamada, Phys. Rev. B **30**, 4314 (1984).

[117] S. M. Shapiro, B. X. Yang, Y. Noda, L. E. Tanner, and D. Schryvers, Phys. Rev. B **44**, 9301 (1991).

[118] S. M. Shapiro, E. C. Svensson, C. Vettier, and B. Hennion, Phys. Rev. B **48**, 13223 (1993).

[119] L. Ye, S. Shapiro, and H. Chou, Scr. Met. Mater. **31**, 203 (1994).

[120] T. Ohba, S. Shapiro, S. Aoki, and K. Otsuka, Jpn J. Appl. Phys. **33**, L1631 (1994).

[121] K. Otsuka, T. Sawamura, and K. Shimizu, Phys. Stat. Sol. A **5**, 457 (1971).

[122] A. Planes, E. Obradó, A. Gonzàleg-Comas, and L. Mañosa, Phys. Rev. Lett. **79**, 3926 (1997).

[123] V. V. Kokorin, V. A. Chernenko, J. Pons, C. Segu, and E. Cesari, Sol. Stat. Commun. **101**, 7 (1997).

[124] U. Stuhr, P. Vorderwisch, V. V. Kokorin, and P. A. Lindgård, Phys. Rev. B **56**, 14360 (1997).

[125] A. Jayaraman, Phys. Rev. Lett. **29**, 1674 (1972).

[126] J. P. Patel, A. Senyshyn, H. Fuess, and D. Pandey, Phys. Rev. B **88**, 104108 (2013).

[127] S. Bhattacharjee, K. Taji, C. Moriyoshi, Y. Kuroiwa, and D. Pandey, Phys. Rev. B **84**, 104116 (2011).

[128] S. Banik, Aparna Chakrabarti, U. Kumar, P. K. Mukhopadhyay, A. M. Awasthi, R. Ranjan, J. Schneider, B. L. Ahuja, and S. R. Barman, Phys. Rev. B **74**, 085110 (2006).

[129] P. J. Webster, K. R. A. Ziebeck, S. L. Town, and M. S. Peak, Phil. Mag. B **49**, 295 (1984).

[130] P. J. Brown, J. Crangle, T. Kanomata, M. Matsumoto, K. U. Neumann, B. Ouladdiaf, and K. R. A. Ziebeck, J. Phys. Condens. Matter **14**, 10159 (2002).

[131] S. Singh, J. Nayak, A. Rai, P. Rajput, A. H. Hill, S. R. Barman, and D. Pandey, J. Phys. Condens. Matter **25**, 212203 (2013).

[132] S. Singh, V. Petricek, P. Rajput, A. H. Hill, E. Suard, S. R. Barman, and D. Pandey, Phys. Rev. B **90**, 014109 (2014).

[133] S. W. D′Souza, A. Rai, J. Nayak, M. Maniraj, R. S. Dhaka, S. R. Barman, D. L. Schlagel, T. A. Lograsso, and A. Chakrabarti, Phys. Rev. B **85**, 085123 (2012).

[134] A. Zheludev, S. M. Shapiro, P. Wochner, A. Schwartz, M. Wall, and L. E. Tanner, Phys. Rev. B **51**, 11310 (1995).

[135] A. Pramanick, X. P. Wang, K. An, A. D. Stoica, J. Yi, Z. Gai, C. Hoffmann, and X. L. Wang, Phys. Rev. B **85**, 144412 (2012).

[136] S. Banik, S. Singh, R. Rawat, P. K. Mukhopadhyay, B. L. Ahuja, A.M. Awasthi, S. R. Barman, and E. V. Sampathkumaran, J. Appl. Phys. **106**, 103919 (2009).

[137] S. Banik, R. Ranjan, A. Chakrabarti, S. Bhardwaj, N. P. Lalla, A. M. Awasthi, V. Sathe, D. M. Phase, P. K. Mukhopadhyay, D. Pandey, and S. R. Barman, Phys. Rev. B **75**, 104107 (2007).

[138] K. F. Hane, and T. W. Shield, Phil. Mag. A **78**, 1215 (1998).

[139] S. M. Shapiro, P. Vorderwisch, K. Habicht, K. Hradil, and H. Schneider, Eur. Phys. Lett. **77**, 56004 (2007).

[140] V. V. Khovaylo, K. P. Skokov, Yu. S. Koshkid′ko, V. V. Koledov, V. G. Shavrov, V. D. Buchelnikov, S. V. Taskaev, H. Miki, T. Takagi, and A. N. Vasiliev, Phys. Rev. B **78**, 060403(R) (2008).

[141] V. V. Khovaylo, T. Takagi, J. Tani, R. Z. Levitin, A. A. Cherechukin, M. Matsumoto, and R. Note, Phys. Rev. B **65**, 092410 (2002).

[142] V. V. Khovaylo, K. P. Skokov, O. Gutfleisch, H. Miki, T. Takagi, T. Kanomata, V. V. Koledov, V. G. Shavrov, G. Wang, E. Palacios, J. Bartolomè, and R. Burriel, Phys. Rev. B **81**, 214406 (2010).

[143] T. Gottschall, K. P. Skokov, B. Frincu, and O. Gutfleisch, Appl. Phys. Lett. **106**, 021901 (2015).

[144] S. Aksoy, M. Acet, P. P. Deen, L. Mañosa, and A. Planes, Phys. Rev. B **79**, 212401 (2009).

[145] S. R. Barman, A. Chakrabarti, S. Singh, S. Banik, S. Bhardwaj, P. L. Paulose, B. A. Chalke, A. K. Panda, A. Mitra, and A. M. Awasthi, Phys. Rev. B **78**, 134406 (2008).

[146] S. Singh, K. R. A. Ziebeck, E. Suard, P. Rajput, S. Bhardwaj, A. M. Awasthi, and S. R. Barman, Appl. Phys. Lett. **101**, 171904(2012).

[147] S. Singh, R. Rawat, and S. R. Barman, Appl. Phys. Lett. **99**, 021902(2011).

[148] X. Moya, D. González- Alonso, L. Mañosa, A. Planes, V. O. Garlea, T. A. Lograsso, D. L. Schlagel, J. L. Zarestky, S. Aksoy, and M. Acet, Phys. Rev. B **79**, 214118(2008).

[149] G. D. Liu, J. L. Chen, Z. H. Liu, X. F. Dai, G. H. Wu, B. Zhang, and X. X. Zhang, Appl. Phys. Lett. **104**, 262504 (2005).

[150] C. P. Sasso, M. Pasquale, L. Giudici, S. Besseghini, and E. Villa, J. App. Phys. **99**, 08K905 (2006).

[151] S. Singh, S. W. D′Souza, K. Mukherjee, P. Kushwaha, S. R. Barman, S. Agarwal, P. K. Mukhopadhyay, A. Chakrabarti, and E. V. Sampathkumaran, Appl. Phys. Lett. **104**, 231909 (2014).

[152] S. Stadler, M. Khan, J. Mitchell, N. Ali, A. M. Gomes, I. Dubenko, A. Y. Takeuchi, and A. P. Guimarães, Appl. Phys. Lett. **88**, 192511 (2006).

[153] E. Stern-Taulats, A. Planes, P. Lloveras, M. Barrio, J. L. Tamarit, S. Pramanick, S. Majumdar, S. Yücke, B. Emre, C. Frontera, and L. Mañosa, Acta Mater. **96**, 324 (2015)

[154] A. Planes, L. Mañosa, and M. Acet, J. Phys. Condens. Matter **21**, 233201 (2009).

[155] L. Caron, P. Devi, A. Magnus G. Carvalho, E. Suard, C. Felser, and S. Singh, arxiv: 1806.05075 (2018).

[156] L. Mañosa, X. Moya, and A. Planes, Appl. Phys. Lett. **92**, 012512 (2008).

[157] B. Kaeswurm, V. Franco, K. P. Skokov, and O. Gutfleisch, J. Magn. Magn. Mater. **406**, 259 (2016).

[158] X. L. Meng, H. Li, W. Cai, S. J. Hao, and L. S. Cui, Scr. Mater. **103**, 30 (2015).

[159] R. Delville, R. D. James, U. Salman, A. Finel, and D. Schryyers, Esomat **10**, 02005 (2009).

[160] S. Niziol, A. Zieba, R. Zach, M. Baj, and L. Dmowski, J. Magn. Magn. Mater. **38**, 205 (1983).

[161] J. Lyubina, K. Nenkov, L. Schultz, and O. Gutfleisch, Phys. Rev. Lett. **101**, 177203 (2008).

[162] H. Kushida, T. Terai, T. Fukuda, T. Kakeshita, T. Osakabe, and K. Kakurai, Scr. Mater. **60**, 248 (2009).

[163] L. Righi, F. Albertini, G. Calestani, L. Pareti, A. Paoluzi, C. Ritter, P. A. Algarabel, L. Morellon, and M. R. Ibarra, J. Sol. Stat. Chem. **179**, 3525 (2006).

[164] S. Lee, A. Pirogov, M. Kang, K. H. Jang, M. Yonemura, T. Kamiyama, S. W. Cheong, F. Gozzo, N. Shin, H. Kimura, Y. Noda, and J. G. Park, Nature **451**, 805 (2008).

[165] A. Singh, V. Pandey, R. K. Kotnala, and D. Pandey, Phys. Rev. Lett. **101**, 247602 (2008).

[166] S. Singh, B. Dutta, S. W. D′Souza, M. G. Zavareh, P. Devi, A. S. Gibbs, T. Hickel, S. Chadov, C. Felser and D. Pandey, Nat. commun. **8**, 1006 (2017).

List of publications

- P. Devi, M. Ghorbani Zavareh, C. Salazar Mejia, K. Hofmann, B. Albert, C. Felser, M. Nicklas, and Sanjay Singh; *Reversible adiabatic temperature change in the shape memory Heusler alloy $Ni_{2.2}Mn_{0.8}Ga$: an effect of structural compatibility*, Phys. Rev. Mat. **2**, 122401(R) (2018).

- P. Devi, Sanjay Singh, B. Dutta, K. Manna, S. W. D′Souza, Y. Ikeda, E. Suard, V. Petricek, P. Simon, P. Werner, S. Chadhov, Stuart S. P. Parkin, C. Felser, and D. Pandey; *Adaptive modulation in the $Ni_2Mn_{1.4}In_{0.6}$ magnetic shape memory Heusler alloy*, Phys. Rev. B **97**, 224102 (2018).

- P. Devi, C. Salazar Mejia, M. Ghorbani Zavareh, K. Hofmann, Pallavi Kushwaha, C. Felser, M. Nicklas, and Sanjay Singh; *Improved reversibility of magnetostriction and magnetocaloric effect in Ni-Mn-In magnetic shape memory Heusler alloy as an effect of cofactor condition*, under review in Phys. Rev. Mater. rapid communication.

- L. Caron, B. Dutta, P. Devi, M. Ghorbani Zavareh, T. Hickel, R. Cabassi, F. Bolzoni, S. Fabbrici, F. Albertini, C. Felser, and Sanjay Singh; *Effect of Pt substitution on the magnetocrystalline anisotropy of Ni_2MnGa: A competition between chemistry and elasticity*, Phys. Rev. B **96**, 054105 (2017).

- Sanjay Singh, B. Dutta, S. W. D′Souza, M. G. Zavareh, P. Devi, A. S. Gibbs, T. Hickel, S. Chadov, C. Felser, and D. Pandey; *Robust Bain distortion in the premartensite phase of a platinum-substituted Ni_2MnGa magnetic shape memory alloy*, Nat. Commun. **8**, 1006 (2017).

- L. Caron, P. Devi, Alexandre M. G. Carvalho, C. Felser, Sanjay Singh; *Minimizing hysteresis in martensite phase transforming magnetocaloric*

Heulser alloys, arxiv: 1806.05075 (2018).

- Shamim Sk, P. Devi, Sanjay Singh, and Sudhir K Pandey; *Exploring the best scenario for understanding the high temperature thermoelectric behaviour of Fe_2VAl*, Mater. Res. Exp. **6**, 026302 (2018).

- A. S. Sukhanov, Sanjay Singh, L. Caron, Th. Hansen, A. Hoser, V. Kumar, H. Borrmann, A. Fitch, P. Devi, K. Manna, C. Felser, and D. S. Inosov; *Gradual pressure-induced change in the magnetic structure of the noncollinear antiferromagnet Mn_3Ge*, Phys. Rev. B **97**, 214402 (2018).

- P. Devi, Manfred Reehuis, Peter Adler, Andreas Hoser, Sanjay Singh, and C. Felser; *Long-range non collinearity and spin reorientation transition in the centrosymmetric Ni-Mn-Ga hexagonal magnet*, submitted to Phys. Rev. B.

- P. Devi, C. Salazar Mejia, L. Caron, Sanjay Singh, and C. Felser; *Large reversible magnetocaloric effect in Ni-Cu-Mn-In magnetic shape memory Heusler alloy*, submitted to Phys. Rev. B.

Appendix

Table 7.1: *An overview of the prepared and investigated single phase Heusler compounds, which are not presented in this thesis. The stoichiometry, optimized condition and their martensitic transition temperature are specified.*

Material	Optimized condition	martensite temperature T_M (K)
Ni_2MnGa	900°C - 72h - wq	210
$Ni_{1.9}Pt_{0.1}MnGa$	900°C - 72h - wq	250
$Ni_{1.8}Pt_{0.2}MnGa$	900°C - 72h - wq	240
$Ni_{1.7}Pt_{0.3}MnGa$	1000°C - 72h - wq	270
$Ni_2Cu_{0.1}Mn_{1.3}In_{0.6}$	1000°C - 24h - wq	280
$Ni_2Cu_{0.2}Mn_{1.2}In_{0.6}$	1000°C - 24h - wq	290
$Ni_2Cr_{0.1}Mn_{1.3}In_{0.6}$	900°C - 24h - wq	270
$Ni_2Cr_{0.2}Mn_{1.2}In_{0.6}$	900°C - 24h - wq	250
$Ni_2Cr_{0.3}Mn_{1.1}In_{0.6}$	900°C - 24h - wq	210
$Ni_2Cr_{0.4}Mn_1In_{0.6}$	900°C - 24h - wq	200
$Ni_{1.8}Co_{0.2}Cr_{0.2}Mn_{1.28}In_{0.52}$	900°C - 24h - wq	230
$Ni_2Pt_{0.1}Mn_{1.3}In_{0.6}$	1000°C - 72h - wq	270
$Ni_2Pt_{0.2}Mn_{1.2}In_{0.6}$	1000°C - 72h - wq	260
$Ni_{1.72}Co_{0.28}Mn_{1.52}Sb_{0.48}$	850°C - 24h - wq	230
$Ni_{1.76}Co_{0.24}Mn_{1.52}In_{0.48}$	850°C - 24h - wq	260
$Ni_{1.88}Mn_{1.6}Sn_{0.52}$	850°C - 24h - wq	100

Acknowledgment

This Dissertation would not have been possible without the goodwill and synchronized efforts of many people. It is a pleasure to thank everyone who has helped me reach this milestone of my life.

- I thank all people, who helped and assisted me during my scientific studies along the way. Without their support, this work would have never been done.
- First and foremost, I would like to thank Prof. Dr. Claudia Felser especially for giving me the opportunity to join her group in 2016 as a PhD student. During that time, I realized my fascination with magnetism
- I am grateful to Prof. Dr. Dmytro S. Inosov for kindly agreeing to be my supervisor of TU Dresden.
- Furthermore, I want to thank Prof. Dr. Sebastian T. B. Goennenwein, who kindly agreed to be a referee for my Doctoral thesis.
- My special thanks go to **Dr. Sanjay Singh**, Dr. Michael Nicklas and Dr. Chandra Shekhar for their guidance, discussion, and help in writing proposals and papers.
- Dr. Walter Schnelle and Ralf Koban for assistance with the magnetization and transport measurements using SVSM and PPMS.
- Dr. Gudrun Aufferman for her friendly help in regulations and suggestions about PhD work.
- Dr. Marcus Schmidt and Susann Scharsach for doing the DSC measurement of various samples.

❖ Dr. Catalina Salazar Mejia and Prof. Dr. Jochen Wosnitza of Helmholtz âZentrum Dresden Rossendorf for giving me the opportunity to do the pulsed field measurements of the stress and adiabatic temperature change in their institute.

❖ Dr. Emma Suard at the Institut Laue Lengevin France for her help in neutron diffraction measurement on D2B instrument.

❖ Dr. Stanislav Chadov for doing the theory and fruitful discussions in several papers.

❖ Vivek Kumar and Praveen Vir for the introduction to the "workflow" showing me around the labs at the very beginning of my work.

❖ The whole working group of Prof. Dr. Claudia Felser for the very scientific and friendly atmosphere, discussions on science and life.

❖ Last but not least, I want to thank my family and friends, especially my mother for the constant motivation, support and love through my life and research.

This document was produced using MiKT$_E$X v.2.6 typesetting system.